Joint Pose and Radio Channel Estimation

Mannesson, Anders

2013

Document Version:
Publisher's PDF, also known as Version of record

Joint Pose and Radio Channel Estimation

Anders Mannesson

LUNDS
UNIVERSITET

Department of Automatic Control

To Julia and Folke

Department of Automatic Control
Lund University
Box 118
SE-221 00 LUND
Sweden

ISSN 0280–5316
ISRN LUTFD2/TFRT--3263--SE

Printed in Sweden by Media-Tryck.
Lund 2013

Abstract

This thesis investigates the combination of pose and radio channel estimation. Pose is the knowledge of the position and orientation of a device whereas the radio channel describes the transmission medium between radio transmitters and receivers. The two subjects are both active research topics with a long history of applications but there has to the author's knowledge been very little work published about combining the two areas using a sensor fusion framework.

A well established approach for pose estimation is using an inertial measurement unit (IMU). Using an inexpensive IMU standalone for dead reckoning pose estimation is tempting but it is not a working solution due to noise and other imperfections in the IMU. There is also a fundamental limitation of inertial sensors, they can not, because of Galileo's principle, obtain any information about absolute velocity of the device. To obtain reliable pose estimates for a longer time, the measurements from the IMU must be fused with some other sensor information. This thesis shows how the pervasive electric magnetic fields from existing radio communication systems such as the cellular mobile systems GSM, 3G, or 4G can be used.

Angle of arrival estimation using antenna arrays is a well studied problem with many different algorithms resolving the individual rays impinging on the array. However, less attention has been given to so called virtual array antennas where only one receiver element is used. By tracking the movement of the element, an array with properties similar to a stationary array with multiple elements is formed. By combining the IMU and the radio channel information, a map of the local radio environment can be obtained. At the same time, the map is used for adjusting for the errors in the IMU that lead to inaccurate pose estimates by using tightly coupled nonlinear state estimation algorithms from the sensor fusion framework.

The goals for this thesis is to develop a dynamic model for kinematics and a ray-trace based radio channel model that can be used together with the particle filter for sensor fusion. It also contains an initial investigation of limitations and achievable performance for the joint pose and radio channel

estimation problem, including radio imperfection such as thermal noise, and phase/frequency error. The proposed model is evaluated using both simulations and datasets from experiments. The analysis of the evaluation shows that the proposed model, together with sensor fusion algorithms, provides a breakthrough in pose estimation using a low cost IMU.

Acknowledgments

To execute a project of this kind is a journey into the unknown. You never know what is waiting for you further on up the road. Therefore, it is important to bring good colleagues and friends along to be prepared for all possibilities.

First of all I would like to thank my main supervisor, Prof. Bo Bernhardsson for convincing me to enter the path of research after I had spent a few years in industry. The journey with you has been both challenging and rewarding. It is a privilege to work with someone with a strong technical knowledge and great intuition to all kind of problems. The next person who is recognized is my Ph.D. student colleague Atif Yaqoob at the Electrical and Information Theory Department (EIT). You have helped me fill in the blanks of my knowledge of radio channels but most important of all, carrying out the measurement series for this work. You have a strong commitment to do things carefully which has proven to be important when working with experimental data. Also, at the same department, Assoc. Prof. Fredrik Tufvesson has been the originator of this problem. Your creativity, inputs, and knowledge of radio systems and channels has been invaluable to this project. Also, a big thanks to you and EIT for supplying experimental equipment and lab resources for this project. To my third supervisor, Dr. Johan Åkesson, we have not worked very tight in this project but your input has been rewarding and you are also great for keeping my spirit up.

Among the Ph.D. students at my department, I especially want to recognize Karl Berntorp and Jerker Nordh. You have both been contributing to my research by sharing the same research interest. It is always valuable to have someone to talk to about intricate problems that arise along the road. Also a big thanks goes to Olof Sörnmo for input on my manuscript and my room mate Fredrik Magnusson for enduring my questions of all kinds.

I also want to thank Assoc. Prof. Thomas Schön at Linköping University for rewarding discussions at different stages of the project and great teaching of the course in machine learning. Further, thanks to the VICON lab at Linköping University for letting us do measurements there.

Finally I would like to thank my friends and family but most important of all, the love of my life, my wonderful wife Julia. Without your love, support, and understanding this work would never have been possible.

The author is part of the LCCC Linnaeus Center, supported by the Swedish Research Council, and The Lund Linköping Initiative on IT (ELLIIT) Excellence Center, supported by the Swedish Government. Also, support from Vetenskapsrådet, project number 2012-42391-93793-23, is acknowledged.

Contents

1

Introduction

1.1 Motivation

This thesis investigates joint pose and radio channel estimation. Pose is the description of how a rigid body is orientated and positioned whereas the radio channel describes the wireless transmission properties from one or several transmitters to one or several receivers, often in a mobile scenario. The two subjects are both active research areas with a long history of applications. The novelty in this thesis is the combination of the two, using tightly coupled algorithms. There are two goals with this approach:

- to improve pose estimation performance by fusing information from the radio channel or
- to improve radio channel estimation and prediction by fusing pose information.

This thesis investigates and describes background and algorithms suitable for both goals, but the focus is on the former.

1.2 Pose estimation

As stated before, the combination of position and orientation relative to a fixed frame is referred to as pose and is one of the ingredients in navigation and device tracking. The other part in navigation is the map. The map is usually thought of as a representation of the physical surroundings but it could just as well be a description of the surroundings as seen by a sensor. In some situations, the map is known beforehand and can be used for improving the localization of the unit. However, if the map is unknown, it needs to be reconstructed at the same time as pose estimation is done. This problem is called simultaneous localization and mapping (SLAM) and has been studied thoroughly in the literature over the last years [Bailey and Durrant-Whyte,

2006a], [Bailey and Durrant-Whyte, 2006b], and [Davison, 2003]. In this thesis, a model of the radio channel will be the map. This will be described in Chapter 2.

With the development of Micro-Electro-Mechanical Systems (MEMS), such as accelerometers and gyroscopes, inertial measurement units (IMU) are nowadays small and inexpensive. The accelerometer measures proper acceleration of the device while the gyroscope measures the angular velocity. The price for an IMU ranges from $1 to several $1000. The expensive ones exhibit lower noise levels in general compared to the inexpensive ones and they may also include software and other sensors on the board, *e.g.*, magnetometers for measuring the magnetic field of the surroundings. Also, the size and power consumption differs between different IMUs.

The IMU can be used for building an inertial navigation system (INS), able to measure pose [Titterton and Weston, 2004]. Due to its simplicity, a tempting solution for pose estimation using an IMU is the dead reckoning approach. The system is depicted in Figure 1.1.

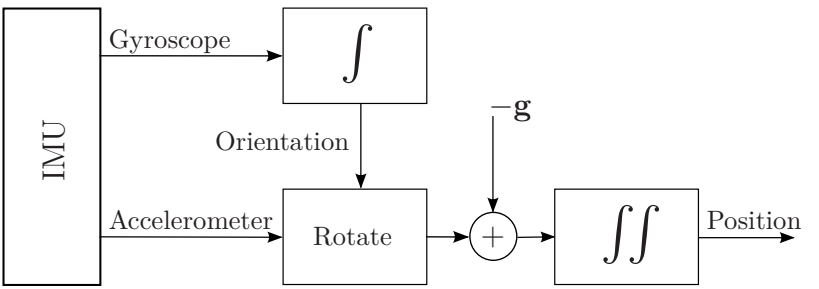

Figure 1.1 Dead reckoning approach using an IMU. The gyroscope signal is integrated once to obtain orientation which is used for rotating the accelerometer signal from body coordinates to world coordinates. Gravity **g** is removed after rotation and the residual is integrated twice to obtain position.

Gyroscope readings are integrated once in order to obtain the orientation of the device. The accelerometer readings are then rotated with the knowledge of the orientation of the device before gravity is removed and double integration then yields the position. However, such a system fails to function for any longer period of time due to noise and imperfections in the IMU. The noise will be integrated in the system leading to growing variance of the estimated position. Also, constant offsets or bias in the signals will keep adding up on the orientation and position leading to an ever increasing estimation error.

Depending on noise and bias levels, the IMUs are usually classified into

different grades. Common names for these grades are consumer, industrial, and tactical grade. In Figure 1.2, typical dead reckoning position error using an IMU from each class is shown. The noise values used for simulations are presented in Table 1.1. The noise processes on the IMU will be further explained in Chapter 3.

	Velocity Random Walk $[\mathrm{m/s}/\sqrt{\mathrm{h}}]$	Angle Random Walk $[^\circ/\sqrt{\mathrm{h}}]$	Angle Bias Stability $[^\circ/\mathrm{h}]$	Stability Time [s]
Consumer	0.2	2	20	360
Industrial	0.1	0.2	10	72
Tactical	0.05	0.02	1	72

Table 1.1 Noise level for the accelerometer and the gyroscope for three different IMU grades. The bias stability time is defined as the time when the contribution from the angle random walk noise process is equal to the contribution from the angle bias stability noise process.

The rapid growth of the position error as seen in Figure 1.2 is mainly coming from the gyroscope. A constant offset in the gyroscope readings will translate into an increasing orientation error and finally a position error as

$$\tilde{p} \propto t^3 \tag{1.1}$$

where $\tilde{p}$ is the error in the estimated position. Hence, before the IMU can be used for estimating pose for any longer period of time, it has to be aided with some other sensor information.

Improving pose estimation by sensor fusion

The imperfections that limit the pose estimation performance of the dead reckoned IMU are different kinds of noise sources, present on both the accelerometer and the gyroscope. One way to improve the estimation performance in terms of accuracy, is to fuse the IMU sensor information with pose information from another sensor [Gustafsson, 2010]. There are three categories of sensor information that can be fused:

- information from spatially separated sensors,
- temporal sensor information, and
- modal sensor information, *i.e.*, sensors measuring the physical quantity differently.

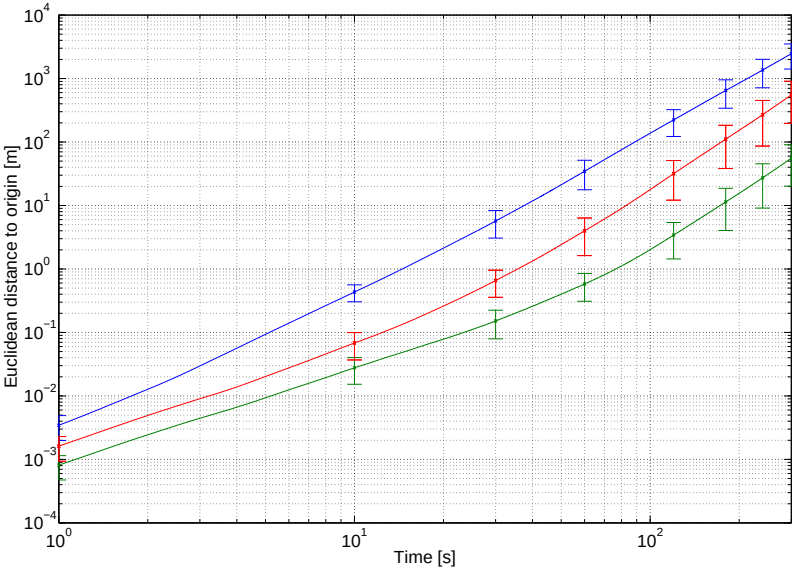

Figure 1.2 Euclidean error distance as a function of time for three different grades of IMUs, see Table 1.1 for noise specifications of the different IMU classes. The IMU grades are marked as (—) consumer, (—) industrial, and (—) tactical. The vertical bars indicate one standard deviation.

One example of sensor fusion is depth vision for humans; a one eyed person can not obtain any depth information but with two eyes, slightly separated, distance to close-by objects can be obtained.

To be able to fuse sensor information, a probabilistic model is needed of how the different measurements from different sensors are related to each other in time and space. A well established way to represent such a model is by using a discrete nonlinear state space representation

$$\begin{cases} x_{k+1} = f(x_k, u_k, n_k) \\ y_k \;\; = h(x_k, w_k), \end{cases} \tag{1.2}$$

where x_k is the state vector at time k, u_k is the control signal to the system, y_k is the output signal, and n_k and w_k are stochastic noise processes for the states and measurements respectively. In the case of pose estimation, pose is obviously a part of the state vector but it can also contain other states describing the system.

In the literature, many different proposals have been made to improve navigation with IMU based INS using sensor fusion. One example is fusing the IMU information with a GPS receiver using the positions from the GPS system. Thus, the IMU is used for pose estimation in between the GPS

position updates. Several implementations for such systems in different applications have proven the technique highly successful, see [Sukkarieh et al., 1999], [Godha et al., 2006], and [Zhang et al., 2005]. Another proposal is to use delay time from transmitter to receiver in various wireless networks, such as WiFi and Ultra Wideband (UWB), in order to obtain distances to the transmitters [Gu et al., 2009]. From the individual distances, triangulation can be used to determine the location of the device. These techniques are in the literature referred to as time of arrival (TOA) or time difference of arrival (TDOA). Others have used statistical information on how the signal strength for radio wave propagation decays with distance in order to estimate position [Pei et al., 2010] and [Woodman and Harle, 2008]. Yet another possibility is to combine the IMU with a camera and to detect interest points in the images in order to facilitate the pose estimation [Achtelik et al., 2011]. The common denominator for all techniques is sensor fusion of two or more sensors to achieve better estimation performance compared to a single sensor system. For personal tracking, a solution with a foot mounted IMU alone has proven to yield reliable estimates of the position using detection of zero velocity in the IMU signal, [Sabatini et al., 2005] and [Skog et al., 2010].

1.3 Radio channel estimation

The transmission medium between a transmitter antenna and a receiver antenna can be modeled as a linear time varying system (LTV) known as the radio channel. The radio channel can be described with a complex-valued unknown transfer function $H(t, f)$, where t is time and f is the transmit frequency, see Figure 1.3. The figure shows a strong channel at 2.44 GHz while there is one that dies out at 2.41 GHz after a few seconds.

The varying time-frequency pattern of the channel is a sign of multipath wave propagation. Between the transmitter and the receiver there will be objects that scatterer the transmitted signal, creating multiple components of it. Due to different travel distances of the components, they will reach the receiver at different times. Thus, a transmitted symbol will interfere with subsequent symbols at the receiver. This multipath model will be discussed in Chapter 2.

The multipath propagation can be a problem for mobile communication where as much information as possible is to be transferred to the users. It can however also be taken advantage of as it can be used to create multiple parallel transmission channels. This is done in recent MIMO systems, *i.e.*, systems with multiple transmit and receive antennas. Since every user experiences a unique radio channel, a bad channel for one user might be a good channel for another. If the system has knowledge of the radio channels to every user in the system, transmissions can be scheduled to increase the

transmission rates to the users. Also error coding of the signal and modulation of the data can be adjusted to fit the capacity of the current channel. By applying these techniques, data rates can be increased substantially in the network [Dahlman et al., 2010].

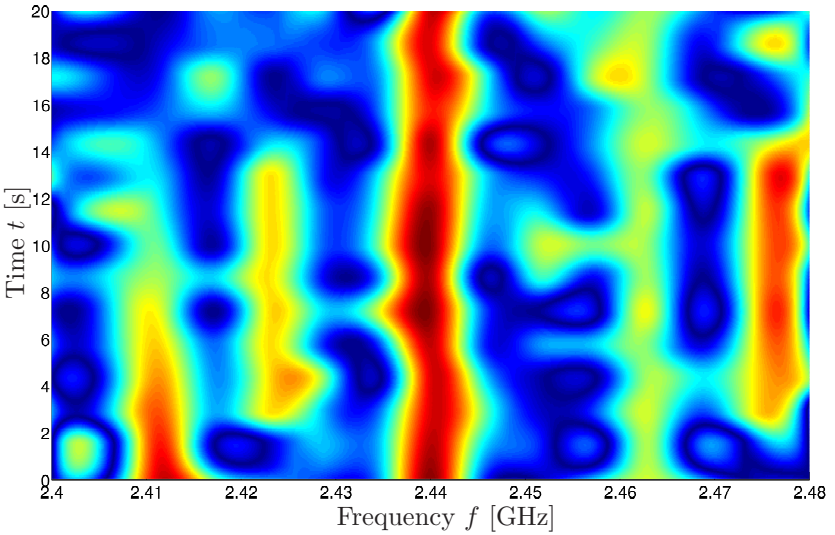

Figure 1.3 Transfer function of radio channel as a function of transmission frequency f and time t. The color indicates $|H(t, f)|$ and red symbolize a frequency with strong gain.

Most efficient communication schemes rely on good estimates of the radio channel. A significant part of the signal processing calculations in cellular phones are used by the radio channel estimation algorithms. The form of these algorithms depend on the communication system. Most often, so called training sequences or *pilots* are used, *i.e.*, a predetermined known signal is transmitted and used by the receivers to estimate the channel. At some time instance, the estimated radio channel parameters are communicated back to the transmitter, increasing the overhead even further. There also exists so called blind channel estimation algorithms. The radio channel estimation is then performed on transmitted user data, using some a priori knowledge about its structure. The advantage with the blind schemes is that bandwidth efficiency is not wasted by pilots, but the drawback is reduced estimation performance. Pilots are therefore used in most wireless systems today.

Traditional approaches to channel estimation are typically based on least squares approaches, with or without using a priori information about the channel transfer function matrix $H(t, f)$. For descriptions of possible schemes

used for the GSM system see, *e.g.*, [Khayrallah et al., 1997] and [Arildsen and Blauendahl, 2010]. For a blind estimation scheme, see [Boss and Kammeyer, 1997].

Channel estimation techniques for the WCDMA (3G) communication systems are different from GSM, since WCDMA uses a spread-spectrum technique. Some different pilot-based approaches are described in [Richardson, 2011], [Andoh et al., 1998], and [Han, 2004]. Channel estimation for the DVB (TV broadcasting) and LTE/4G systems are similar since these are so called OFDM systems, using a multi-carrier technique for modulation. Pilots with certain positions in the time-frequency domain are used, as shown in Figure 1.4. For some typical channel estimation algorithms for OFDM see [Edfors et al., 1998], [Bahai et al., 2004], and [Coleri et al., 2002].

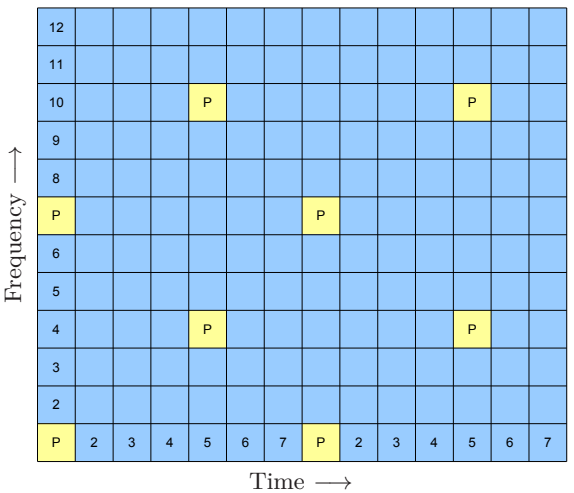

Figure 1.4 Pilot scheduling in the LTE/4G cellular system. Each square represents one time-frequency transmission slot. The pilots consist of known transmission signals used to estimate the radio channel.

1.4 Previous work of joint pose and channel estimation

Very little previous work has been found dealing with tight integration between pose and radio channel estimation. In [Broumandan et al., 2007], the authors investigate the possibility of combining IMU with GPS receivers to improve robustness against interfering transmitters in the GPS frequency band. The IMU is used for obtaining the positions of the receiver antenna along a circular trajectory. However, there is no tight integration between the

IMU and the GPS receiver thus leaving the position estimates unconnected with the radio environment estimation. The same authors follow up the work with investigation of detection performance with a moving antenna in indoor environments in [Broumandan et al., 2010].

[Schmeink et al., 2010] studies channel estimation for the stationary case trying to estimate the channel parameters by an optimization algorithm applicable to nonlinear problems. Since the proposed technique investigates a stationary case, there is no need for a dynamic motion model. [Liang et al., 2006] explores the possibility to estimate the radio channel using the same kind of algorithms investigated in this thesis but once again there is no motion involved.

1.5 Problem formulation

The focus of this thesis is on improving pose estimation performance by sensor fusion with radio channel information since it is believed to have potential for a disruptive technology breakthrough in terms of accuracy of INS performance. The reason for the rapid increase in the position estimate error in the dead reckoning approach is due to the fact that the IMU can not, because of Galileo's principle, measure absolute velocity. Hence, there is no way to correct the occurrence of a velocity error in an algorithm using inertial sensors only. The use of the local radio environment could potentially give the velocity information, assuming a trustworthy map of the local radio environment can be constructed. The success of construction such a map, is highly dependent on how well the imperfections in the hardware can be modeled and estimated. However, the fundamental performance limits of the joint system are not known, neither how hardware imperfections in both IMU and radio affect the result.

1.6 Contributions

This thesis contains the following contributions.

- Statement of a novel technique for joint pose and radio channel estimation.
- Development of a state space model that is suitable for sensor fusion, combining pose and a ray-traced based radio channel representation.
- Development and evaluation of suitable sensor fusion algorithms, for the developed model using both simulation and experimental data.

- Evaluation of two different sparse convex optimization solutions to the angle of arrival problem.
- Investigation of fundamental limitations of the problem using Cramér-Rao bounds for the joint estimation problem taking hardware imperfections into account.

Publications

The thesis is based on the following publications.

Mannesson, A., M. A. Yaqoob, B. Bernhardsson, and F. Tufvesson (2012). "Indoor positiong using IMU and radio". *International Conference on Systems, Signals and Image Processing (IWSSIP 2012)*, pp. 32–35.

Yaqoob, M. A., A. Mannesson, F. Tufvesson, and B. Bernhardsson (2013). "Direction of arrival estimation with arbitrary virtual antenna arrays using low cost inertial measurement unit". *Accepted for publication in Proceedings of IEEE International Conference on Communications 2013*.

For the first publication, the author has contributed with modeling and algorithms, similar to what is presented here. M.A. Yaqoob contributed with the measurements used for evaluation. For the second publication, the author mainly contributed with measurements and development of the algorithms. B. Bernhardsson and F. Tufvesson contributed on both publications with ideas and reviewing of manuscripts.

The current work was also presented on the SWE-CTW conference at KTH, Stockholm, SWEDEN in 2011 and at the ELLIIT workshop in Linköping, SWEDEN in 2012.

1.7 Outline

Chapter 2 describes basic radio transmission properties and a general model of the radio channel for MIMO systems. By making some assumptions and approximations, this general model is used as the basis for the ray-traced based radio channel model. Chapter 3 develops the nonlinear joint pose and ray-traced based radio channel state space model that can be used with the sensor fusion algorithms. Chapter 4 presents suitable algorithms for the nonlinear state space estimation problem, batch approaches to the classic angle of arrival estimation problem, and the Cramér-Rao bound for the estimation problem. Chapter 5 discusses implementation specific details of the estimation algorithms and hardware requirements. Chapter 6 presents the results with subsequent analysis. Chapter 7 describes the hardware used and also how the gathering of experimental data is done. Results from different experiments are presented and analyzed with promising results proving potential

for practical feasibility of the suggested method. Chapter 8 summarizes the work and presents ideas for the future.

2

Radio Channel Model

2.1 Introduction

For wireless communication, at least one transmitter (TX) and one receiver (RX) unit is needed. The transmission medium between the two is called the radio channel. Such a scenario is depicted in Figure 2.1. If the transmitter transmits a sinusoidal signal

$$U(t) = A(t)\cos(2\pi f_c t + \varphi(t)) = \mathbb{R}\{u(t)\exp(i2\pi f_c t)\} \tag{2.1}$$

where f_c is the carrier frequency, then $A(t)$ and $\varphi(t)$ are the amplitude and argument of the information $u(t) \in \mathbb{C}$ modulated onto the carrier signal. The signal $U(t)$ is referred to as the RF signal. Assuming the transmitter is stationary and transmitting a signal as in (2.1), the receiver placed at a distance d from the transmitter will, in free space, receive a signal as

$$Y(t) = A(t)a(t)\cos(2\pi f_c t + \varphi(t) - \frac{2\pi}{\lambda}d) \tag{2.2}$$

where λ is the wavelength of the carrier frequency and $a(t)$ is the gain of the signal due to energy loss of the wave as it propagates [Molisch, 2005]. Wavelengths for different radio standards are summarized in Table 2.1. The received signal is phase shifted due to the distance between the transmitter and the receiver and the signal (2.2) is also known as the line of sight component since it is the direct path between the transmitter and the receiver.

To demodulate, *i.e.*, to remove the carrier frequency and retrieve the information transmitted, the receiver reverts the operations performed by the transmitter. A common receiver type is the IQ demodulator depicted in Figure 2.2. The receiver down converts the RF signal by mixing it with a locally generated signal $y_{LO}(t)$ with the same frequency f_c as the carrier in the RF signal. By adding a 90 degree phase shift to $y_{LO}(t)$ before mixing, two signals $y_i(t)$ and $y_q(t)$, which are called in-phase and quadrature signals respectively are obtained. After the down conversion and subsequent filtering,

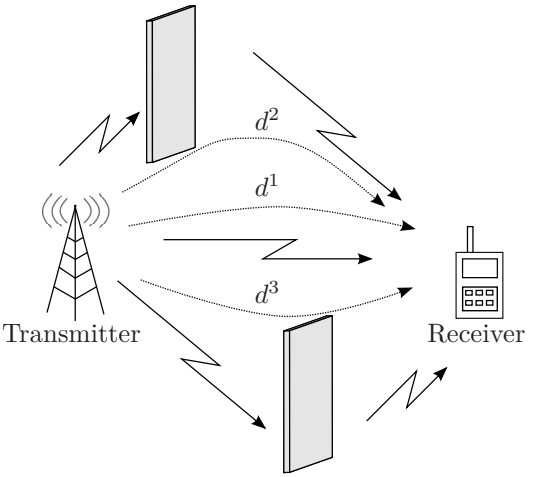

Figure 2.1 A wireless communication scenario with one transmitter, one receiver, and two scattering objects.

Radio Standard	Frequency [MHz]	Wavelength λ [cm]
GSM	900	33.3
3G	2100	14.3
Wi-Fi 802.11-b/g	2400	12.5
4G	2600	11.5
Wi-Fi 802.11-a	5500	5.5

Table 2.1 Wavelengths for a few different radio standards and frequency bands. Note that the cellular standards operate in more frequency bands than presented here.

an attenuated and phase shifted version of the signal modulated onto the carrier is obtained. This signal is also known as the baseband signal and can be written as a complex signal

$$\begin{aligned} y(t) = y_i(t) + iy_q(t) &= A(t)\exp\left(i\varphi(t)\right)a(t)\exp\left(-i\frac{2\pi}{\lambda}d\right) \\ &= u(t)a(t)\exp\left(-i\frac{2\pi}{\lambda}d\right). \end{aligned} \tag{2.3}$$

The baseband signal $y(t)$ contains one part which is the modulation $u(t)$ and the second part is the contribution from the radio channel.

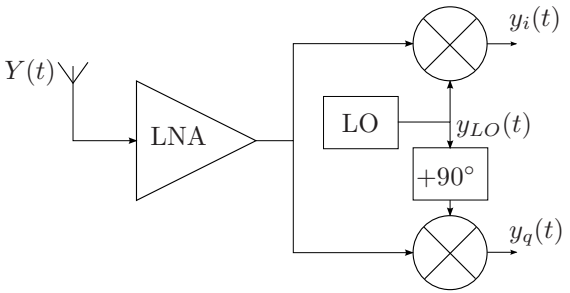

Figure 2.2 IQ demodulator with a low noise amplifier (LNA) on the input, a local oscillator (LO), and two mixers for retrieving the I and Q channel signals.

Small scale fading

Along the path from the transmitter to the receiver, the radio signal interferes with objects and is scattered, creating multipath components that will reach the receiver with different time delays and amplitudes. Let the distance from the transmitter to the r:th scattering object and further on to the receiver be d^r. If the distance from the receiver to the transmitter and scattering objects is assumed to be large, the impinging waves at the receiver can be considered to be plane waves, *i.e.*, the argument of the multipath component is independent of the position along the line, perpendicular to the propagation direction of the wave. This assumption is known as the far-field assumption [Krim and Viberg, 1996]. If all scattering objects and both transmitter and receiver are stationary, the signals are not subject to any Doppler shift. Thus, all impinging rays will have the same frequency and the received signal will be a superimposed attenuated version of the transmitted signal

$$y(t) = \sum_{r=1}^{R} a^r(t) \exp\left(-i\frac{2\pi}{\lambda} d^r\right) u(t), \tag{2.4}$$

where R is the total number of multipath components or rays that impinge on the receiver. Depending on the distance between the transmitter, scattering objects, and receiver the individual components in (2.4) will create constructive or destructive interference at the location of the receiver. This effect is called small scale fading since the fading pattern changes rapidly over short distances. The fading pattern creates what can be seen as a virtual map over the radio landscape, see figures 2.3, 2.4, and 2.5 wherein the number of impinging rays is one, two, and three respectively. In the figures, the real and imaginary parts, as well as the argument of the received complex signal (2.4), are shown as a function of the location of the receiver.

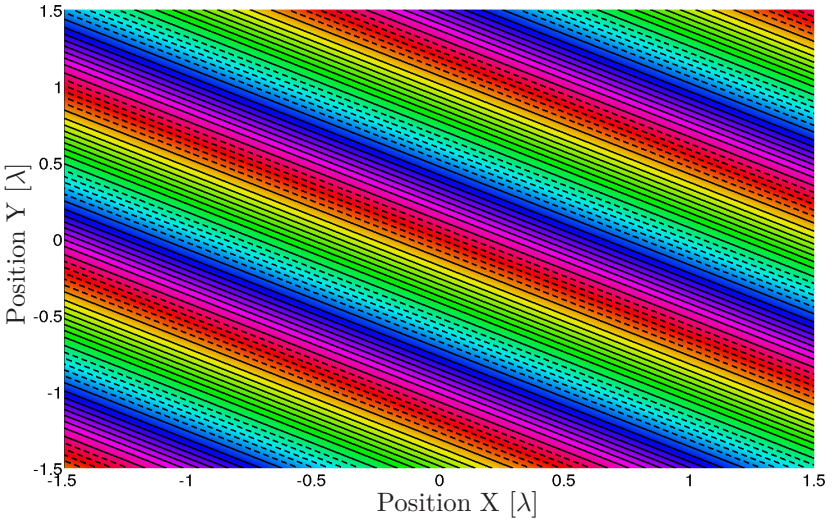

Figure 2.3 Map of the radio channel with one impinging ray with level curves for the real (-) and complex (- -) value of the received complex signal $y(t)$. The colors indicate argument.

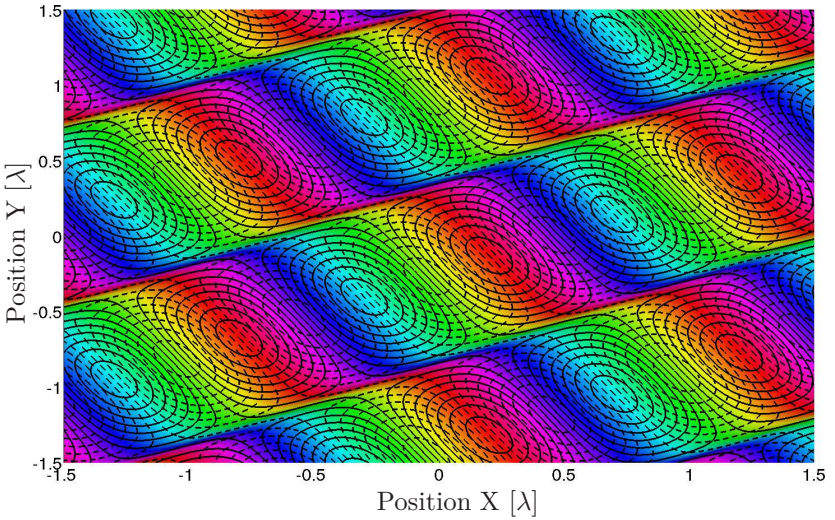

Figure 2.4 Same as Figure 2.3 but with two impinging rays.

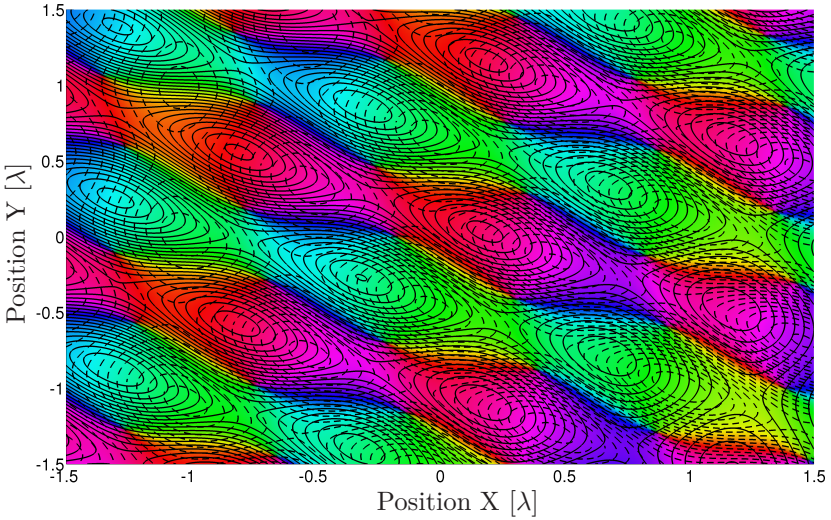

Figure 2.5 Same as Figure 2.3 but with three impinging rays.

The map in Figure 2.3 shows interesting characteristics of the radio channel. The far field assumption is clearly visible as straight lines of the color pattern where the argument is constant in the direction perpendicular to the impinging ray. Hence, the argument of the received signal will not give any information about the position perpendicular to the direction of the impinging ray. Further, if the receiver is moved λ in the direction of the ray, the argument of the signal revolves 2π during the movement and is back to the same value as it was when the movement was initiated.

In Figure 2.4, two rays impinging the receiver are modeled. The constant argument lines have now become ”wavy” due to superposition between the two rays. There are still areas wherein the argument is constant but now the real and imaginary parts of the received signal are changing. This information can be used to distinguish two points having equal argument from each other. Finally, for the case with three rays in Figure 2.5, the pattern becomes even more involved. There are several positions in the plane that will be indistinguishable from each other looking at the real and complex value of the received signal. Hence, the map of the radio environment alone, will not provide a single location of where the receiver is located but rather multiple possible locations. This will have implications for estimating the position of the receiver in the radio channel later on.

2.2 Modeling of MIMO radio channels

The simple case of the radio channel presented in the previous section, can be made more general to cover a scenario where there are several transmitters and receivers present. This scenario is known as Multiple-Input Multiple-Output (MIMO) and it is used in modern cellular networks. The ray-traced based radio channel model used here is more advanced than traditionally used, but it is becoming more frequent lately since is has the advantage of producing spatial models needed for MIMO systems. The derivation presented here follows [Pedersen, 2009] closely.

Figure 2.6 shows a MIMO scenario with M transmitters, N receivers, and two scattering objects. The transmitted and received signal can be represented with their complex baseband signals respectively introduced in (2.3) as

$$u(t) = \begin{bmatrix} u_1(t) \\ \vdots \\ u_m(t) \\ \vdots \\ u_M(t) \end{bmatrix} \quad \text{and} \quad y(t) = \begin{bmatrix} y_1(t) \\ \vdots \\ y_n(t) \\ \vdots \\ y_N(t) \end{bmatrix}, \tag{2.5}$$

where $u_m(t)$ is the input signal of transmit antenna m and $y_n(t)$ the output signal of receiver antenna n, see [Proakis and Salehi, 2002]. The observed signal $y(t)$ will then be

$$y(t) = s(t) + w(t), \tag{2.6}$$

where $s(t)$ is a u-dependent component as in (2.3) and $w(t)$ is additive complex white Gaussian noise as

$$w(t) \sim \mathcal{N}(0, \sigma^2/2) + i\mathcal{N}(0, \sigma^2/2) \triangleq \mathcal{CN}(0, \sigma^2), \tag{2.7}$$

where $\mathcal{N}(0, \sigma^2/2)$ is a white Gaussian noise process with zero mean and variance $\sigma^2/2$. The total noise power in $w(t)$ will then be σ^2. The description of the noise can represent different things, *e.g.*, thermal noise in the receiver or interference in the radio channel.

The delay-spread function

As mentioned in Section 2.1, the scattering objects along the path from the transmitter to the receiver will create multipath components at the receiver. Assuming a continuum of multipath components, the signal component $s(t)$ can be described by

$$s(t) = \int h(t, \tau) u(t - \tau) d\tau, \tag{2.8}$$

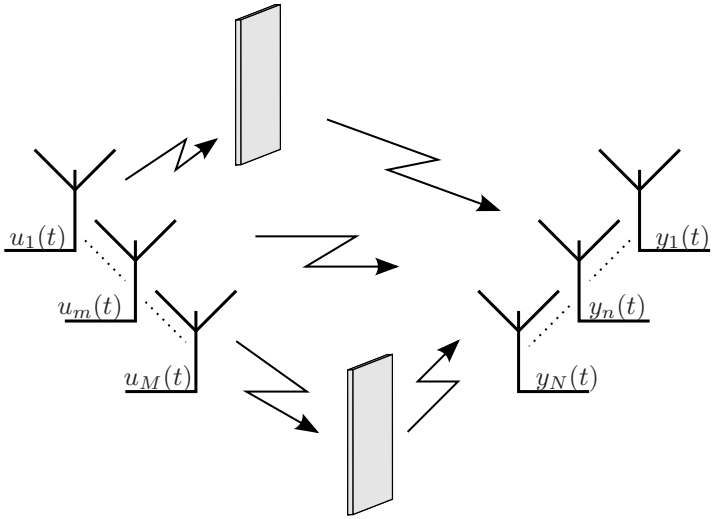

Figure 2.6 MIMO scenario with M transmitters to the left and N receivers to the right. There are also two scattering objects creating multipath components arriving at the receiver array.

where the integral kernel $h(t,\tau) \in \mathbb{C}^{N\times M}$ is called the *delay-spread function* and τ is the time delay in the channel [Pedersen, 2009]. A schematic of the channel operations is presented in Figure 2.7.

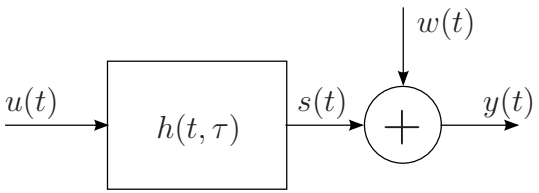

Figure 2.7 The radio channel can be modeled as a LTV system with additive complex valued white Gaussian noise $w(t)$. The input to the channel is the baseband equivalent $u(t)$ while the output is $y(t)$. The channel is described by the delay-spread function $h(t,\tau)$.

Assuming that the channel is time-invariant, *i.e.*, the integral kernel is constant over time, it has a delay-spread function of the form $h(t,\tau) \triangleq h_1(\tau), \forall t$. The signal component of the channel is then

$$s(t) = \int h_1(\tau)u(t-\tau)d\tau. \tag{2.9}$$

Further, the delay-spread function of a *non-dispersive channel* is of the form $h(t,\tau) \triangleq h_2(t)\delta(\tau-\tau_0)$ and the signal component for such a channel becomes

$$s(t) = h_2(t)u(t-\tau_0). \tag{2.10}$$

By combining the time-invariant and the non-dispersive channel properties, the integral kernel has the form of $h(t,\tau) \triangleq h_3\delta(\tau-\tau_0)$. Thus, the signal component of the channel will be

$$s(t) = h_3u(t-\tau_0). \tag{2.11}$$

Time-invariance may be assumed for channels where changes occur slowly compared to the considered transmission time duration. Similarly, a channel may be considered non-dispersive if the difference in time delay between the first and last component is significantly smaller than the inverse of the bandwidth B of the transmitted signal, *i.e.*, if

$$\tau_{max} - \tau_{min} \ll \frac{1}{B}. \tag{2.12}$$

Antenna modeling

In this thesis, for simplicity, it is assumed that the antennas are isotropic, *i.e.*, the radio channel will not depend on the rotation of the receiver which simplifies the models significantly. However, for future use, the models describing the influence of the antennas on the radio channel model are presented here.

By assuming that the antennas at the transmitters and the receivers are time-invariant and non-dispersive with respect to their field pattern, the antennas can be described by their direction dependent complex transfer functions. For each antenna element, the complex electric field patterns is a two-dimensional complex function. For the i:th TX antenna element, it is described by

$$\begin{bmatrix} c^{\theta}_{TX,i}(\Omega) \\ c^{\phi}_{TX,i}(\Omega) \end{bmatrix}, \tag{2.13}$$

where $c^{\theta}_{TX,i}(\Omega)$ and $c^{\phi}_{TX,i}(\Omega)$ are the horizontal and vertical components of the complex electric field pattern respectively and Ω is the direction vector defined in Figure 2.8.

Define the TX antenna steering matrix as the $2 \times M$ matrix

$$C_{TX} = \begin{bmatrix} c^{\theta}_{TX,1} & \cdots & c^{\theta}_{TX,m} & \cdots & c^{\theta}_{TX,M} \\ c^{\phi}_{TX,1} & \cdots & c^{\phi}_{TX,m} & \cdots & c^{\phi}_{TX,M} \end{bmatrix}, \tag{2.14}$$

where θ denotes azimuth and ϕ elevation. Similarly, for the RX antenna, a $2 \times N$ steering matrix C_{RX} is introduced. The delay-spread radio channel function can be written as

$$h(t,\tau) = \iint C_{RX}(\Omega_{RX})^T h(t,\tau,\Omega_{TX},\Omega_{RX}) C_{TX}(\Omega_{TX}) d\Omega_{TX} d\Omega_{RX}, \tag{2.15}$$

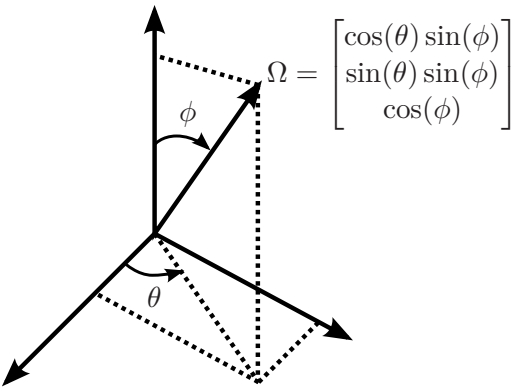

Figure 2.8 Definition of the direction vector Ω. Note that the notation of the angles is different than commonly used.

where the 2×2 kernel $h(t, \tau, \Omega_{TX}, \Omega_{RX})$ is the *bi-directional delay spread function* of the radio channel and ^{T} denotes matrix transpose. It describes the propagation properties for different combinations of transmit-receive polarization pairs as

$$h(t, \tau, \Omega_{TX}, \Omega_{RX}) = \begin{bmatrix} h^{\theta\theta}(t, \tau, \Omega_{TX}, \Omega_{RX}) & h^{\theta\phi}(t, \tau, \Omega_{TX}, \Omega_{RX}) \\ h^{\phi\theta}(t, \tau, \Omega_{TX}, \Omega_{RX}) & h^{\phi\phi}(t, \tau, \Omega_{TX}, \Omega_{RX}) \end{bmatrix}. \quad (2.16)$$

Multipath propagation assumption

Multipath propagation was introduced before to describe the result of scattering. It is a commonly used model which is intuitive and fits many other observed phenomena like channel delay and Doppler power spectra. The multipath assumption also allows for physical interpretation of observed changes in the radio channel due to movement of the receiver.

The received signal is modeled as a superposition of R signal components due to waves propagating via different paths

$$s(t) = \sum_{r=1}^{R} s^r(t), \quad (2.17)$$

where $s^r(t)$ denotes the complex contribution by path r. A path consists of a trajectory from one transmitter to one receiver along which the radio wave interacts with a number of scattering objects. For a multipath model, the delay-spread function is decomposed as

$$h(t, \tau) = \sum_{r=1}^{R} h^r(t, \tau), \quad (2.18)$$

where $h^r(t,\tau)$ denotes the delay-spread function along path r. If the plane-wave assumption holds for each path, the individual delay-spread functions become

$$h^r(t,\tau) = \iint C_{RX}(\Omega_{RX})^T h^r(t,\tau,\Omega_{TX},\Omega_{RX}) C_{TX}(\Omega_{TX}) \partial\Omega_{TX}\partial\Omega_{RX}, \tag{2.19}$$

and therefore

$$h(t,\tau) = \iint C_{RX}(\Omega_{RX})^T \sum_{r=1}^{R} h^r(t,\tau,\Omega_{TX},\Omega_{RX}) C_{TX}(\Omega_{TX}) \partial\Omega_{TX}\partial\Omega_{RX}. \tag{2.20}$$

Specular multipath representation

A path is called specular when its delay-spread function has the form

$$\begin{aligned} &h^r(t,\tau,\Omega_{TX},\Omega_{RX}) = \\ &A^r \exp(-i2\pi\nu^r t)\delta(t-\tau^r)\delta(\Omega_{TX}-\Omega^r_{TX})\delta(\Omega_{RX}-\Omega^r_{RX}), \end{aligned} \tag{2.21}$$

where A^r is a complex 2×2 polarization matrix, ν^r is the Doppler frequency, τ^r is the delay, Ω^r_{TX} is the angle of departure, and Ω^r_{RX} is the angle of arrival of path r respectively.

Inserting this expression in (2.19) and integrating over Ω_{TX} and Ω_{RX} yields

$$h^r(t,\tau) = C_{RX}(\Omega^r_{RX})^T A^r C_{TX}(\Omega^r_{TX})\delta(\tau-\tau^r)\exp(-i2\pi\nu^r t). \tag{2.22}$$

Thus, path r is determined by the parameter set $(A^r,\Omega^r_{TX},\Omega^r_{RX},\tau^r,\nu^r)$. Since A^r is a complex matrix with 4 elements and the directions can be described by two real parameters each, a total of 14 parameters is needed for each path. For R paths, $14R$ parameters must be estimated. To simplify the model and reduce the number of parameters, some assumptions will be made.

Start by assuming all paths have zero Doppler shifts, *i.e.*, $\nu^r = 0, \forall r$. This is the case if all multipath components have been scattered by stationary objects. The next assumption is isotropic antennas which leads to

$$C_{RX,n}(\Omega^r_{RX})^T A^r C_{TX,m}(\Omega^r_{TX}) = \alpha^r_{n,m}, \tag{2.23}$$

where $\alpha^r_{n,m}$ is a complex scalar for each transmitter/receiver pair.

Next, assume that all transmitters are stationary, *i.e.*, the delay in the channel τ^r is only dependent on the position of the receiver. To establish a relation between how a common translation of all receiver antennas affect the delay of the signal, the scenario in Figure 2.9 is considered. Introduce the

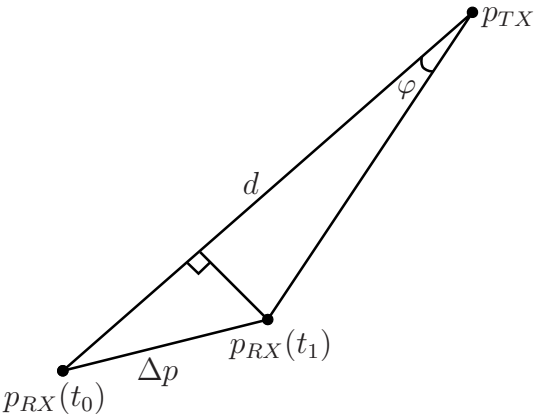

Figure 2.9 The receiver antenna is moved from location $p_{RX}(t_0)$ to $p_{RX}(t_1)$ and a stationary transmitter is placed in p_{TX}.

location of the receiver at time t as $p_{RX}(t) \in \mathbb{R}^3$ and introduce the vectors $\Delta p \triangleq p_{RX}(t_1) - p_{RX}(t_0)$ and $d \triangleq p_{TX} - p_{RX}(t_0)$, where p_{TX} is the location of the transmitter.

If the vector Δp is projected onto vector d as

$$p' = \frac{\langle \Delta p, d \rangle}{\|d\|^2} d \tag{2.24}$$

where $\langle *, * \rangle$ denotes scalar product, the distance between the stationary transmitter in p_{TX} and the receiver in $p_{RX}(t_1)$ is

$$\|p_{TX} - p_{RX}(t_1)\| = \frac{\|d - p'\|}{\cos(\varphi)}. \tag{2.25}$$

If $\|\Delta p\| \ll \|d\|$, φ becomes small and thus

$$\|p_{TX} - p_{RX}(t_1)\| \approx \|d - p'\| = \|d - \frac{\langle d, \Delta p \rangle}{\|d\|^2} d\| = \|d\| - \langle \frac{d}{\|d\|}, \Delta p \rangle \tag{2.26}$$

The vector $\dfrac{d}{\|d\|}$ is the vector Ω_{RX} pointing in the direction of the impinging ray. If the scenario is limited to $\mathbb{R}^2$, denote the position of the receiver n at time t by $p_n(t) \in \mathbb{R}^2$ and a unit vector as

$$\mathsf{e}(\theta) \triangleq [\cos(\theta), \sin(\theta)]^T. \tag{2.27}$$

The azimuth angle θ is hereafter called angle of arrival (AoA). With these assumptions, the time delay at receiver n of ray r can be written

$$\tau_{n,m}^r = c_{n,m}^r - \frac{1}{c} \langle p_n(t), \mathsf{e}(\theta^r) \rangle, \tag{2.28}$$

where c^r is a constant for path r and c is the speed of light. Using these assumptions, the following model for the base-band equivalent delay-spread function $h^r_{n,m}(t,\tau)$ for transmitter/receiver pair (m,n) is according to

$$h^r_{n,m}(t,\tau) = \alpha^r_{n,m}\delta(\tau - c^r_{n,m} + \frac{1}{c}\langle p_n(t), \mathsf{e}(\theta^r)\rangle. \tag{2.29}$$

This means that the relation between the input RF signal to the channel

$$U(t) = \Re\{\exp[2\pi i f_c t]u(t)\} \tag{2.30}$$

and output RF signal of the channel

$$Y(t) = \Re\{\exp[2\pi i f_c t]y(t)\}, \tag{2.31}$$

where $u(t)$ and $y(t)$ are the base-band equivalents of $U(t)$ and $Y(t)$ respectively, is given by

$$y_n(t) = \sum_{r=1}^{R} \alpha^r_{n,m} \exp\left(-i2\pi\frac{f_c}{c}\langle p_n(t), \mathsf{e}(\theta^r)\rangle\right) u_m(t + c^r_{n,m} - \frac{1}{c}\langle p_n(t), \mathsf{e}(\theta^r)\rangle). \tag{2.32}$$

If the baseband signal $u_m(t)$ is slowly varying in the sense that it has its energy in the frequency interval $|f| \leq B$ then the approximation

$$u_m(t + c^r_{n,m} - \frac{1}{c}\langle p_n(t), \mathsf{e}(\theta^r)\rangle) \approx u_m(t + c^r_{n,m}) \tag{2.33}$$

is valid if $\tau_n := \frac{1}{c}\langle p_n(t), \mathsf{e}(\theta^r)\rangle$ satisfies

$$\tau_{n,max} - \tau_{n,min} \ll \frac{1}{B}. \tag{2.34}$$

This is the *narrowband assumption*. If the signal is allowed to change rapidly, thereby covering a larger frequency band, the difference between the absolute delays of the rays can be resolved. This gives TOA information when transmitters and receivers are time synchronized and TDOA information otherwise. This is possible in a wideband system. However, in this thesis the investigation is limited to the narrowband case, even though the wideband case would supply more information about the radio channel.

If the transmitter is transmitting a constant baseband signal, *i.e.*, $u_m = \exp(i\varphi_{TX})$, the dependence on $c^r_{n,m}$ dissappears and the contribution from the constant phase φ_{TX} can be included in the complex amplitude $\alpha^r_{n,m}$. Under these assumptions, the base-band model in (2.32) simplifies to

$$y_n(t) = \sum_{r=1}^{R} \alpha^r_{n,m} \exp\left(-i2\pi\frac{f_c}{c}\langle p_n(t), \mathsf{e}(\theta^r)\rangle\right), \tag{2.35}$$

where $p_n(t)$ denotes the position of the n:th receiver at time t, $\alpha^r_{n,m}$ is the complex amplitude of path r, and $\mathsf{e}(\theta^r)$ is a unit vector pointing in the azimuth direction of θ^r. In this thesis, the analysis is restricted to a receiver array consisting of only one receiver element that can be moved arbitrarily. This configuration is referred to as a *virtual array antenna*, see [Molisch, 2005].

The delay-spread function of a typical radio channel with a line of sight component arriving first and two scattered components arriving later is shown in Figure 2.10. The channel shows a strong line of sight component together with two rays arriving around 0.75 μs and 2 μs later. The curvature is due to the movement of the receiver and that thereby the distances to the transmitter and the scattering objects are changing.

Instead of using a time domain model, a frequency domain model $H(t, f)$ can be obtained by Fourier transforming the delay-spread function in (2.29) as

$$H(t,f) = \int_{-\infty}^{\infty} h(t,\tau)\exp(-i2\pi f\tau)d\tau = \sum_{r=1}^{R} \alpha^r(t)\exp\left(-i2\pi f\tau^r\right), \qquad (2.36)$$

see Figure 2.11. A typical transfer function of the radio channel was shown earlier in Figure 1.3.

2.3 Receiver imperfections

The transmitter and the receiver in the derivation above were both assumed to be perfect in sense of transmitter frequency and local oscillator frequency. A closer look at the receiver reveals that especially noise in the local oscillator, see Figure 2.2, will be transformed into a phase/frequency error of the receiver. The local oscillator output of the receiver can be modeled as

$$y_{LO}(t) = \beta\cos(2\pi f_c t + \xi(t)), \qquad (2.37)$$

where $\xi(t)$ is a perturbation of the phase of the output signal and β is the amplitude. If $\xi(t)$ is assumed to be small, then

$$y_{LO}(t) \approx \beta\cos(2\pi f_c t) - \beta\xi(t)\sin(2\pi f_c t). \qquad (2.38)$$

Thus, the perturbation is modulated onto the carrier frequency and this noise is called phase noise. It is usually quantified as the noise power in a 1 Hz band around the carrier frequency plus an offset of Δf. The spectral noise density becomes

$$\mathcal{L}(\Delta f) = 10\log\left(\frac{S_\xi(f_c+\Delta f)}{P(f_c)}\right) \quad \left[\frac{\text{dBc}}{\text{Hz}}\right] \qquad (2.39)$$

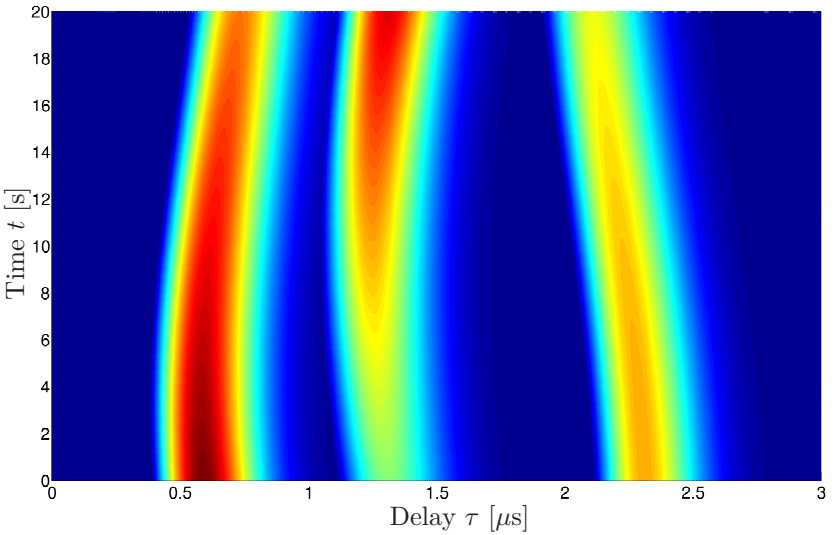

Figure 2.10 The delay-spread function of a radio channel with delay τ on the x-axis and time t on the y-axis. The color indicates $|h(t,\tau)|$. Three multipath components give responses at 0.5 μs, 1.3 μs, and 2.3 μs respectively. The curvature is due to the movement of the receiver.

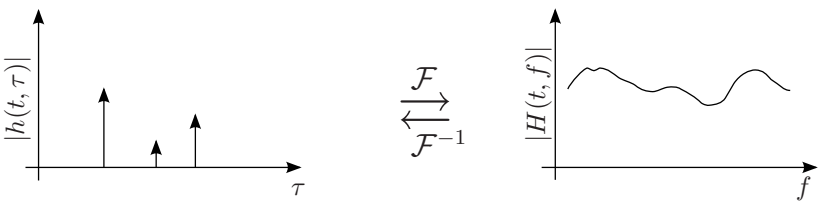

Figure 2.11 Time domain and frequency domain radio channel model.

where $P(f_c)$ denotes the power in the carrier frequency and $S_\xi(f)$ is the noise power of $\xi(t)$ at frequency f. A typical output noise spectrum of the local oscillator is shown in Figure 2.12.

The noise in the oscillator can usually be divided into two parts; a noise floor with flat noise power at large offset frequencies and a $1/f^2$ part near the carrier. The former part is due to thermal noise in the circuits while the later comes from electronic noise in the oscillator. As in [Staszewski et al., 2005], the noise floor part can be seen as an uncertainty of the phase in the oscillator output (2.38). Since the error from one time step to another is approximately independent, it is modeled as white Gaussian noise on $y_{LO}(t)$. Furthermore, the $1/f^2$ part is modeled as an accumulative process leading

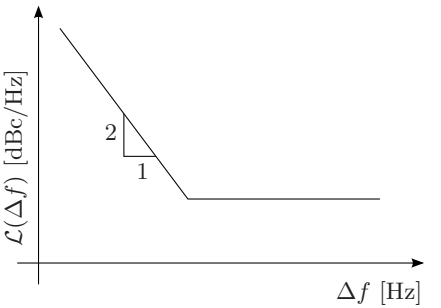

Figure 2.12 Output phase noise from receiver LO as a function of frequency offset from carrier.

to a drift in the phase of the oscillator. To model this effect, an integrator

$$\zeta(t) = \int_0^t \delta_f(\tau) d\tau \tag{2.40}$$

is introduced, where $\delta_f(t)$ is a frequency error, and added on the argument of (2.35). The received signal can now be written as

$$y(t) = \sum_{r=1}^{R} \alpha^r \exp\left(-i[\frac{2\pi}{\lambda}\langle p(t), \mathsf{e}(\theta^r)\rangle + \zeta(t)]\right) + w(t), \tag{2.41}$$

where $p(t)$ is the location of the receiver at time t with respect to its initial position $p(t_0)$. The derived equation gives a connection between the AoA of an impinging ray and how the channel fading pattern will vary with the position of the receiver. This equation will be referred to as the measurement equation in subsequent chapters.

Several other types of imperfections exist in transmitters and receivers but they are believed to be of less importance and their effect is assumed to be covered by the white Gaussian noise $w(t)$. However, it is important to model phase noise carefully since it deteriorates the virtual map slowly and thereby limits the information the radio signal gives to the sensor fusion algorithms for improved pose estimation.

3

Joint Pose and Radio Channel Modeling

3.1 Inertial measurement unit

An IMU consists of accelerometers and gyroscopes and optionally magnetometers. In order to measure acceleration and rotation around all axes, three accelerometers and gyroscopes are needed. The gyroscope measures the angular velocity of the IMU's body coordinate frame with respect to a static coordinate frame. Rotation is thereby defined as the orientation of the body coordinate frame with respect to a static coordinate frame. The accelerometer measures the forces acting upon the device, in the coordinate frame of the IMU. Acceleration of the device leads to a displacement between the static coordinate frame and the body coordinate frame called translation. Rotation and translation is illustrated in Figure 3.1. The fixed coordinate frame is the coordinate system relative to which position and orientation is defined and it is hereafter called the world frame while the coordinate system attached to the moving body is called the body frame. All frames throughout the thesis are assumed to be right handed.

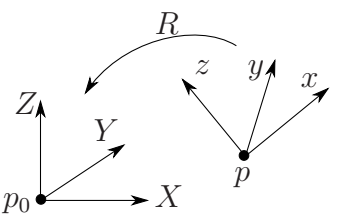

Figure 3.1 Translation and rotation of the body frame in relation to the world frame. The world frame is fixed in p_0 while the body frame is translated to p. The rotation matrix R transforms positions in body frame to the world frame.

IMU noise sources

Various types of disturbances distort the IMU measurements. The main distortion contributors are random noise, bias, calibration errors, and temperature effects [Woodman, 2010]. Both the accelerometer and gyroscope are subject to these noise sources.

Random noise The random noise from the accelerometer and gyroscope circuits are modeled as zero mean white Gaussian noise. For the gyroscope, the random noise will be integrated once when calculating the orientation resulting in so called angular random walk. The standard deviation of the orientation will therefore grow $\propto t^{1/2}$. The unit for the standard deviation of the angular random walk is usually given as $^\circ/\sqrt{\text{h}}$. However, the mean value, *i.e.*, the orientation, is unaffected by this noise since the integral of zero mean white noise has zero mean.

For the accelerometer, the random noise is integrated once into a velocity random walk noise source. The unit for the standard deviation of the noise becomes $\text{m/s}/\sqrt{\text{h}}$. As mentioned before, position is obtained by double integration of the accelerometer signal. Thus, the noise from the accelerometer will also be integrated twice and the standard deviation of the position estimate will grow $\propto t^{3/2}$. The mean value is left unaffected due to the same reason as for the gyroscope.

Constant and varying bias If the IMU is kept at rest, the mean value of the measurements from the gyroscope might differ from zero. Possible reasons for this deviation are scale errors or periodic behavior in the circuits. This offset is called bias and usually consists of one constant part and one slowly time varying part [Woodman, 2010]. The constant part can quite easily be removed with a calibration scheme such as in [Skog and Händel, 2006]. Any remaining calibration errors on the gyroscope will be integrated once leading to an orientation error that grows $\propto t$. The effect on the position is an error that grows $\propto t^3$ due to the constant error. The time varying part must be modeled and is usually done so with a first order Gaussian random walk process on the measurements, see [Woodman, 2010] and [Gustafsson, 2010]. For the gyroscope, this noise will be integrated once more into a second order random walk process. The standard deviation of the angular random walk process will then have the unit of $^\circ/\text{h}^{3/2}$.

The same applies to the accelerometer; the constant part of the bias can be removed by calibration but any remaining error will be integrated twice to obtain position. The time varying offset is also modeled with a first order random walk which yields a third order random walk in the estimated position. The unit for the standard deviation of the position noise process becomes $\text{m}/\text{h}^{5/2}$.

Note that in order to simulate a true bias stability process with the units

of °/h and m/h^2 for gyroscope and accelerometer respectively, a noise source with intensity 1/f must be used. Due to the challenge to simulate this, only 1/f^2 is considered here giving the noise sources described previously. The chosen noise sources have other properties but it is deemed to capture the noise behavior of the IMU needed in simulation during suitable time intervals.

Temperature effects Temperature variations affect the accelerometers and gyroscopes as changing bias and noise levels, etc. The temperature dependence on the circuits can be modeled but this model will be difficult to obtain since there is no temperature information available from the device used. Thus, the temperature dependence on the sensors of the IMU is left unmodeled.

Allan variance

To determine which noise sources that are present in the measured signals, the technique known as Allan variance can be used. A thorough description of the technique can be found in [IEEE Std 952-1997, 1998]. To characterize the IMU, data is gathered over a long period of time when the IMU is kept at complete rest. The data sequence is then divided into N bins of length T. For each bin, the mean value is calculated giving a set of averages denoted by $[a(T)_1, \ldots, a(T)_N]$. The Allan variance for the averaging time T is calculated as

$$\mathrm{AVAR}(T) = \frac{1}{2(N-1)} \sum_{n=1}^{N-1} (a(T)_{n+1} - a(T)_n)^2. \tag{3.1}$$

The Allan deviation, $\mathrm{AD}(T) \triangleq \sqrt{\mathrm{AVAR}(T)}$, is plotted against the averaging interval T. A typical such curve is shown in Figure 3.2.

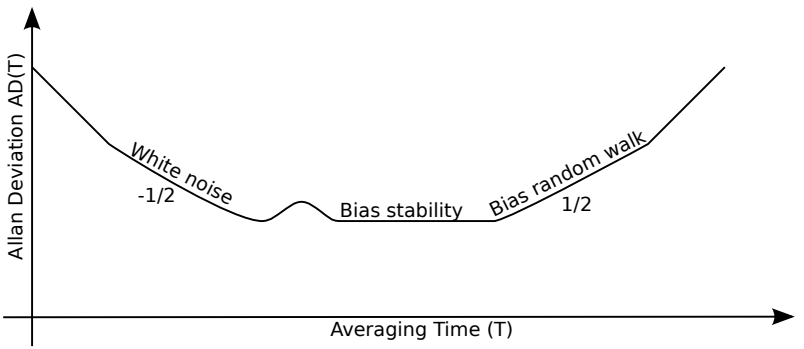

Figure 3.2 Typical log-log plot of the Allan deviation as a function of averaging interval length T [IEEE Std 952-1997, 1998].

From the Allan deviation plot, the white noise intensity and bias stability can be obtained as well as other noise sources. The white noise gives a slope of -0.5 at short averaging times. As more samples are lumped together and averaged, the variance of the mean value becomes lower. The bias stability can be determined by the flat part in the plot and the bias random walk is seen as the ramp with slope 0.5. If the signal contains correlated noise, it will be visible as a hump in the plot. In this work, random noise and bias are considered to be the two most important noise sources and are therefore modeled. The bias is modeled as a first order random walk process, individual for each sensor axis. The measurements from the 3-axis accelerometer and gyroscope in the body frame are denoted by $u_a^b(t) \in \mathbb{R}^3$ and $u_\omega^b(t) \in \mathbb{R}^3$ respectively and become

$$u_a^b(t) = a^b(t) + \delta_a(t) + n_a(t), \tag{3.2}$$

$$u_\omega^b(t) = \omega^b(t) + \delta_\omega(t) + n_\omega(t), \tag{3.3}$$

where $a^b(t) \in \mathbb{R}^3$ are the acceleration forces acting on the three axes of the device measured in $\mathrm{m/s^2}$ and $\omega^b(t) \in \mathbb{R}^3$ is the angular velocity of the device measured in rad/s. The $\delta_a(t) \in \mathbb{R}^3$ and $\delta_\omega(t) \in \mathbb{R}^3$ are the first order random walk noise processes of the accelerometers and gyroscopes respectively. They are modeled as

$$\dot{\delta}_a(t) = n_{\delta_a}(t), \tag{3.4}$$

$$\dot{\delta}_\omega(t) = n_{\delta_\omega}(t), \tag{3.5}$$

where

$$n_{\delta_a}(t) \sim \mathcal{N}(\mathbf{0}, \Sigma_{\delta_a}), \tag{3.6}$$

$$n_{\delta_\omega}(t) \sim \mathcal{N}(\mathbf{0}, \Sigma_{\delta_\omega}) \tag{3.7}$$

with diagonal covariance matrices of appropriate sizes. The white noise processes $n_a(t) \in \mathbb{R}^3$ and $n_\omega(t) \in \mathbb{R}^3$ are white noise processes as

$$n_a(t) \sim \mathcal{N}(\mathbf{0}, \Sigma_a), \tag{3.8}$$

$$n_\omega(t) \sim \mathcal{N}(\mathbf{0}, \Sigma_\omega), \tag{3.9}$$

where Σ_a and Σ_ω are diagonal covariance matrices of appropriate sizes.

3.2 Kinematic modeling

Kinematics is the dynamical description of how bodies move. To be able to predict or evaluate the likelihood of rigid body movements, a kinematic model is of essence. The model derived here is for movements in three dimensions even though experiments and simulations in this thesis are carried out in two dimensions.

Rotation

There are two widely used ways of representing rotation, Euler angles and quaternions. Euler angles represent the rotation as three rotations around the coordinate axes. The Euler angles are easy to understand but suffer from singularities where two of the rotational axes coincide. The other representation, quaternions, does not have this shortcoming and will therefore be used in this thesis. A quaternion q is defined as

$$q \triangleq [q_0, q_1, q_2, q_3]^T = [q_0, \mathbf{q}]^T \in \mathbb{R}^4 \tag{3.10}$$

with the internal restriction

$$||q||_2 = 1. \tag{3.11}$$

The unit quaternion is defined as

$$q_{\mathbf{I}} \triangleq [1, 0, 0, 0]^T. \tag{3.12}$$

Multiplication of two quaternions is denoted by $\otimes$ and defined as

$$q \otimes r = \begin{bmatrix} q_0 \\ \mathbf{q} \end{bmatrix} \otimes \begin{bmatrix} r_0 \\ \mathbf{r} \end{bmatrix} = \begin{bmatrix} q_0 r_0 - \mathbf{q} \cdot \mathbf{r} \\ q_0 \mathbf{r} + r_0 \mathbf{q} + \mathbf{q} \times \mathbf{r} \end{bmatrix} \tag{3.13}$$

and the inverse of quaternion q is given by

$$q^{-1} \otimes q = q \otimes q^{-1} = q_{\mathbf{I}} \quad \Leftrightarrow \quad q^{-1} = \begin{bmatrix} q_0 \\ -\mathbf{q} \end{bmatrix} \tag{3.14}$$

Let $p^b = [p_x^b, p_y^b, p_z^b]^T$ be a vector in the body frame and q the quaternion describing the relation between the body and the world frame. Rotation of vector p^b from the body coordinate system to $p^w = [p_x^w, p_y^w, p_z^w]^T$ in the world frame is calculated as

$$\begin{bmatrix} 0 \\ p^w \end{bmatrix} = q \otimes \begin{bmatrix} 0 \\ p^b \end{bmatrix} \otimes q^{-1} = \begin{bmatrix} 0 \\ R(q) p^b \end{bmatrix}, \tag{3.15}$$

where $R(q)$ denotes a rotation matrix from body coordinates to world coordinates. The rotation matrix is given by

$$R(q) = \begin{bmatrix} q_0^2 + q_1^2 - q_2^2 - q_3^2 & 2q_1q_2 - 2q_0q_3 & 2q_1q_3 + 2q_0q_2 \\ 2q_1q_2 + 2q_0q_3 & q_0^2 - q_1^2 + q_2^2 - q_3^2 & 2q_2q_3 - 2q_0q_1 \\ 2q_1q_3 - 2q_0q_2 & 2q_2q_3 + 2q_0q_1 & q_0^2 - q_1^2 - q_2^2 + q_3^2 \end{bmatrix}. \tag{3.16}$$

Rotational dynamics

Let the orientation of a rigid body be represented by the quaternion q and let the angular velocity of the body be ω, see Figure 3.3. The continuous state

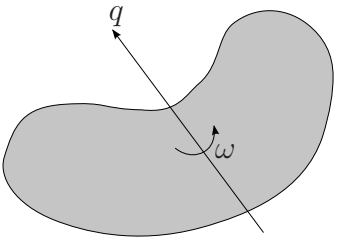

Figure 3.3 A rigid body with orientation described by quaternion q rotated with angular velocity ω.

dynamics for the quaternion is [Coutsias and Romero, 2004]

$$\dot{q}(t) = \frac{1}{2}\omega(t) \otimes q(t), \tag{3.17}$$

which can be written as matrix multiplications as

$$\dot{q}(t) = \frac{1}{2}P(q(t))\omega(t) = \frac{1}{2}Q(\omega(t))q(t), \tag{3.18}$$

where

$$P(q) = \begin{bmatrix} -q_1 & -q_2 & -q_3 \\ q_0 & -q_3 & q_2 \\ q_3 & q_0 & -q_1 \\ -q_2 & q_1 & q_0 \end{bmatrix} \tag{3.19}$$

and

$$Q(\omega) = \begin{bmatrix} 0 & -\omega_x & -\omega_y & -\omega_z \\ \omega_x & 0 & \omega_z & -\omega_y \\ \omega_y & -\omega_z & 0 & \omega_x \\ \omega_z & \omega_y & -\omega_x & 0 \end{bmatrix}. \tag{3.20}$$

By using the measurement model for the angular velocity of the IMU, (3.3) and substituting it into (3.18) the following equation is obtained

$$\dot{q}(t) = \frac{1}{2}Q(\omega^b(t))q(t) = \frac{1}{2}Q(u_\omega^b(t) - \delta_\omega(t) - n_\omega(t))q(t), \tag{3.21}$$

which together with the bias state of the gyroscope

$$\dot{\delta}_\omega(t) = n_{\delta_\omega}(t), \tag{3.22}$$

where $n_{\delta_\omega}(t)$ is a white Gaussian noise process, gives the dynamic model for rotations. A full description of quaternions and their dynamics can be found in [Kuipers, 1999].

Translational dynamics

For translation, there are several different motion models available [Rong Li and Jilkov, 2003]. If the movement of the object is limited, *e.g.*, a car can not drive sideways, there are models that include this limitation. In the current scenario, the choice is to assume minimal information about the movement of the device and therefore the classic Newton equations for free body movement are chosen as motion model

$$\dot{p}(t) = v(t), \tag{3.23}$$

$$\dot{v}(t) = a(t), \tag{3.24}$$

where $p(t) \triangleq [p_x(t), p_y(t), p_z(t)]^T$, and $v(t) \triangleq [v_x(t), v_y(t), v_z(t)]^T$ are the position and velocity in the world frame at time t respectively. The acceleration $u_a^b(t)$ is measured by the IMU and is used as an input signal to the system. Before the position and velocity states can be updated using the accelerometer measurements, they have to be rotated from the body frame to the world frame using (3.16), and gravity $\bar{g} \triangleq [0, 0, g]^T$ must be removed. These operations yield

$$a^w(t) = R(q(t))a^b(t) - \bar{g}. \tag{3.25}$$

Inserting the measurement model from (3.2) gives

$$\dot{p}(t) = v(t), \tag{3.26}$$

$$\dot{v}(t) = R(q(t))[u_a^b(t) - \delta_a(t) - n_a(t)] - \bar{g}, \tag{3.27}$$

$$\dot{\delta}_a(t) = n_{\delta_a}(t). \tag{3.28}$$

Discrete time dynamics

The rotational dynamics, (3.21) and (3.22), together with the translational dynamics in (3.26) to (3.28) are discretized as

$$p_{k+1} = p_k + T_s v_k + \frac{T_s^2}{2}\{R(q_k)[u_{a,k}^b + \delta_{a,k}] - \bar{g} + n_{a,k}\} \tag{3.29}$$

$$v_{k+1} = v_k + T_s\{R(q_k)[u_{a,k}^b + \delta_{a,k}] - \bar{g} + n_{a,k}\} \tag{3.30}$$

$$\delta_{a,k+1} = \delta_{a,k} + T_s n_{\delta_a,k} \tag{3.31}$$

$$q_{k+1} = [\mathbf{I}_4 + \frac{T_s}{2}Q(u_{\omega,k}^b + \delta_{\omega,k})]q_k + \frac{T_s}{2}P(q_k)n_{\omega,k} \tag{3.32}$$

$$\delta_{\omega,k+1} = \delta_{\omega,k} + T_s n_{\delta_\omega,k}, \tag{3.33}$$

where $\mathbf{I}_4$ is the unity matrix of size 4 and T_s is the sample time. In the discretization step, the sign on the bias states and the white noise processes for both accelerometer and gyroscope has been changed. Note that (3.32) does not preserve the relation (3.11). This will be dealt with when implementing algorithms for state estimation, see Chapter 5.

3.3 Radio channel dynamics

The radio channel model, introduced in Section 2.2, must similarly to the kinematics, be transformed into a dynamic model.

To keep the number of states to a minimum, the phase drift $\zeta(t)$ is added to the complex amplitude $\alpha^r(t), \forall r$. The complex amplitude is also separated into two individual states as

$$|\alpha^r(t)| \triangleq a^r(t) \quad \text{and} \quad \arg\{\alpha^r(t)\} \triangleq \phi^r(t). \tag{3.34}$$

The dynamic equation for $\phi^r(t)$ becomes

$$\dot{\phi}^r(t) = \delta_f(t), \tag{3.35}$$

where $\delta_f(t)$ is the unknown frequency error at time t. The absolute value and argument of the complex amplitude, the AoA, and the frequency error are all added to the state vector which now becomes

$$x = [p, v, \delta_a, q, \delta_\omega, \theta^1, \ldots, \theta^r, a^1, \ldots, a^r, \phi^1, \ldots, \phi^r, \delta_f]^T \in \mathbb{R}^{17+3R}, \tag{3.36}$$

where R is the number of multipath components of the radio channel. Since nothing is assumed to be known about how the amplitude, angle of arrival, and frequency error changes with time, the states are all modeled as random walk processes. The complex argument is however modeled as an integrator of the frequency offset as described before. The full continuous time model becomes

$$\dot{\theta}^r(t) = n_{\theta^r}(t), \tag{3.37}$$
$$\dot{a}^r(t) = n_{a^r}(t), \tag{3.38}$$
$$\dot{\phi}^r(t) = \delta_f(t) + n_{\phi^r}(t), \tag{3.39}$$
$$\dot{\delta}_f(t) = n_{\delta_f}(t), \tag{3.40}$$

where the index r denotes the r:th estimated ray. The states are subject to uncorrelated Gaussian noise processes $n(t)$. The noise term $n_{\phi^r}(t)$ is kept as a roughening noise term to avoid the situation of completely locking the individual phases to each other.

Discrete radio channel model

The differential equations in (3.37) to (3.40) are discretized with the sample rate T_s as

$$\begin{aligned}\begin{bmatrix}\theta^r_{k+1}\\ a^r_{k+1}\\ \phi^r_{k+1}\\ \delta_{f,k+1}\end{bmatrix} &= \begin{bmatrix}\mathbf{I}_R & \mathbf{0} & \mathbf{0} & \mathbf{0}\\ \mathbf{0} & \mathbf{I}_R & \mathbf{0} & \mathbf{0}\\ \mathbf{0} & \mathbf{0} & \mathbf{I}_R & T_s\mathbf{1}_R\\ \mathbf{0} & \mathbf{0} & \mathbf{0} & 1\end{bmatrix}\begin{bmatrix}\theta^r_k\\ a^r_k\\ \phi^r_k\\ \delta_{f,k}\end{bmatrix}\\ &+ \begin{bmatrix}T_s\mathbf{I}_R & \mathbf{0} & \mathbf{0} & \mathbf{0}\\ \mathbf{0} & T_s\mathbf{I}_R & \mathbf{0} & \mathbf{0}\\ \mathbf{0} & \mathbf{0} & T_s\mathbf{I}_R & \frac{T_s^2}{2}\mathbf{1}_R\\ \mathbf{0} & \mathbf{0} & \mathbf{0} & T_s\end{bmatrix}\begin{bmatrix}n_{\theta^r_k}\\ n_{a^r_k}\\ n_{\phi^r_k}\\ n_{\delta_{f,k}}\end{bmatrix}.\end{aligned} \tag{3.41}$$

Equations (3.29) to (3.33) together with the ones in (3.41), is the final dynamic state space representation of the kinematics and the radio channel model together. The measurement equation from (2.41) is sampled with sample rate T_s and becomes

$$y_k = \sum_{r=1}^{R} \alpha^r_k \exp\left(-i\langle p_k, \mathsf{e}(\theta^r_k)\rangle\right) + w_k, \tag{3.42}$$

where p_k is normalized with the constant $2\pi\frac{f_c}{c}$ to facilitate the notation, *i.e.*, distances are measured in the unit of wavelengths.

3.4 Observability of the states

Since all rays are assumed to impinge the receiver horizontally, neither the measurement equation (3.42) nor any other states depend on position along the z-axis, this state is unobservable in this model. The estimated position along the z-axis will therefore be the dead reckoning estimate. Looking at the yaw angle, *i.e.*, the rotation of the unit around the z-axis, it will also be unobservable. Consider a scenario where all impinging rays have been rotated φ radians anti-clockwise. If the position p is also rotated in the same direction, the new position $\acute{p}$ becomes

$$\acute{p} = \begin{bmatrix}\acute{p}_x\\ \acute{p}_y\end{bmatrix} = \begin{bmatrix}\cos(\varphi) & \sin(\varphi)\\ -\sin(\varphi) & \cos(\varphi)\end{bmatrix} p. \tag{3.43}$$

The scalar product in the argument of the measurement equation (3.42) is then changed to

$$\cos(\theta-\varphi)\acute{p}_x + \sin(\theta-\varphi)\acute{p}_y = \ldots = \cos(\theta)p_x + \sin(\theta)p_y. \tag{3.44}$$

Hence, the θ's and the positions can be rotated around the z-axis without affecting the measurement equation. This ambiguity can be removed using a magnetometer but this has for simplicity not been considered here. When evaluating the results of the sensor fusion algorithms, this ambiguity has to be taken into account.

4

Estimation Algorithms

In most cases, all states of a dynamic system can not be measured directly. Instead, the state vector has to be reconstructed in some way. If the system is not subject to any noise and the dynamic model of the states is completely known, the states would be easy to reconstruct by feeding the input signal for the true system to a model of the true system. However, if the input signals and measurements are subject to noise, the states can still be estimated but only to a certain accuracy.

The statistical viewpoint of state estimation can be summarized as follows. Given a noisy measurement y dependent on some states x, estimate the states from the measurement, given some prior knowledge of the state and measurement noise. The relation between these distributions is known as Bayes' formula

$$p(x|y) = \frac{p(y|x)p(x)}{p(y)}. \tag{4.1}$$

There are two ways of using measurements acquired for estimation. Either the measurements are lumped together and processed as a batch or they can be used on a sample by sample basis for recursive estimation. The two cases will be treated separately below.

4.1 Batch angle of arrival estimation

The virtual receiver array described in Section 2.2 can be used for angle of arrival estimation. If the positions p_k of the receiver are known and the θ unknown, it would be a classical AoA estimation problem using a virtual array where the samples from the array is processed as a batch. This problem is well studied in the literature and several different techniques have been developed: Capon's beamformer [Capon, 1969], MUSIC [Schmidt, 1986], and SAGE [Fessler and Hero, 1994] to mention some. In this thesis, the batch AoA estimation problem will be investigated using the ambiguity function described in, *e.g.*, [Gu, 1996] and a sparse convex optimization algorithm.

The ambiguity function

Arrange the complex amplitude α for each multipath component in a column vector $A \in \mathbb{C}^{R\times 1}$ as

$$A = \begin{bmatrix} \alpha^1 \\ \alpha^2 \\ \vdots \\ \alpha^R \end{bmatrix}. \tag{4.2}$$

The measurements from (3.42) can then be written in matrix form as

$$y = SA + W, \tag{4.3}$$

where the matrix $S = [s^1, s^2, \ldots, s^R] \in \mathbb{C}^{K\times R}$ is the steering matrix and whose columns are given by

$$s^r = \begin{bmatrix} 1 \\ \exp[-i(\langle p_1, \mathsf{e}(\theta^r)\rangle + \phi_1^r)] \\ \vdots \\ \exp[-i(\langle p_{K-1}, \mathsf{e}(\theta^r)\rangle + \phi_{K-1}^r)] \end{bmatrix}, \tag{4.4}$$

where $\mathsf{e}(\theta^r)$ is a unit vector pointing in the direction of the angle θ^r.

Assuming that $\delta_f(t) \equiv \delta_f$, the maximum likelihood estimates of the unknown amplitudes and parameters denoted by $\hat{A}$ and $\hat{\Theta}$, can be obtained by solving

$$\underset{A,\Theta}{\text{minimize}} \quad \|y - S(\Theta)A\|^2, \tag{4.5}$$

where $\Theta = [\theta^1, \theta^2, \ldots, \theta^R, \delta_f]^T$. To increase the readability, the Θ dependence in the S matrix is left out from here on. For a fixed Θ, the expression can be minimized over A as

$$\hat{A}(\Theta) = [S^H S]^{-1} S^H y, \tag{4.6}$$

where S^H denotes Hermitian transpose of S. Inserting this into (4.5) yields

$$\begin{aligned} \|y - S\hat{A}(\Theta)\|^2 &= y^H y - y^H S[S^H S]^{-1} S^H y \\ &\triangleq \|y\|^2 - C(\Theta), \end{aligned} \tag{4.7}$$

which is the difference between y and its projection onto the subspace of $S(\Theta)$. Maximizing $C(\Theta)$ will solve (4.5). If the noise is ignored, *i.e.*, assuming $y = S(\Theta^\star)A^\star$ where * indicates the true value of the variable, the function $C(\Theta)$ can be written as

$$C(\Theta) = A^{\star H} S^H(\Theta^\star) S[S^H S]^{-1} S^H S(\Theta^\star) A^\star. \tag{4.8}$$

The function $C(\Theta)$ is called the ambiguity function [Gu, 1996].

Figure 4.1 shows $C(\Theta)$ for a scenario where three rays impinge on a virtual array with $\delta_f \equiv 0$. As the number of elements K in the array grows, the angular resolution of the array gets finer. With 25 elements, the three impinging rays are clearly visible as three distinct peaks in the angular spectrum. However, the ambiguity function is not able to locate the AoA correctly even when the number of elements in the array grows. Therefore, more advance methods are needed.

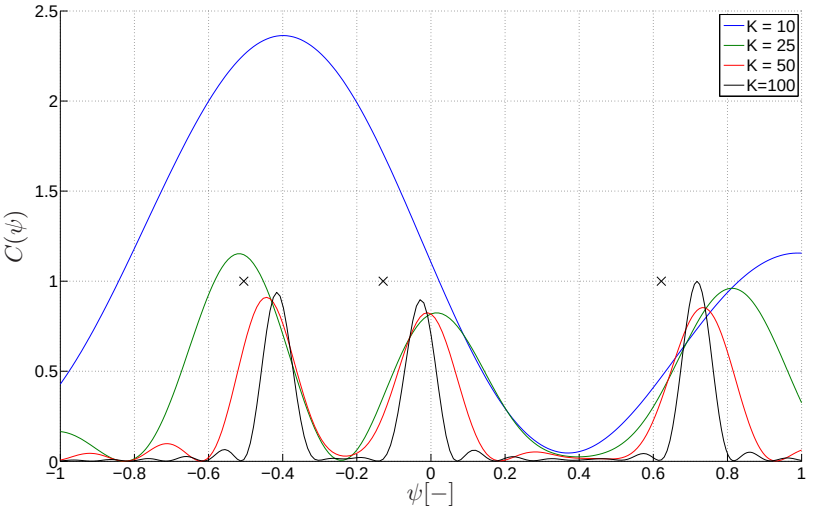

Figure 4.1 Ambiguity function for the scenario with three rays impinging on the array of length K from $[\theta^1, \theta^2, \theta^3] = [0.9, 1.7, 2.1]$ as a function of $\psi = \cos(\theta)$. The black crosses indicate the true locations of the rays. Note that the ambiguity function estimates the number of components correctly, but the location is wrong.

Convex angle of arrival estimation

The AoA estimation problem introduced in (4.5) is repeated here

$$\underset{\Theta, A}{\text{minimize}} \quad \|y - S(\Theta)A\|_2^2. \tag{4.9}$$

The vector $y = [y_0, \ldots, y_{K-1}]^T$ contains the K measurements from the virtual array and S is the steering matrix pointing towards the AoA of the impinging rays and A are the complex amplitudes. Now introduce a set $\Omega = [0, 2\pi]$ of possible angle of arrival directions and grid the set into M equidistant angles that cover Ω. Using this set, the matrix S will have M columns, where each column points to a possible AoA. The optimization

problem in (4.9) becomes a least squares problem in A and can be solved efficiently.

Reweighted ℓ_1 optimization The nature of the problem is that there will only be rays impinging on the array from a few angles. However, the least squares solution A_{ls} will not be sparse. To force the optimizer to find sparse solutions, ℓ_1-minimization and reweighted ℓ_1-minimization has been proposed in [Boyd and Vandenberghe, 2004] and [Candes et al., 2008]. One way of adding a cost of non-zero A elements is by solving the problem

$$\underset{A}{\text{minimize}} \quad \|y - SA\|_2^2 + \rho\|UA\|_1, \tag{4.10}$$

where $\rho > 0$ is a weight of the regularization term and $U = diag[\mu_1, \ldots, \mu_M]$ with positive weights μ_m. The weighting matrix U can be updated with an iterative algorithm, presented in [Candes et al., 2008] and restated here as Algorithm 1.

Algorithm 1 Iterative ℓ_1 minimization with adaptive reweighting

Initialize: $\mu_i^{(0)} = 1, \quad i = 1, \ldots, M$
for $l = 1, 2, \ldots, l^{\max}$ **do**
Solve the optimization problem in (4.10) with $U = \text{diag}(\mu^{(l)})$.
Update μ as

$$\mu_i^{(l+1)} = \frac{1}{|x_i^{(l)}| + \epsilon} \tag{4.11}$$

end for

The value $\epsilon > 0$ is suggested to be chosen smaller than the largest value expected in A. Thus, the reweighting scheme will put higher cost on small elements in A, forcing them to zero and thereby improving sparsity. Choosing ρ has been studied in literature, see [Ohlsson et al., 2010] and

$$\rho = c\|S^H y\|_\infty, \tag{4.12}$$

where $0 < c < 1$ is a constant, has proven to give a good weight between the two norm expressions in (4.10). Hence, the iterative ℓ_1 minimization has three parameters to adjust, $(\rho, \epsilon, l^{\max})$.

SPICE Another proposed algorithm for sparse parameter estimation in this problem is introduced in [Stoica and Babu, 2012] and is called SPICE. The algorithm starts with a weighted covariance criterion

$$\underset{P}{\text{minimize}} \quad \|R^{-1/2}(R - yy^H)\|^2 \tag{4.13}$$

where $R \triangleq BPB^H$ is the covariance matrix of the measurement vector y and the matrix $B \triangleq [S \quad \mathbf{I}_K] \in \mathbb{C}^{K\times(M+K)}$. P is diagonal with elements $[p_1, \ldots, p_{K+M}]$ where p_k is the variance of the power in each possible AoA and variance of the noise in each element k of the array. Calculations in [Stoica and Babu, 2012] show that the problem formulation in (4.13) can be rewritten as

$$\begin{aligned} \underset{p_k,\beta}{\text{minimize}} \quad & \beta^H P^{-1}\beta + \sum_{k=1}^{K+M} w_k^2 p_k \\ \text{subject to} \quad & B\beta = y, \end{aligned} \tag{4.14}$$

where the weights are defined as

$$w_k = \frac{\|b_k\|}{\|y\|} \tag{4.15}$$

and b_k are the columns of matrix B. Solving (4.14) with respect to p_k for a fixed β can be shown to lead to

$$p_k = \frac{|\beta_k|}{w_k}, \quad k = 1, \ldots, K+M. \tag{4.16}$$

The original problem in (4.14) can now be stated as a second order cone program (SOCP) as

$$\begin{aligned} \underset{\beta_k}{\text{minimize}} \quad & \sum_{k=1}^{K+M} w_k|\beta_k|, \\ \text{subject to} \quad & B\beta = y, \end{aligned} \tag{4.17}$$

which is the optimization problem that is the SPICE algorithm. The performance of the two algorithms presented here will be evaluated in Section 6.2.

4.2 Recursive state estimation

Instead of collecting a number of measurements and process in a batch, recursive state estimation can be used. Consider the discrete system

$$\begin{cases} x_{k+1} = f(x_k, u_k, n_k) \\ y_k \;\; = h(x_k, w_k), \end{cases} \tag{4.18}$$

where x_k is the state vector at time k, u_k is the control signal, n_k is the process noise and w_k is the measurement noise. There are many ways to formulate a state estimator for the system, depending on which criterion the estimator should satisfy. One criterion for a state estimator would be to minimize the mean square error of the estimates, *i.e.*,

$$\text{minimize} \quad \mathbb{E}[\|\tilde{x}_k\|^2], \tag{4.19}$$

where $\tilde{x}_k = \hat{x}_{k|k} - x_k$ and $\hat{x}_{k|k}$ is the estimated state vector at time k using measurements up to time k. If the system is linear and the noise processes are Gaussian, the Kalman filter is exactly this estimator [Kalman, 1960]. The Kalman filter can be written in an elegant way for recursive filtering; one step calculates the posterior distribution of the states using the measurements while the second step calculates a new prior distribution of the state using the system dynamics. If the state dynamics or the measurements are nonlinear, the equations can be linearized around the current state when calculating the covariance matrices. This filter is known as the extended Kalman filter (EKF), see [Maybeck, 1982], and the recursive equations of the EKF are summarized in Algorithm 2.

Algorithm 2 The Extended Kalman filter

Initialize: Initial state estimate: $\hat{x}_{1|0}$, and initial covariance $P_{1|0}$.
for $k = 1, 2, \ldots$ **do**
Calculate Kalman gain:

$$K_k = P_{k|k-1}H_k^T(H_k P_{k|k-1} H_k^T + R_k)^{-1} \tag{4.20}$$

Measurement update:

$$\hat{x}_{k|k} = \hat{x}_{k|k-1} + K_k[y_k - h(\hat{x}_{k|k-1}, 0)] \tag{4.21}$$
$$P_{k|k} = (I - K_k H_k)P_{k|k-1} \tag{4.22}$$

Time update:

$$\hat{x}_{k+1|k} = f(\hat{x}_{k|k}, u_k, 0) \tag{4.23}$$
$$P_{k+1|k} = F_k P_{k|k} F_k^T + G_k Q_k G_k^T \tag{4.24}$$

end for

Here $\hat{x}_{k|k}$ is the estimated state with a corresponding covariance matrix $P_{k|k} = \mathbb{E}[\tilde{x}_{k|k}\tilde{x}_{k|k}^T]$. The matrices F_k, G_k and H_k are the linearizations of the system in (4.18) as

$$F_k = \nabla_{x_k} f(\hat{x}_k, u_k, 0), \tag{4.25}$$
$$G_k = \nabla_{n_k} f(\hat{x}_k, u_k, 0), \tag{4.26}$$
$$H_k = \nabla_{x_k} h(\hat{x}_k, 0). \tag{4.27}$$

The matrices Q_k and R_k are the covariance matrices of the process and measurement noise respectively and assumed to be independent of each other.

Even if the Kalman filter can be modified to handle nonlinear dynamics there are other cases that the filter can not handle well, such as non-Gaussian

process or measurement noise or when the distributions can not be described well as Gaussian. It is obvious that the Kalman filter can not handle such cases since it represents the states as the mean value in a Gaussian distribution with a corresponding covariance matrix. For solving such estimation problems, other methods are needed such as the particle filter.

The particle filter

The underlying idea of the particle filter is to represent the filtering density using particles, each carrying a hypothesis of the state vector $\hat{x}_k$ and a weight w_k as a measure of the likelihood of that hypothesis when evaluated against the measurements. The particle filter was introduced in [Gordon et al., 1993] and has since then found many areas of application.

The dynamic and measurement equations of (4.18) can be written as drawings from conditional distributions as

$$x_{k+1} \sim p_x(x_{k+1}|x_k), \tag{4.28}$$

$$y_k \sim p_y(y_k|x_k). \tag{4.29}$$

Now consider the posterior distribution density

$$p(x_k|y_{1:k}) = p(x_k|y_k, y_{1:k-1}), \tag{4.30}$$

where $y_{1:k}$ denotes all measurements from time 1 to k. Using Bayes' rule (4.1) and the Markov property of dynamic systems, (4.30) can be transformed into

$$p(x_k|y_{1:k}) = \frac{p(y_k|x_k, y_{1:k-1})p(x_k|y_{1:k-1})}{p(y_k|y_{1:k-1})} = \frac{p(y_k|x_k)p(x_k|y_{1:k-1})}{p(y_k|y_{1:k-1})}, \tag{4.31}$$

where the denominator can, using marginalization, be written with known densities as

$$p(y_k|y_{1:k-1}) = \int p(y_k|x_k)p(x_k|y_{1:k-1})dx_k. \tag{4.32}$$

For the prediction step, the strategy with marginalization used above is used again

$$\begin{aligned} p(x_k|y_{1:k-1}) &= \int p(x_k, x_{k-1}|y_{1:k-1})dx_{k-1} \\ &= \int p(x_k|x_{k-1}, y_{1:k-1})p(x_{k-1}|y_{1:k-1})dx_{k-1} \\ &= \int p(x_k|x_{k-1})p(x_{k-1}|y_{1:k-1})dx_{k-1}. \end{aligned} \tag{4.33}$$

The integrals in (4.32) and (4.33) are usually not analytically solvable. If the distributions are Gaussian and the dynamic system is linear, the integrals

above are solvable and yield the Kalman filter equations presented in Algorithm 2. For the more general case, an approximation of the integrals can be used instead.

Introduce a particle as a sample from the posterior distribution

$$x_k^{(i)} \sim p(x_k|y_{1:k}), \quad i = 1, \ldots, N, \tag{4.34}$$

where N is the number of such particles. The particles can now be used to make an approximation of the posterior distribution as

$$p(x_k|y_{1:k}) \approx \hat{p}(x_k|y_{1:k}) = \sum_{i=1}^{N} w_{k|k}^{(i)} \delta(x_k - x_k^{(i)}) \tag{4.35}$$

with

$$\sum_{i=1}^{N} w_{k|k}^{(i)} = 1, \quad w_{k|k}^{(i)} \geq 0, \quad i = 1, \ldots, N. \tag{4.36}$$

By using the approximation above, the integrals in (4.31) and (4.33) can be solved approximately. Starting with the prediction step in (4.33) and replacing the posterior distribution with its approximation from (4.35) yields

$$\begin{aligned} p(x_k|y_{1:k-1}) &= \int p(x_k|x_{k-1}) p(x_{k-1}|y_{1:k-1}) dx_{k-1} \\ &\approx \int p(x_k|x_{k-1}) \sum_{i=1}^{N} w_{k-1|k-1}^{(i)} \delta(x_{k-1} - x_{k-1}^{(i)}) dx_{k-1} \\ &= \sum_{i=1}^{N} w_{k-1|k-1}^{(i)} p(x_k|x_{k-1}^{(i)}). \end{aligned} \tag{4.37}$$

To regain a set of particles instead of a distribution, N new particles should be drawn from (4.37). However, it is difficult to directly generate samples from this distribution. Instead, importance sampling can be used to generate the samples [Gordon et al., 1993]. From importance sampling it is given that the importance weights w are calculated as

$$w = \frac{p(x_k|y_{1:k-1})}{q(x_k|x_{k-1}, y_k)} \tag{4.38}$$

where the numerator is the target distribution and the denominator is the proposal distribution from which samples can be drawn. The first step of importance sampling is to draw new particles from the proposal distribution as

$$\tilde{x}_k^{(i)} \sim q(x_k|x_{k-1}^{(i)}, y_k), \quad i = 1, \ldots, N. \tag{4.39}$$

The weights w for the new samples are computed as

$$w_{k|k-1}^{(i)} = \frac{p(\tilde{x}_k^{(i)}|y_{1:k-1})}{q(\tilde{x}_k^{(i)}|x_{k-1}^{(i)}, y_k)}, \quad i = 1, \ldots, N. \tag{4.40}$$

By choosing

$$q(x_k|x_{k-1}, y_k) \triangleq p(x_k|x_{k-1}) \tag{4.41}$$

as proposal distribution, which is the state dynamics from (4.28), the following relation is obtained

$$\begin{aligned} w_{k|k-1}^{(i)} &= \frac{p(\tilde{x}_k^{(i)}|y_{1:k-1})}{p(\tilde{x}_k^{(i)}|x_{k-1}^{(i)})} \\ &\approx \frac{\int p(\tilde{x}_k^{(i)}|x_{k-1}) \sum_{i=1}^{N} w_{k-1|k-1}^{(i)} \delta(x_{k-1} - x_{k-1}^{(i)}) dx_{k-1}}{p(\tilde{x}_k^{(i)}|x_{k-1}^{(i)})} \\ &= w_{k-1|k-1}^{(i)}. \end{aligned} \tag{4.42}$$

The approximation of the prediction step is then

$$\hat{p}(x_k|y_{1:k-1}) = \sum_{i=1}^{N} w_{k|k-1}^{(i)} \delta(x_k - \tilde{x}_k^{(i)}). \tag{4.43}$$

To solve the measurement update in (4.31), start with (4.32) and use the previous result to get an approximation as

$$\begin{aligned} \hat{p}(y_k|y_{1:k-1}) &= \int p(y_k|x_k) \sum_{i=1}^{N} w_{k|k-1}^{(i)} \delta(x_k - \tilde{x}_k^{(i)}) dx_k \\ &= \sum_{i=1}^{N} w_{k|k-1}^{(i)} p(y_k|\tilde{x}_k^{(i)}). \end{aligned} \tag{4.44}$$

Substituting this into (4.31) yields the following approximation

$$\begin{aligned} \hat{p}(x_k|y_{1:k}) &= \frac{p(y_k|x_k)\hat{p}(x_k|y_{1:k-1})}{\hat{p}(y_k|y_{1:k-1})} \\ &= \sum_{i=1}^{N} \frac{w_{k|k-1}^{(i)} p(y_k|x_k)}{\sum_{j=1}^{N} w_{k|k-1}^{(j)} p(y_k|\tilde{x}_k^{(j)})} \delta(x_k - \tilde{x}_k^{(i)}) \\ &\approx \sum_{i=1}^{N} w_{k|k-1}^{(i)} \delta(x_k - \tilde{x}_k^{(i)}). \end{aligned} \tag{4.45}$$

Resampling A problem associated with running the above filter for many subsequent time steps would be depletion which implies that only some of the particles are located in the dense part of the target distribution p. To overcome this problem, the particles are resampled. The resampling is carried out using draw and replace so that particles having a high weight w are more likely to be reproduced several times compared to particles with low weights. The resampling step has some theoretical implications for the filter but it has proven to be a good solution for the depletion problem, see [Gordon et al., 1993] and [Gustafsson, 2010]. Resampling can be performed in every time step but in order to save time, in this thesis resampling is done when the effective number of particles, calculated as

$$N_{\text{eff}} = \frac{1}{\sum_{i=1}^{N} \left(w_{k|k}^{(i)} \right)^2}, \tag{4.46}$$

drops below a predetermined level N_T. After resampling has been performed, the weights are reinitialized as $w_{k|k}^{(i)} = 1/N, \quad i = 1, \ldots, N$.

Algorithm 3 The Particle Filter

Initialize filter: Generate $x_{1|0}^{(i)} \sim p(x_{1|0})$ and set $w_{1|0}^{(i)} = 1/N, \quad i = 1, \ldots, N$.

for $k = 1, 2, \ldots$ **do**

Measurement update: Evaluate importance weights as

$$w_{k+1|k}^{(i)} = \frac{p(y_k|x_k^{(i)})}{\sum_{j=1}^{N} p(y_k|x_k^{(j)}) w_{k|k-1}^{(j)}} w_{k|k-1}^{(i)}. \tag{4.47}$$

if $N_{\text{eff}} < N_T$ **then**

Resample N particles using draw and replace with weights $w_{k+1|k}^{(i)}$.

Reinitialize weights to $w_{k+1|k}^{(i)} = 1/N, i = 1, \ldots, N$.

end if

Time update: Draw new particles from proposal distribution as

$$x_{k+1}^{(i)} \sim p(x_{k+1}|x_k^{(i)}), \quad i = 1, \ldots, N. \tag{4.48}$$

end for

The marginalized particle filter

By representing the filtering density with particles instead of using mean and covariance, as in the Kalman filter, distributions are not limited to Gaussians

anymore. While the Kalman filter has all the information about the distributions in the mean and covariance, the set of particles represents the distributions. To obtain a good description of the filtering densities, the particles must be able to cover the true distribution. More particles are needed as the state dimension grows and the computing power and time needed for solving the problem increases dramatically, [Karlsson et al., 2005].

One solution to reduce the computational burden of the particle filter is to use marginalization of the linear states. The linear states can then be estimated using a standard Kalman filter while the nonlinear states are still estimated with the particle filter. Hence, every particle now carries a state vector with the nonlinear states, and a state vector with the linear states, and a corresponding covariance matrix. This filter is called the marginalized particle filter or Rao-Blackwellized particle filter and was introduced in [Doucet et al., 2000]. The derivations of the marginalized particle filter are long and have been left out but can be found in [Schön et al., 2005]. The filter is however summarized here for convenience.

Let x_k^l denote the linear state vector and x_k^n the nonlinear state vector. The system in (4.18) is rewritten as

$$\begin{aligned} x_{k+1}^n &= f_k^n(x_k^n) + A_k^n(x_k^n)x_k^l + G_k^n(x_k^n)n_k^n, \\ x_{k+1}^l &= f_k^l(x_k^n) + A_k^l(x_k^n)x_k^l + G_k^l(x_k^n)n_k^l, \\ y_k &= h_k(x_k^n) + C_k(x_k^n)x_k^l + w_k. \end{aligned} \tag{4.49}$$

The filtering algorithm for the decoupled case, *i.e.*,

$$n_k = \begin{bmatrix} n_k^n \\ n_k^l \end{bmatrix} \sim \mathcal{N}(\mathbf{0}, Q_k), \quad Q_k = \begin{bmatrix} Q_k^n & 0 \\ 0 & Q_k^l \end{bmatrix}, \tag{4.50}$$

is summarized in Algorithm 4.

The distributions in (4.51) and (4.57) are given by

$$p(y_k|x_{1:k}^{n,(i)}, y_{1:k-1}) = \mathcal{N}(h_k(x_k^{n,(i)}) + C_k(x_k^{n,(i)})\hat{x}_{k|k-1}^{l,(i)}, S_k^{(i)}) \tag{4.62}$$

and

$$p(x_{k+1|k}^{n,(i)}|x_{1:k}^{n,i}, y_{1:k}) = \mathcal{N}(f_k^n(x_k^{n,(i)}) + A_k^n(x_k^{n,(i)})\hat{x}_{k|k}^{l,(i)}, M_k^{(i)}) \tag{4.63}$$

respectively.

The approximation of the final state distributions become

$$\begin{aligned} \hat{p}(x_k^n|y_{1:k}) &\approx \sum_{i=1}^{N} w_{k|k-1}^{(i)} \delta(x_k - \tilde{x}_k^{(i)}), \\ \hat{p}(x_k^l|y_{1:k}) &\approx \sum_{i=1}^{N} w_{k|k-1}^{(i)} \mathcal{N}(x_k^l|x_{k|k}^{l,(i)}, P_{k|k}^{(i)}). \end{aligned} \tag{4.64}$$

Algorithm 4 The Marginalized Particle Filter

Initialize filter: For $i = 1, \ldots, N$, generate $x_{1|0}^{n,(i)} \sim p(x_{1|0}^n)$, $x_{1|0}^{l,(i)} = x_0^l$, $P_{1|0}^{(i)} = P_0$, and set $w_{1|0}^{(i)} = 1/N$.

for $k = 1, 2, \ldots$ **do**

Measurement update: Evaluate importance weights as

$$\tilde{w}_{k+1|k}^{(i)} = p(y_k | x_{1:k}^{n,(i)}, y_{1:k-1}) w_{k|k-1}^{(i)} \tag{4.51}$$

and normalize

$$w_{k+1|k}^{(i)} = \frac{\tilde{w}_{k+1|k}^{(i)}}{\sum_{j=1}^{N} \tilde{w}_{k+1|k}^{(j)}} \tag{4.52}$$

if $N_{\text{eff}} < N_T$ **then**

Resample N particles using draw and replace with weights $w_{k+1|k}^{(i)}$.

Reinitialize weights to $w_{k+1|k}^{(i)} = 1/N, \quad i = 1, \ldots, N$.

end if

Measurement update of the Kalman filter:

$$\hat{x}_{k|k}^{l,(i)} = \hat{x}_{k|k-1}^{l,(i)} + K_k^{(i)}[y_k - h_k - C_k \hat{x}_{k|k-1}^{l,(i)}] \tag{4.53}$$

$$P_{k|k}^{(i)} = P_{k|k-1}^{(i)} - K_k^{(i)} S_k^{(i)} (K_k^{(i)})^T \tag{4.54}$$

$$S_k^{(i)} = C_k P_{k|k-1}^{(i)} C_k^T + R_k \tag{4.55}$$

$$K_k^{(i)} = P_{k|k-1}^{(i)} C_k^T (S_k^{(i)})^{-1} \tag{4.56}$$

Draw new particles from the proposal distribution

$$x_{k+1|k}^{n,(i)} \sim p(x_{k+1|k}^{n,(i)} | x_{1:k}^{n,(i)}, y_{1:k}), \quad i = 1, \ldots N. \tag{4.57}$$

Time update of the Kalman filter:

$$\hat{x}_{k+1|k}^{l,(i)} = A_k^l \hat{x}_{k|k}^l + f_k^l + L_k(x_{k+1}^{n,(i)} - f_k^n - A_k^n \hat{x}_{k|k}^{l,(i)}) \tag{4.58}$$

$$P_{k+1|k}^{(i)} = A_k^l P_{k|k}^{(i)} (A_k^l)^T + G_k^l Q_k^l (G_k^l)^T - L_k^{(i)} M_k^{(i)} (L_k^{(i)})^T \tag{4.59}$$

$$M_k^{(i)} = A_k^n P_{k|k}^{(i)} (A_k^n)^T + G_k^n Q_t^n (G_k^n)^T \tag{4.60}$$

$$L_k^{(i)} = A_k^l P_{k|k}^{(i)} (A_k^n)^T (M_k^{(i)})^{-1} \tag{4.61}$$

end for

4.3 Estimation performance bounds

For all estimation problems, it is of interest to know how well a parameter can be estimated with given measurements and noise levels. The Cramér-Rao bound (CRB) provides such a lower bound on the error covariance for any unbiased estimator. Assume that y is a measurement and $\hat{x}$ is the output of an unbiased linear estimator of the parameter x. Then

$$\mathsf{Cov}[\tilde{x}] \geq P^{CRB} = \mathcal{I}^{-1}, \tag{4.65}$$

where, $\tilde{x}$ is the estimation error, P^{CRB} the Cramér-Rao bound, and $\mathcal{I}$ the Fisher information matrix. Assume one observation $y_k \in \mathbb{R}^n$ from a system

$$y_k = h(x_k) + w_k, \tag{4.66}$$

where $h(x_k)$ is the measurement equation for the system with x_k as its state vector and w_k is a noise process. For K such independent observations $[y_0, \ldots, y_{K-1}]$, the Fisher information matrix is given by

$$\mathcal{I} = -\mathbb{E}\left\{ \sum_{k=1}^{K} \frac{\partial^2 \log(p(y_k|x_k))}{\partial x_k \partial x_k^T} \right\}, \tag{4.67}$$

where p is the likelihood function for the noise process w_k in (4.66). Assume that w_k is a white Gaussian noise process, *i.e.*,

$$y_k \sim \mathcal{N}(h(x_k), \Sigma). \tag{4.68}$$

In such case, the Fisher information matrix becomes

$$\mathcal{I} = \sum_{k=1}^{K} H^H(x_k) \Sigma^{-1} H(x_k), \tag{4.69}$$

where

$$H(x_k) = \frac{\partial h}{\partial x}(x_k) =: \nabla_{x_k} h(x_k). \tag{4.70}$$

Similarly, if the measurements $y_k \in \mathbb{C}$ are subject to circular complex Gaussian noise as

$$y_k \sim \mathcal{CN}(h(x_k), \Sigma), \tag{4.71}$$

where $h(x_k) \in \mathbb{C}$ and $x_k \in \mathbb{R}$, the Fisher information matrix is given by [Kay, 1993]

$$\mathcal{I} = 2\Re\left\{ \sum_{k=1}^{K} H^H(x_k) \Sigma^{-1} H(x_k) \right\}. \tag{4.72}$$

Note that the Fisher information matrix is additive, *i.e.*, if two independent measurements series with Fisher information matrices of $\mathcal{I}_1$ and $\mathcal{I}_2$ respectively are joined, the total information is the sum $\mathcal{I}_1 + \mathcal{I}_2$. Also note that the CRB is an asymptotic bound with respect to the number of measurements, and not necessarily reachable but a nonlinear estimator might also be able to perform better than the bound.

Recursive Cramér-Rao bounds

A recursively updated Cramér-Rao bound is presented in [Taylor, 1979]. For a nonlinear system with deterministic inputs and white Gaussian noise, the recursively updated $P_{k|k}^{CRB}$ propagates with the equations (4.22) and (4.24), found in the EKF in Algorithm 2. The linearized matrices needed are calculated using the true state vector $x_k^\star$ as

$$F_k = \nabla_{x_k} f(x_k^\star, u_k, 0), \tag{4.73}$$

$$G_k = \nabla_{n_k} f(x_k^\star, u_k, 0), \tag{4.74}$$

$$H_k = \nabla_{x_k} h(x_k^\star, 0). \tag{4.75}$$

This means that the EKF produces the CRB as a side result if the true state vector is supplied to the filter.

5

Implementation Aspects and Requirements

5.1 The marginalized particle filter

The length of the state vector (3.36) would force the required number of particles in the original particle filter to be too large for efficiently solving the state estimation problem. For this reason, the marginalized particle filter in Algorithm 4 from Section 4.2 will be used for recursively estimating the state vector.

Linearized/nonlinear states

The state vector (3.36) of the state space model in Chapter 3 can be divided into linear and nonlinear states according to the model in (4.49). The goal is to keep as many states as possible in the linear part of the filter in order to keep the number of particles low. Due to the nonlinearities in the measurement equation (3.42), position p, angle of arrival θ, and the argument of the complex amplitude ϕ are clearly part of the nonlinear domain. The nonlinear state vector becomes

$$x^n = [p, \theta^1, \ldots, \theta^R, \phi^1, \ldots, \phi^R]^T \in \mathbb{R}^{3+2R}. \tag{5.1}$$

The quaternion states q have nonlinear state dynamics but the EKF has successfully been used in, *e.g.*, [Sabatini, 2006] to estimate the quaternion after the dynamics has been linearized. The success of the linearization will depend on the level of the angular velocity. For the angular velocities used in the experiments, the linearization has found to be a good approximation and the quaternion is arranged with the rest of the linear states as

$$x^l = [v, \delta_a, q, \delta_\omega, a^1, \ldots, a^R, \delta_f]^T \in \mathbb{R}^{14+R}. \tag{5.2}$$

For the marginalized particle filter (4.49), the matrices A_k^n, A_k^l, G_k^n, and G_k^l together with the two state vectors given in (5.1) and (5.2) become

$$A_k^l = \begin{bmatrix} \mathbf{I}_3 & T_s R(q_k) & T_s Q'(q_k, u_{a,k} + \delta_{a,k}) & \mathbf{0} & \mathbf{0} & \mathbf{0} \\ \mathbf{0} & \mathbf{I}_3 & \mathbf{0} & \mathbf{0} & \mathbf{0} & \mathbf{0} \\ \mathbf{0} & \mathbf{0} & \mathbf{I}_4 + \frac{T_s}{2} Q(u_{\omega,k}) & \frac{T_s}{2} P(q_k) & \mathbf{0} & \mathbf{0} \\ \mathbf{0} & \mathbf{0} & \mathbf{0} & \mathbf{I}_3 & \mathbf{0} & \mathbf{0} \\ \mathbf{0} & \mathbf{0} & \mathbf{0} & \mathbf{0} & \mathbf{I}_R & \mathbf{0} \\ \mathbf{0} & \mathbf{0} & \mathbf{0} & \mathbf{0} & \mathbf{0} & 1 \end{bmatrix} \tag{5.3}$$

$$G_k^l = \begin{bmatrix} T_s \mathbf{I}_3 & \mathbf{0} & \mathbf{0} & \mathbf{0} & \mathbf{0} & \mathbf{0} \\ \mathbf{0} & T_s \mathbf{I}_3 & & \mathbf{0} & \mathbf{0} & \mathbf{0} \\ \mathbf{0} & \mathbf{0} & \frac{T_s}{2} P(q_k) & \mathbf{0} & \mathbf{0} & \mathbf{0} \\ \mathbf{0} & \mathbf{0} & \mathbf{0} & T_s \mathbf{I}_3 & \mathbf{0} & \mathbf{0} \\ \mathbf{0} & \mathbf{0} & \mathbf{0} & \mathbf{0} & T_s \mathbf{I}_R & \mathbf{0} \\ \mathbf{0} & \mathbf{0} & \mathbf{0} & \mathbf{0} & \mathbf{0} & T_s \end{bmatrix} \tag{5.4}$$

$$A_k^n = \begin{bmatrix} T_s \mathbf{I}_3 & \frac{T_s^2}{2} \mathbf{I}_3 & \frac{T_s^2}{2} Q'(q_k, u_{a,k} + \delta_{a,k}) & \mathbf{0} & \mathbf{0} & \mathbf{0} \\ \mathbf{0} & \mathbf{0} & \mathbf{0} & \mathbf{0} & \mathbf{0} & \mathbf{0} \\ \mathbf{0} & \mathbf{0} & \mathbf{0} & \mathbf{0} & \mathbf{0} & T_s \mathbf{1}_R \end{bmatrix} \tag{5.5}$$

$$G_k^n = \begin{bmatrix} \frac{T_s^2}{2} \mathbf{I}_3 & \mathbf{0} & \mathbf{0} & \mathbf{0} \\ \mathbf{0} & T_s \mathbf{I}_R & \mathbf{0} & \mathbf{0} \\ \mathbf{0} & \mathbf{0} & T_s \mathbf{I}_R & \frac{T_s^2}{2} \mathbf{1}_R \end{bmatrix}, \tag{5.6}$$

where the matrix $Q'(q, p)$ is defined as

$$\begin{aligned} Q'(q,p) &= \nabla_q R(q) p \\ &= 2 \begin{bmatrix} p_x q_0 - p_y q_3 + p_z q_2 & p_x q_3 + p_y q_0 - p_z q_1 & p_y q_1 - p_x q_2 + p_z q_0 \\ p_x q_1 + p_y q_2 + p_z q_3 & p_x q_2 - p_y q_1 - p_z q_0 & p_x q_3 + p_y q_0 - p_z q_1 \\ p_y q_1 - p_x q_2 + p_z q_0 & p_x q_1 + p_y q_2 + p_z q_3 & p_y q_3 - p_x q_0 - p_z q_2 \\ p_z q_1 - p_y q_0 - p_x q_3 & p_x q_0 - p_y q_3 + p_z q_2 & p_x q_1 + p_y q_2 + p_z q_3 \end{bmatrix}^T, \end{aligned} \tag{5.7}$$

where $q = [q_0, q_1, q_2, q_3]^T$ and $p = [p_x, p_y, p_z]^T$.

Quaternion normalization

As mentioned in Section 3.2, the discretized dynamic equation and noise properties of the quaternion breaks the unit length constraint in (3.11). This is fixed by normalizing the quaternion every time step k as

$$q_k := \frac{q_k}{\|q_k\|}, \tag{5.8}$$

which is common practice, see [Sabatini, 2006].

Filter initialization

Since the state estimation problem is nonlinear, there might be several local minima to where the estimation algorithm can converge. To avoid this, good state initialization is important. For the particle filter there is another aspect. If the filter is to cover a larger set of possibilities in the beginning, the number of particles must be increased to still obtain a good coverage over the distribution. By using the convex AoA estimation algorithms, an initial guess of the AoA and the number of rays present can be obtained and thereby also reducing the number of particles. Note that the batch approaches to AoA estimation assumes that the steering matrix is known, *i.e.*, the positions need to be estimated. Since dead reckoning works fine for short time periods, this is a viable approach. Figure 1.2 indicates that dead reckoning using a consumer grade IMU are feasible with error $\ll 1$ wavelength for a couple of seconds at wavelengths of approximately 0.1 m.

Amplitude limitation

Due to the modeling of the amplitude $a(t)$ of the rays as a random walk process, there is a possibility that the amplitude gets very close to zero or even negative. Since the amplitude $a(t)$ is a positive number by its definition, see (3.34), the random walk process has to be limited. A crude solution to this problem is to assign zero weight to all particles that have an amplitude below a certain threshold after the particles are evaluated with the measurement equation (4.51). Thus, the particles having zero weight will be removed the next time resampling is executed.

5.2 Choice of sample rate

The sample rate of the system must be chosen high enough in order for it to capture the movement of the device properly. On the other hand, a sample rate that is too high will only produce a lot of extra data that will not add any extra information to the estimation algorithms. In the simple case with one impinging ray on the receiver, the argument of the radio signal revolves 2π every λ moved in the direction of the impinging ray, see Section 2.1. The Nyquist sampling theorem states that the sample rate has to be at least twice the frequency of the sampled signal. To get some margin to the lower bound, 5 samples per λ is assumed to be enough. In the case of receiving rays at 1800 MHz and sample rate of 50 Hz, the maximum speed for the device becomes $\approx$1.5 m/s which is considered to be sufficient for movements performed in this thesis.

5.3 Synchronization requirements

The IMU and the radio signal are supposed to be sampled with the same rate at the same time. If the two systems are not sampled simultaneously, there will be some jitter altering the sample time. Assume that the IMU is sampled at kT_s while the sample from the radio receiver is taken at $kT_s + \Delta t$ where Δt has zero mean and variance $\mathbb{E}[\Delta t]^2$. If the velocity of the unit is assumed to be constant, $v(t) \triangleq [v_x, v_y]^T$ between kT_s and $kT_s + \Delta t$, and the position of the unit is p_k at time kT_s, the position at time $kT_s + \Delta t$ will be $p_k + \Delta t v$. The baseband signal for the two cases will be

$$y(kT_s) = \sum_{r=1}^{R} \alpha_k^r \exp[-i\langle \mathsf{e}(\theta_k^r), p_k \rangle] + w_k \tag{5.9}$$

$$y(kT_s + \Delta t) = \sum_{r=1}^{R} \alpha_k^r \exp[-i\langle \mathsf{e}(\theta_k^r), p_k + \Delta t v \rangle] + w_k, \tag{5.10}$$

i.e., (5.9) is the baseband signal when the IMU was sampled while (5.10) is the signal that was sampled. The difference Δy_k between them can be approximated as

$$\begin{aligned} \Delta y_k &\approx \sum_{r=1}^{R} \alpha_k^r (-i\langle \mathsf{e}(\theta_k^r), p_k + \Delta t v \rangle + i\langle \mathsf{e}(\theta_k^r), p_k \rangle) \\ &= -i\Delta t \sum_{r=1}^{R} \alpha_k^r \langle \mathsf{e}(\theta_k^r), v \rangle \end{aligned} \tag{5.11}$$

Let $\bar{v}$ denote the largest value of $v(t)$ and the variance of Δy_k can be bounded as

$$\mathbb{E}[\Delta y_k]^2 = \mathbb{E}[\Delta t]^2 \left| \sum_{r=1}^{R} \alpha_k^r \langle \mathsf{e}(\theta_k^r), v \rangle \right|^2 \leq \mathbb{E}[\Delta t]^2 \left| \sum_{r=1}^{R} \bar{v} \alpha_k^r \right|^2. \tag{5.12}$$

Introduce $\bar{a_k}$ as the strongest component of the R impinging rays and rewrite the sum as

$$\mathbb{E}[\Delta y_k]^2 \leq \mathbb{E}[\Delta t]^2 \bar{v}^2 \bar{a_k}^2 R^2. \tag{5.13}$$

If the variance of the difference is smaller than the noise on the measurement signal, the jitter will be covered in noise. If the noise of the measurement signal is given as SNR with respect to the strongest component, the standard deviation should satisfy

$$\mathrm{RMSE}(\Delta t) \leq \frac{\sigma_y}{R\bar{v}} \tag{5.14}$$

where σ_y is the standard deviation of the measurement signal. Let $\bar{v} = 5\ \lambda/\mathrm{s}$ and two rays impinge on the array. The noise from the jitter will be equal to the measurement noise if $\mathrm{RMSE}(\Delta t) \approx 1$ ms and the SNR is 20 dB.

6

Simulation Results and Analysis

In this chapter, simulation results are presented and analyzed. Experimental results are given in the subsequent chapter.

6.1 Ambiguity for linear movements

The ability and accuracy of angle of arrival (AoA) estimation will be dependent on the movement of the receiver. As seen in (3.42), a constant frequency error will alter the phase of the received signal in the same manner as a constant velocity movement of the receiver will. Even if the position of the receiver is known with high accuracy, the frequency error will lead to an estimation error in the AoA.

Consider a virtual antenna array, formed by moving the receiver along the x-axis with known constant velocity v_x. Let the known position of the receiver at time instance k be

$$p_{x,k} = \quad v_x k, \quad \forall k \in \{-K, \ldots, K\}. \tag{6.1}$$

Assume that the receiver has a constant unknown frequency error $\delta_f(t) \equiv \delta_f$ and that the radio channel is static throughout the movement of the receiver. If one ray impinges on the array from angle θ, the received signal from the array is according to (3.42)

$$y_k = \alpha \exp\left(-i(\psi v_x + \delta_f)k\right) + w_k, \tag{6.2}$$

where $\psi = \cos(\theta)$ and $w_k \sim \mathcal{CN}(0, \sigma^2)$. Note that the phase error at the starting point can be non-zero but this can be included in the complex amplitude α does not affect the calculations below.

The ambiguity function (4.7) with $\Theta = [\psi, \delta_f]$ becomes

$$\begin{aligned} C(\Theta) &= \frac{\alpha^2}{2K+1} \left| \sum_{k=-K}^{K} \exp\left(-i(-v_x\psi + v_x\psi^\star - \delta_f + \delta_f^\star)k\right) \right|^2 \\ &= \frac{\alpha^2}{2K+1} \left(1 + 2\sum_{k=1}^{K} \cos(\Delta_1 k) \right)^2, \end{aligned} \tag{6.3}$$

where $\Delta_1 = -v_x\psi + v_x\psi^\star - \delta_f + \delta_f^\star$.

Figure 6.1 shows the level curves of the ambiguity function as a function of δ_f and ψ when K = 10, $v_x = 0.2\pi$, $\delta_f^\star = \frac{1}{25}\pi$ and $\psi^\star = 0.5$. Obviously, there are infinitely many combinations of ψ and δ_f that have the same ambiguity value. Hence, if the receiver is moved in one direction along the x-axis, there is no possibility to distinguish a frequency error in the receiver from an offset in the estimated AoA.

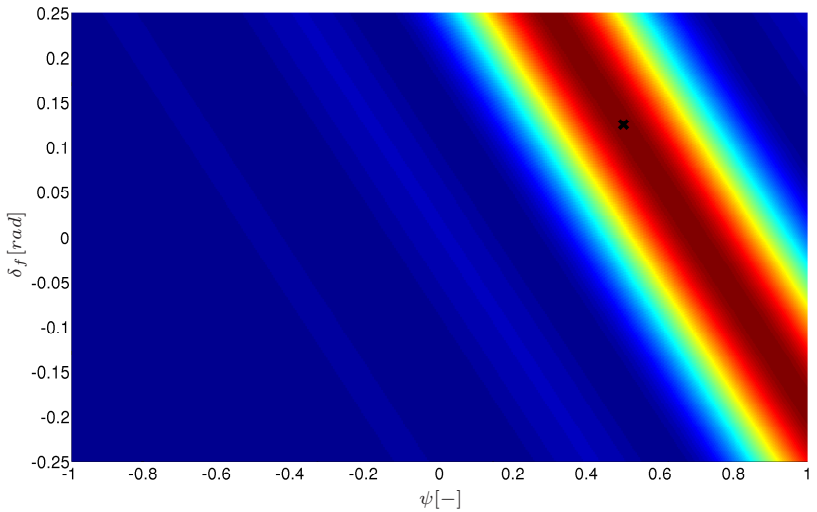

Figure 6.1 The ambiguity function as a level curve of δ_f and ψ for movement with constant known velocity in one direction. There is no possibility to distinguish a frequency error in the receiver from an offset in the estimated AoA.

The Fisher information matrix with respect to the unknown parameters $\Psi = [\alpha, \psi, \delta_f]^T$ of the impinging ray is calculated according to (4.69) as

$$\begin{aligned} H &= \nabla_\Psi [\alpha \exp\left(-i(\psi v_x + \delta_f)k\right)] \\ &= \exp\left(-i(\psi v_x + \delta_f)k\right) \begin{bmatrix} 1 & -i\alpha v_x k & -i\alpha k \end{bmatrix} \end{aligned} \tag{6.4}$$

$$\mathcal{I}_\Psi = \frac{2}{\sigma^2}\begin{bmatrix} 2K+1 & 0 & 0 \\ 0 & 2a^2v_x^2\sum_{k=1}^{K}k^2 & 2a^2v_x\sum_{k=1}^{K}k^2 \\ 0 & 2a^2v_x\sum_{k=1}^{K}k^2 & 2a^2\sum_{k=1}^{K}k^2 \end{bmatrix}, \tag{6.5}$$

where σ is the standard deviation of the noise in (6.2). The Fisher information matrix reveals that the estimation of amplitude is independent of θ and δ_f. Also, the two last columns are linearly dependent which is seen in Figure 6.1 in that no information is obtained in one direction no matter how many samples are collected.

Now assume a scenario where the receiver is moved back and forth along the x-axis with the same starting and end position, *i.e.*, the position at time instance k is given by

$$p_{x,k} = \begin{cases} v_x(K+k) & \forall k \in \{-2K,\ldots,0\} \\ v_x(K-k) & \forall k \in \{0,\ldots,2K\} \end{cases} \tag{6.6}$$

where v_x is the speed per sample. Note that the array has twice the length compared to the previous case. The ambiguity function becomes

$$C(\Theta) = \frac{\alpha^2}{4K+2}\left|\sum_{k=-2K}^{0}\exp\left(-i\Delta_1 k\right) + \sum_{k=0}^{2K}\exp\left(-i\Delta_2 k\right)\right|^2 \tag{6.7}$$

$$= \left|\frac{1-\exp\left(i\Delta_1(2K+1)\right)}{1-\exp\left(i\Delta_1\right)} + \frac{1-\exp\left(-i\Delta_2(2K+1)\right)}{1-\exp\left(-i\Delta_2\right)}\right|^2 \tag{6.8}$$

with Δ_1 as before and $\Delta_2 = v_x\psi - v_x\psi^\star - \delta_f + \delta_f^\star$. The ambiguity function for this scenario with the same choice of ψ and δ_f as before is shown in Figure 6.2. The ambiguity function does now have a distinct peak at the correct values $\psi^\star$ and $\delta_f^\star$. Hence, the ambiguity between frequency error and AoA estimation offset is removed due to the richer movement. There is no fundamental limitation to estimate AoA and frequency error jointly if the movement of the receiver is rich enough and known.

Similarly, as in the previous case, the Fisher information matrix with respect to Ψ becomes

$$\mathcal{I}_\Psi = \frac{2}{\sigma^2}\begin{bmatrix} 4K+2 & 0 & 0 \\ 0 & 2a^2v_x^2\sum_{k=1}^{2K}k^2 & 0 \\ 0 & 0 & 2a^2\sum_{k=1}^{2K}k^2 \end{bmatrix}. \tag{6.9}$$

Comparing this with (6.5) reveals that the linearly dependent columns are removed due to the movement. The result is instead a diagonal Fisher information matrix which is seen in Figure 6.2 where the ellipse formed by the ambiguity function is parallel to the axes.

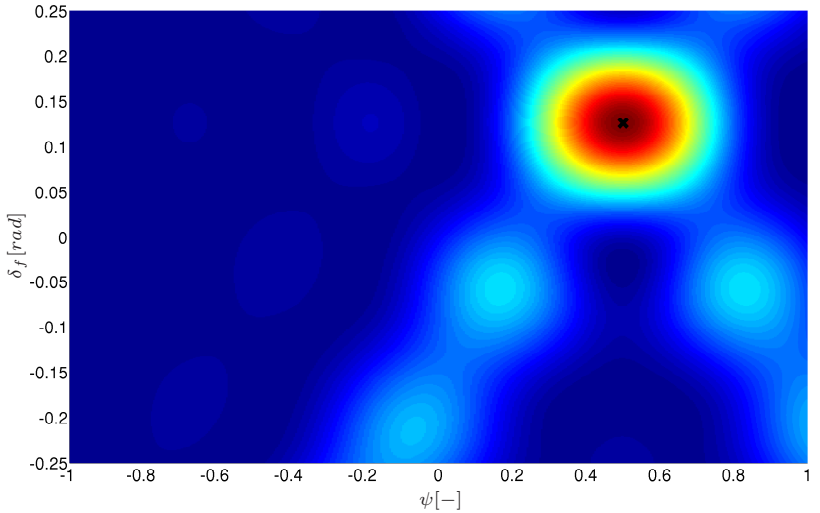

Figure 6.2 The ambiguity function as a level curve of δ_f and ψ for linear movement in two directions. The ambiguity between AoA and a frequency error is removed due to the richer movement.

Ambiguity for circular movements

The movement of the receiver is now assumed to be circular as

$$p_k = \rho[\cos(\frac{k}{K}\Omega), \sin(\frac{k}{K}\Omega)]^T, \quad \forall k \in \{0, \ldots, K-1\}, \tag{6.10}$$

where ρ is a constant radius of the circular movement, K is the total number of sample points and Ω controls the size of the circle sector. The ambiguity function (4.7) becomes

$$C(\Theta) = \left| \sum_{k=0}^{K-1} \exp\left(-i[(\delta_f^\star - \delta_f)k + \rho(\cos(\frac{k}{K}\Omega - \theta^\star) - \cos(\frac{k}{K}\Omega - \theta))]\right) \right|^2. \tag{6.11}$$

Let $K = 20$ and ψ and δ_f be chosen as before. Figure 6.3 shows how the ambiguity function varies with the choice of Ω together with a fixed $\rho = \lambda$. When a larger sector of the circle is covered, there is less ambiguity between AoA and frequency error. In order to get a narrow peak around the true value, a half turn is needed.

The Fisher information matrix for the circular case can be calculated using the general formula for any movement,

$$\text{FIM} = \frac{2}{\sigma^2} \begin{bmatrix} K & 0 & 0 \\ 0 & a^2 \sum_{k=0}^{K-1} \langle p_k, \mathsf{e}(\theta)^\perp \rangle^2 & a^2 \sum_{k=0}^{K-1} \langle p_k, \mathsf{e}(\theta)^\perp \rangle k \\ 0 & a^2 \sum_{k=0}^{K-1} \langle p_k, \mathsf{e}(\theta)^\perp \rangle k & a^2 \sum_{k=0}^{K-1} k^2 \end{bmatrix}, \tag{6.12}$$

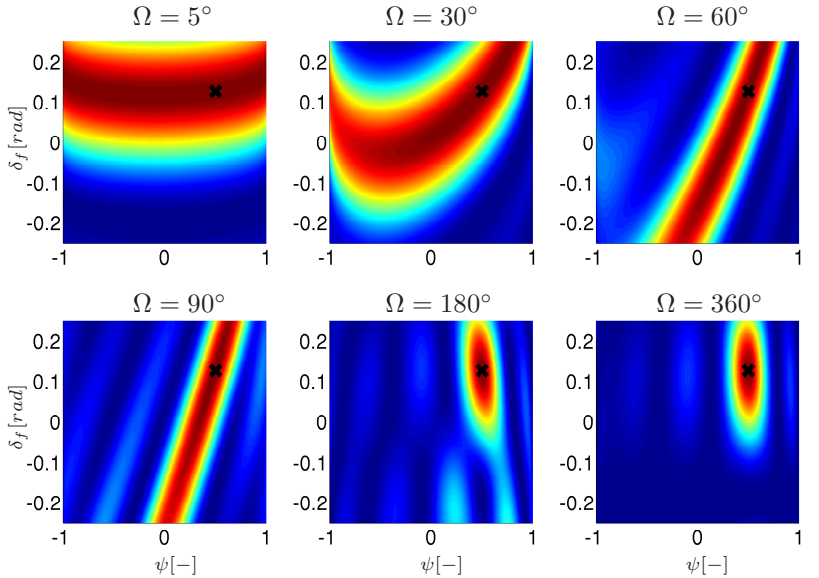

Figure 6.3 The ambiguity function as a level curve of δ_f and ψ for circular movement of $\Omega = 5°$, $30°$, $60°$, $90°$,$180°$ and $360°$ with $\rho = \lambda$. The black cross is where $[\psi^\star,\delta_f^\star]$ is located. After a turn of $180°$, the ambiguity between AoA and frequency error is removed.

where

$$\mathsf{e}(\theta)^\perp = \frac{\partial \mathsf{e}(\theta)}{\partial \theta} = [-\sin(\theta), \cos(\theta)]^T. \tag{6.13}$$

6.2 AoA estimation algorithm benchmark

The two sparse convex estimation algorithms presented in Section 4.1 are both capable of providing an estimate of the AoA if the position is known or well estimated. Before choosing which one to use for AoA estimation, a benchmark test is performed.

The scenario considered is the following. A virtual array with exact information about the position of the sample points is considered. The array is formed by moving the receiver along the x-axis with a constant velocity $v_x = 5\ \lambda/\text{s}$, sampled at 50 Hz, and the AoA is estimated for different lengths of the array and different reasonable levels of SNR of the received signal. The frequency error of the receiver is assumed to be zero, *i.e.*, $\delta_f(t) = 0$. Three rays are directed towards the array from angles θ^1, θ^2 and θ^3 so that

$$\psi^1 = 0.8, \quad \psi^2 = 0.2, \quad \text{and} \quad \psi^3 = -0.4, \tag{6.14}$$

wherein $\psi^r = \cos(\theta^r), \forall r$ and with amplitudes of

$$a^1 = 2, \quad a^2 = 5, \quad \text{and} \quad a^3 = 10, \tag{6.15}$$

respectively. The set $\Omega = [0, \pi]$ is chosen as the search grid for possible AoA, thus allowing negative amplitudes. The set is divided into 200 equidistant grid points. By this choice, the correct values in (6.14) are placed between grid points.

The algorithms are both implemented using the CVX toolbox [CVX, 2013]. The three largest peaks of the resulting spectrum are extracted and denoted by $\hat{\theta}^1$, $\hat{\theta}^2$ and $\hat{\theta}^3$ respectively. A typical spectrum from the iterative ℓ_1 algorithm after two runs with $\epsilon = 10^{-3}$ and $c = 0.2$ is shown in Figure 6.4. The corresponding amplitudes of the peaks are denoted by $\hat{a}^1$, $\hat{a}^2$ and $\hat{a}^3$ and calculated using the least squares solution of A to $y = SA$ with

$$S = \begin{bmatrix} s^1 & s^2 & s^3 \end{bmatrix} = \begin{bmatrix} 1 & 1 & 1 \\ \exp\left(-i\langle p_1, \mathsf{e}(\hat{\theta}^1)\rangle\right) & \exp\left(-i\langle p_1, \mathsf{e}(\hat{\theta}^2)\rangle\right) & \exp\left(-i\langle p_1, \mathsf{e}(\hat{\theta}^3)\rangle\right) \\ \vdots & \vdots & \vdots \\ \exp\left(-i\langle p_K, \mathsf{e}(\hat{\theta}^1)\rangle\right) & \exp\left(-i\langle p_K, \mathsf{e}(\hat{\theta}^2)\rangle\right) & \exp\left(-i\langle p_K, \mathsf{e}(\hat{\theta}^3)\rangle\right) \end{bmatrix}. \tag{6.16}$$

The peak with the largest amplitude is assumed to belong to $\hat{\theta}^3$, the second largest to $\hat{\theta}^2$, and so on. The root mean square error (RMSE) for amplitude is calculated as

$$\mathrm{RMSE}_a = \sqrt{\frac{1}{3N} \sum_{r=1}^{3} \sum_{n=1}^{N} (\hat{a}_n^r - a^r)^2}, \tag{6.17}$$

where N=100 is the number of Monte Carlo runs performed for each array size. The RMSE for the AoA estimate is calculated as

$$\mathrm{RMSE}_\psi = \sqrt{\frac{1}{3N} \sum_{r=1}^{3} \sum_{n=1}^{N} \min(|\hat{\psi}_n^r - \psi^r|, 1)^2}. \tag{6.18}$$

The saturation is introduced to reduce impact of outliers present after detection. For comparison, the quotient between the RMSE for the two algorithms is introduced as

$$\kappa_\psi = \frac{\mathrm{RMSE}_\psi^{\ell_1}}{\mathrm{RMSE}_\psi^{\mathrm{SPICE}}} \tag{6.19}$$

$$\kappa_a = \frac{\mathrm{RMSE}_a^{\ell_1}}{\mathrm{RMSE}_a^{\mathrm{SPICE}}} \tag{6.20}$$

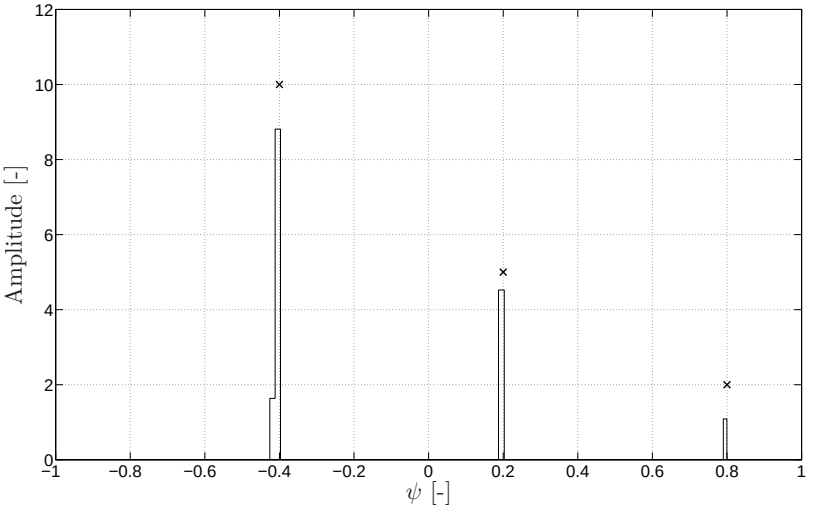

Figure 6.4 A typical spectrum of the ℓ_1 recursive algorithm. The crosses mark the true AoA and amplitude. The locations of the rays are correctly estimated but the estimated amplitude is too low. Note that there is a small component next to the largest peak.

and the result is presented in Figure 6.5.

For long arrays with high SNR, the algorithms perform equally well for both amplitude and AoA. For low SNR situations, the iterative ℓ_1 algorithm performs better than SPICE for ψ of all array sizes. However, for short arrays the amplitude estimation of the iterative ℓ_1 algorithm is less accurate than SPICE but since the AoA is believed more important compared to amplitude, the iterative ℓ_1 algorithm is picked as the favorable algorithm of the two, despite the need for adjusting three parameters. The execution time for running the iterative ℓ_1 algorithm twice is approximately 3.5 times longer compared to SPICE.

6.3 Virtual array size trade-off

There is a clear trade-off between array size and AoA estimation accuracy when using position estimates instead of true positions. A longer virtual array will collect more data and make the AoA estimate more accurate. However, the accuracy of the position estimates deteriorate due to noise in the IMU, see Section 3.1. Therefore the information from later samples will affect the estimate in a negative way. Also, the frequency error in the receiver makes the radio signal from later samples more unreliable. For the batch AoA algorithms presented before, these two error sources are not taken into

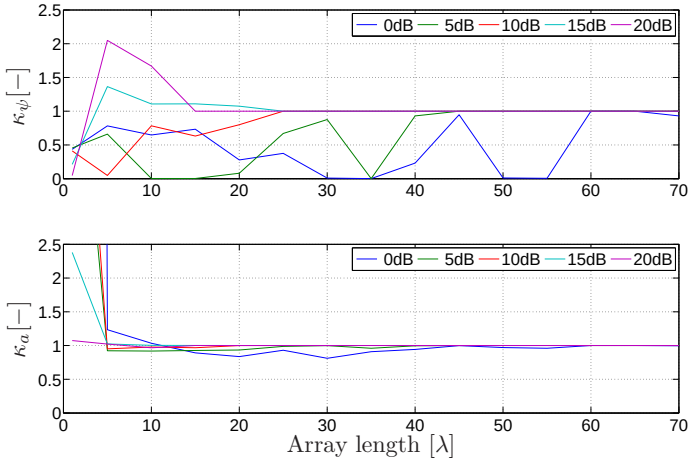

Figure 6.5 κ_ψ and κ_a for five different values of SNR of the radio signal. A value larger than 1 indicates that SPICE is better than the reweighted ℓ_1 algorithm. For long arrays with high SNR the algorithms perform equally well for both amplitude and AoA estimation. For low SNR situations, the iterative ℓ_1 algorithm performs better than SPICE for ψ of all array sizes. However, for short arrays the amplitude estimation of the iterative ℓ_1 algorithm is less accurate. Since the performance of the reweighted ℓ_1 algorithm is better for low SNR, this algorithm is chosen.

account thus leading to an error in the estimated AoA. Since the iterative ℓ_1 algorithm was chosen instead of SPICE, the former will be used in this simulation.

To study the influence of the IMU accuracy vs AoA estimation with frequency error in the receiver, the following scenario is considered. The receiver is moved with a constant velocity of 5 λ/s, sampled at 50 Hz, along the x-axis. One IMU of consumer grade and another one of industrial grade from Table 1.1 are considered for two different test cases. For convenience, the velocity random walk noise value is normalized with λ and presented in Table 6.1. Since the angle stability level is not reached with these short simulations, see Table 1.1, the bias stability for the gyroscope is neglected here.

The position is estimated with dead reckoning without assistance from the radio signal. Figure 6.6 shows how the standard deviation of the position grows with respect to array size. When the array has reached a certain length, the AoA algorithm is executed with the data acquired up to the current array size.

	Velocity Random Walk $[\lambda/s/\sqrt{\text{h}}]$	Angle Random Walk $[^\circ/\sqrt{\text{h}}]$
Consumer	1.2	2
Industrial	0.6	0.2

Table 6.1 The two IMU cases considered in the test case. The bias stability level is not considered here due to the short lengths of the simulations.

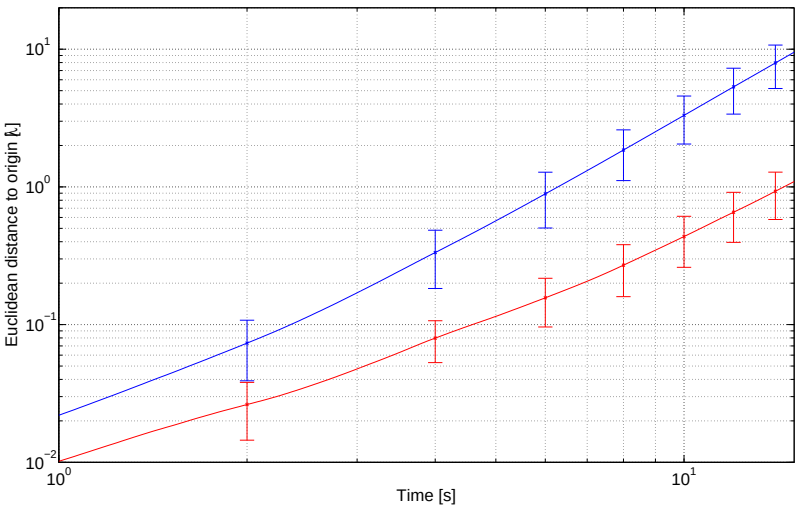

Figure 6.6 Position drift and standard deviation using dead reckoning for the two IMU cases presented in Table 6.1. The cases are marked as (-) for consumer and (-) for industrial grade IMU.

The radio environment is configured in the same way for both test cases. The SNR of the radio signal is set to 20 dB since this is a reasonable level of achievable SNR in channel estimation. Further, two rays are directed towards the array from angle $\theta^1 = 45^\circ$ and $\theta^2 = 125^\circ$ with amplitudes of $a^1 = 1$ and $a^2 = 2$ respectively. The search set Ω for possible AoA is once again chosen as $\Omega = [0, \pi]$ divided into 200 equidistant grid points.

The two largest peaks identified in the spectrum are denoted by $\hat{\theta}^1$ and

$\hat{\theta}^2$ respectively, and the least squares solution of $y = SA$ is calculated with

$$S = \begin{bmatrix} s^1 & s^2 \end{bmatrix} = \begin{bmatrix} 1 & 1 \\ \exp\left(-i\langle p_1, \mathsf{e}(\hat{\theta}^1)\rangle\right) & \exp\left(-i\langle p_1, \mathsf{e}(\hat{\theta}^2)\rangle\right) \\ \vdots & \vdots \\ \exp\left(-i\langle p_K, \mathsf{e}(\hat{\theta}^1)\rangle\right) & \exp\left(-i\langle p_K, \mathsf{e}(\hat{\theta}^2)\rangle\right) \end{bmatrix}, \tag{6.21}$$

where p_k is the dead reckoned position at time k. The solution gives the complex amplitudes, $\hat{\alpha}^1$ and $\hat{\alpha}^2$. Further, six levels of constant frequency errors are chosen for evaluation of its influence on AoA accuracy. The frequency error is given with the unit of $^\circ/\lambda$, *i.e.*, for every λ moved, the phase of the measurement signal has rotated a number of degrees due to the frequency error.

To compare the scenarios against each other, 100 Monte Carlo runs are executed for each array size and for each frequency error the RMSE of the AoA and amplitude is calculated according to (6.17) and (6.18). The results from the simulations are shown in figures 6.7 and 6.8 respectively.

For the IMU of consumer grade, the batch AoA estimation works well up to array sizes of 20 λ. For longer arrays, the performance deteriorates rapidly. Also, the phase drift is clearly setting a limit on the accuracy of the AoA estimation but the same effect is not seen in the amplitude estimation. Apparently a small offset in the AoA does not affect the estimated amplitude. For the IMU of industrial grade, the size of array does not affect the AoA estimation performance very much for sizes up to 70 λ. For the amplitude estimation, there is a smaller dependence on the array size than before. Hence, using an IMU of industrial grade, the accuracy of the position estimates using dead reckoning seems to be enough for doing batch AoA estimation when moving at this speed. Therefore, the tactical grade IMU from Table 1.1 is not considered here.

To study influence of SNR on the radio signal two frequency errors are chosen, $0^\circ/\lambda$ and $36^\circ/\lambda$, and the scenario with SNR of 0 dB, 10 dB and 20 dB for the two different IMU cases is compared. The RMSE for AoA and amplitude is presented in Figure 6.9.

For the consumer grade IMU, there is little impact on the AoA estimation at different SNR levels. The curves are very similar to the case in Figure 6.7. However, for the amplitude estimation, the situation is different. There is a clear dependence between amplitude estimation accuracy and SNR for short arrays. For longer arrays, larger than 20 λ, the difference is smaller and for long arrays there is no difference.

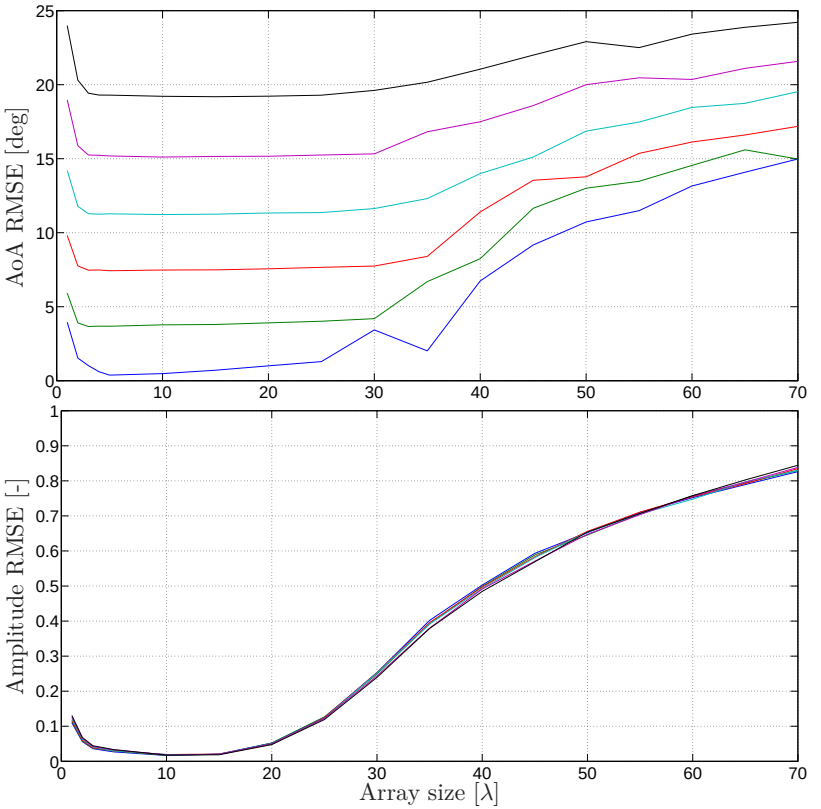

Figure 6.7 The upper panel shows the RMSE for AoA estimation with respect to array size while the lower shows the amplitude estimation. The position estimates are calculated with dead reckoning and an IMU of consumer grade is used. The lines indicate the level of phase drift in the simulation as 0, 18, 36, 54, 72 and 90 $^\circ/\lambda$. Note that the RMSE of AoA and amplitude deteriorate at array lengths larger than 20 λ.

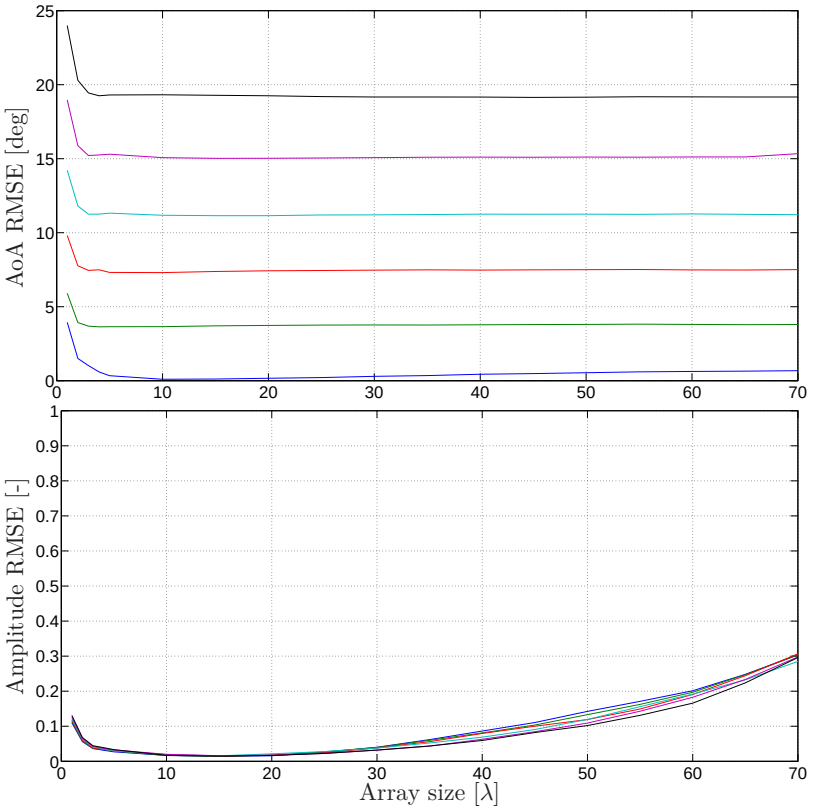

Figure 6.8 Same as Figure 6.7 but with an industrial grade IMU. Note that the AoA accuracy is independent of array length.

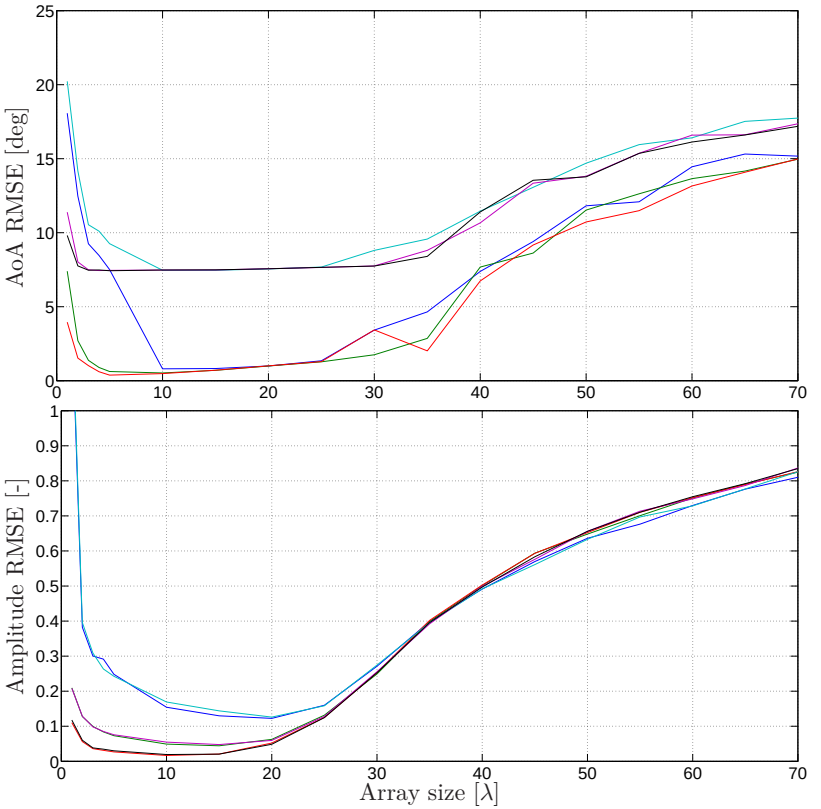

Figure 6.9 The upper panel shows the RMSE for AoA estimation with respect to array size while the lower shows the amplitude estimation. The position estimates are calculated with dead reckoning and an IMU of consumer grade is used. The lines indicate the level of phase drift and SNR in the simulation as [0,0], [0,10], [0,20], [0,36], [10,36] and [20,36] [dB,°/λ]. Note that the RMSE of AoA deteriorates at array lengths larger than 20 λ, independently of SNR.

6.4 Joint pose and radio channel estimation: Performance bounds

To study the performance bounds of the joint pose and radio channel estimation problem, the recursive Cramér-Rao bound for the state space model derived in Chapter 3 is calculated using the extended Kalman filter presented as Algorithm 2. Two different movements are used, a linear one and a sawtooth movement similar to the ones in Section 6.1.

Linear movement

The first scenario is a linear movement along the x-axis with constant velocity $|v_x(t)| \equiv v_x$. The position, measured in wavelengths, at time instance kT_s is given by

$$p_{x,k} = \quad v_x k, \quad \forall k \in \{0, \ldots, K-1\}, \tag{6.22}$$

where $v_x = 0.2\pi$ and $K = 3000$. To study the influence of the number of rays impinging on the array, three cases with this movement are studied: one, two, and three impinging rays respectively. The radio channel parameters are given by

$$\begin{aligned} \alpha^1 &= 1\exp(-i0.4), \quad \theta^1 = \pi/4 \\ \alpha^2 &= 3\exp(-i2.1), \quad \theta^2 = \pi/2 \\ \alpha^3 &= 2\exp(-i5.3), \quad \theta^3 = -5\pi/6 \end{aligned} \tag{6.23}$$

and the SNR for the received signal is 20 dB. The configuration of the radio channel is kept constant throughout the whole movement. The simulation results for the three cases are shown in figures 6.10, 6.11, and 6.12.

The result with one impinging ray reveals that even though the radio signal is used, there is no change of the growth rate in the uncertainty of the position estimate. This is consistent with previous results; one ray does not provide any information perpendicular to the AoA, see Figure 2.3, and the uncertainty can therefore increase in this direction. Hence, one ray alone can not significantly increase the accuracy of the estimated position. The AoA and the phase estimate are both unaffected by the radio signal since without any accuracy in the position, there is no way to estimate these states either. The only state that can be estimated with some accuracy is the amplitude. This is because the measurements depend linearly on the amplitude.

The result with two impinging rays in Figure 6.11 shows an improvement of approximately 40 times for the position estimate, but the asymptotic growth rate is unaffected. The variances of the AoA and the phase for the rays are still growing without any change. Also, the amplitude that before was bounded is now slowly growing. This is due to the ambiguity of estimating the individual components in a sum. Thus, two rays with a linear movement is not sufficient to estimate the position or the radio channel accurately.

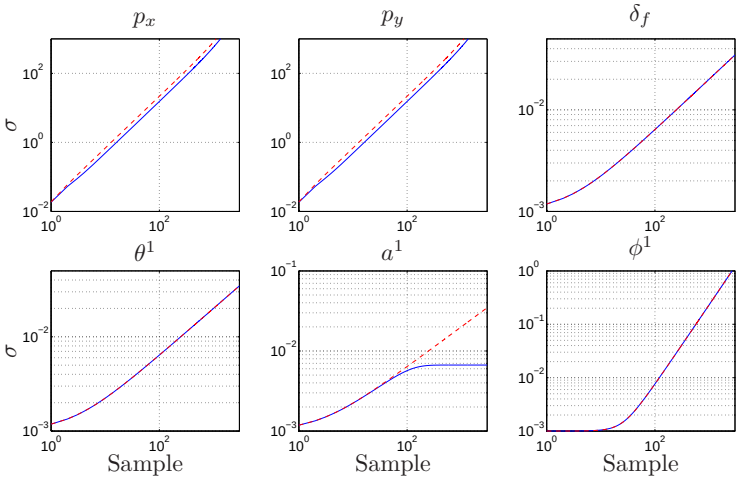

Figure 6.10 Cramér-Rao bound of state estimation with one ray impinging on the array with linear movement in one direction. The y-axis shows standard deviation versus sample on x-axis for the states p_x, p_y, δ_f, θ^1, a^1, and ϕ^1. The red curve shows the case when no radio signal is supplied. There is a small performance improvement of $\sqrt{2}$ in position accuracy, but the asymptotic growth rate is not improved.

With three impinging rays the result is similar to the previous case. The variance of the position is growing, but the variance of θ^1 has decreased. This is due to the choice of θ for ray 1. For the other states, there is not enough information in the radio signal and the movement to estimate them.

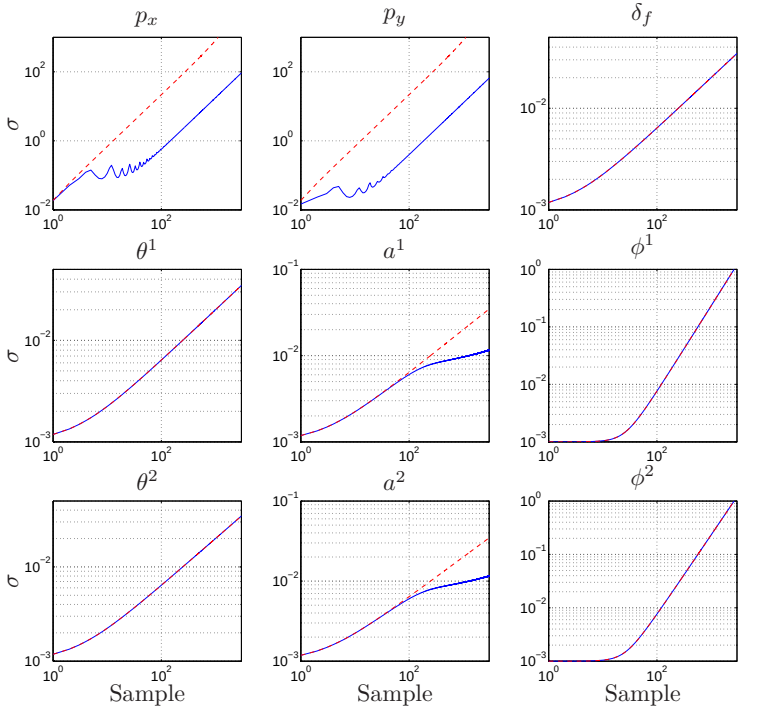

Figure 6.11 Same as Figure 6.10 but with two rays. The improvement in position accuracy is approximately 40 times but the asymptotic growth rate is unaffected. The variances of the AoA and the phase for the rays are still growing without any change compared to the single ray case. Also, the amplitude that before was bounded has now become slowly growing.

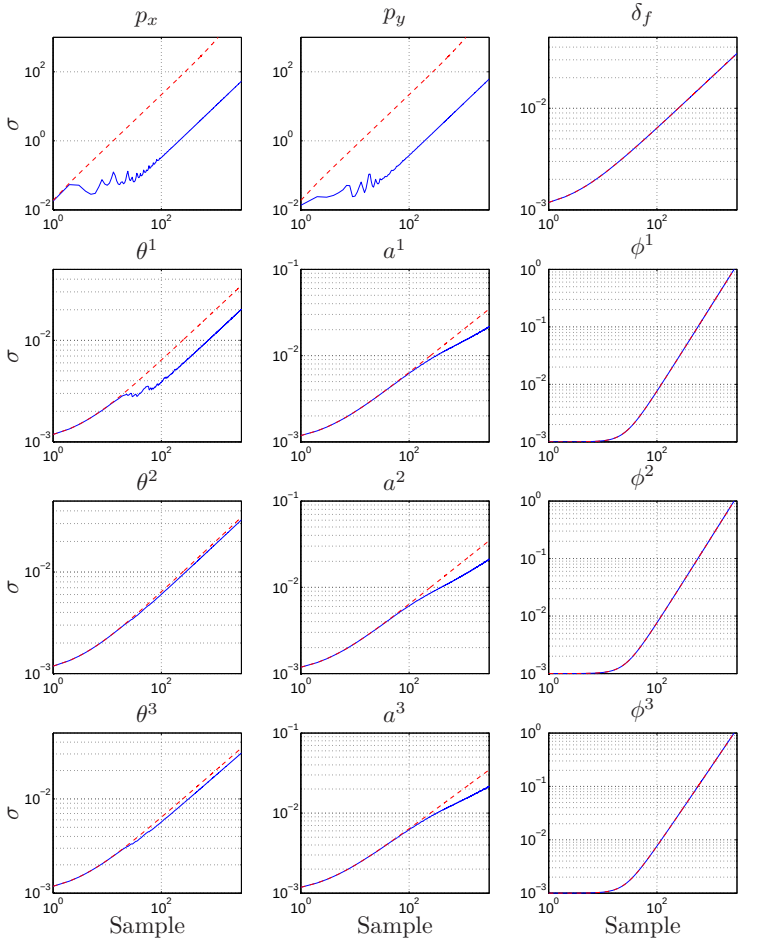

Figure 6.12 Same as Figure 6.10 but with three rays impinging on the array. The result is similar to the case with two rays.

Sawtooth movement

For the second scenario, the movement is still a liner movement along the x-axis. The difference is that the receiver is now moving back and forth with constant speed $v_x(t) \equiv v_x$, starting at the origin. The position at time instance kT_s is given by

$$p_{x,k} = \begin{cases} v_x k, & \forall k \in \{0, \ldots, K-1\} \\ v_x(2K-k-1), & \forall k \in \{K, \ldots, 2K-1\} \\ v_x(2K-k), & \forall k \in \{2K, \ldots, 3K-1\} \\ v_x(-4K+1+k), & \forall k \in \{3K, \ldots, 4K-1\} \end{cases} \tag{6.24}$$

The movement is repeated 10 times before the receiver is put to rest for 30000 samples. The radio channel is assumed to be as before with an SNR of 20 dB. Let K be 750 making this scenario identical to the previous scenario up to $k = 750$. The simulation results from the case of one, two and three rays are presented in figures 6.13, 6.14, and 6.15 respectively.

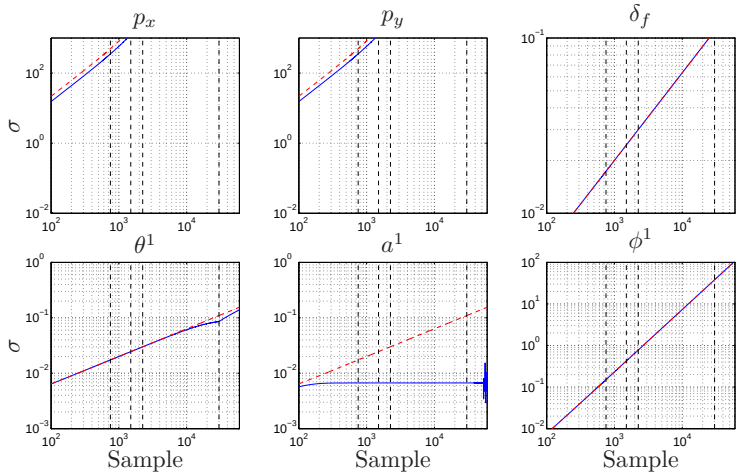

Figure 6.13 Cramér-Rao bound of state estimation with one ray impinging on the array with sawtooth movement. The y-axis shows standard deviation versus sample on x-axis for the states p_x, p_y, δ_f, θ^1, a^1, and ϕ^1. The red curve shows the case when no radio signal is supplied. The dashed lines mark the events K, $2K$, $3K$, and $40K$ respectively. The result is identical to the case with linear movement. The variance of the amplitude shows some numerical noise at the very end.

This result is identical to the previous scenario: there is a performance improvement of $\sqrt{2}$ of the accuracy for the position but the asymptotic growth rate is not affected. Still, the only state that can be estimated with bounded accuracy is the amplitude due to the same reason as previously.

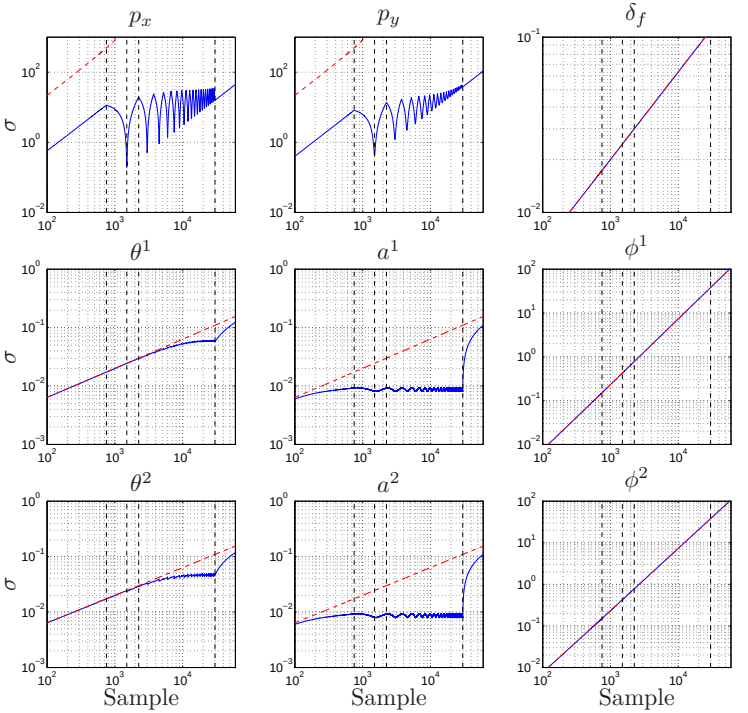

Figure 6.14 Same as Figure 6.13 but with two rays. There is clear improvement in the position accuracy due to the richer movement. After the movement has stopped at $k = 40K$, the variance of amplitude and the AoA increases again since the algorithm can not estimate the states when the receiver is stationary.

For the case with two impinging rays there is a clear benefit in position, amplitude, and AoA. The variance of the position decreases when the movement changes direction towards the origin. After the origin is passed, the variance increases again. Clearly there is a dependence between the distance from origin and with what accuracy the position can be estimated. This is due to the ray-trace based model used for modeling the radio channel. A small variation of θ, when the receiver is far away from the origin, will have a bigger impact on the phase of the received signal compared to if the receiver is kept close to the origin. Looking at the amplitude estimates, the variance decreases when the movement changes direction and behaves in the same way as the variance of the position. Finally, the variance of the AoA is limited as long as the receiver is moving. Thus, a stationary receiver can never estimate the AoA.

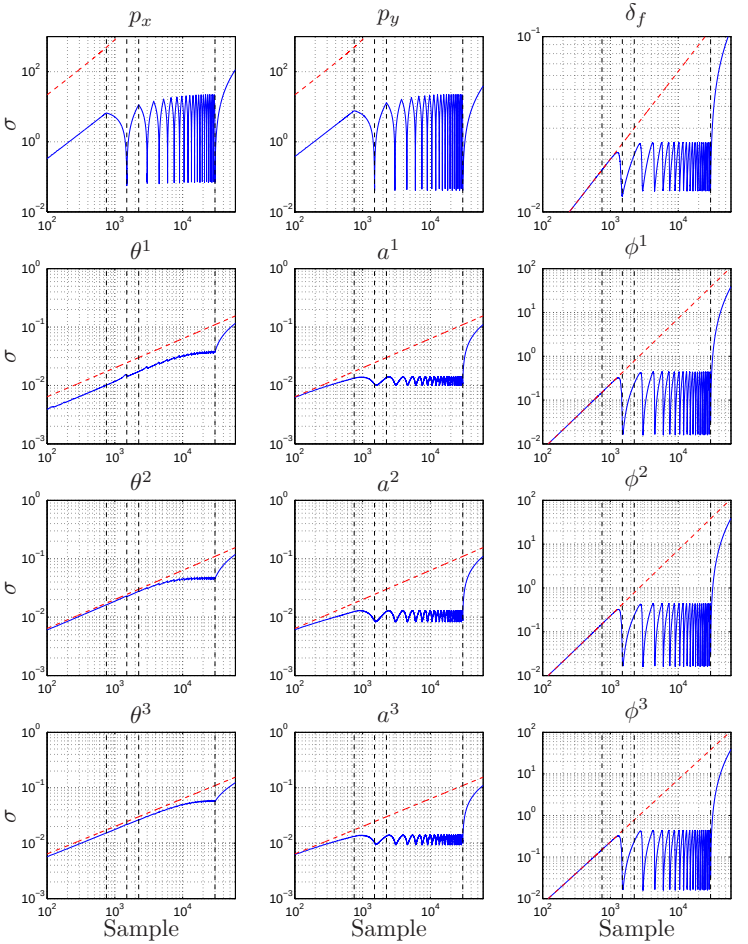

Figure 6.15 Same as Figure 6.13 but with three rays. Note that the asymptotic growth rate of the position estimates has been decreased and it is also possible to estimate the frequency error and argument of the complex amplitude ϕ. After the movement has stopped at $k = 40K$, the variance of all states starts to grow again since the information from a stationary receiver does not provide any information to estimate them.

The case with three impinging rays with a movement in two directions shows great improvement compared to the case with two rays. The growth rate of the variance of the position is reduced as long as the receiver is moving. As soon as it is stopped, the variance grows with the same rate as before. The result for amplitude and AoA is similar to the previous case. However, for the phase and frequency error the variance is reduced when the receiver passes the origin.

Summary

The Cramér-Rao calculations show promising results for the joint estimation problem. If the movement is rich enough and three rays impinge on the array, all states can be estimated with bounded growth rate of the variance, given that the receiver is moving. This is a huge improvement of the performance of the INS compared to the unaided case. For the cases with one ray, some performance improvement is seen but the asymptotic growth rate is still present. The reason for the limited performance in these cases is the plane wave propagation assumption, see Section 2.1. However, with two rays and a sawtooth movement, the analysis reveals that the variance of both amplitude and AoA estimation is bounded.

6.5 Joint pose and radio channel estimation: Estimation performance

The marginalized particle filter from Algorithm 4 has been implemented in Matlab. The number of particles and impinging rays to track can be altered. Also, a trajectory moving in both X and Y was generated and sampled at 50 Hz. The movement starts and ends in the origin and the full movement takes 30 seconds to complete. Note that it takes approximately 5 seconds before the movement is initiated. The trajectory was converted to accelerometer readings with additive white noise with intensity similar to an IMU of consumer grade, see Table 6.1. During the movement, the device is assumed to have a fixed orientation, *i.e.*, the gyroscope signal is white Gaussian noise with intensity similar to the consumer grade IMU. For this trajectory, no random walk process for the accelerometer or the gyroscope has been included due to the short movement. For time periods of 30 seconds, the white Gaussian noise is still the dominant part of the noise signal, see Table 1.1. Also constant bias in the sensors has been neglected since the calibration error is assumed to be small.

The results shown from the simulations with the filter are compared to the dead reckoning scheme of the IMU signal, see Figure 1.1. Due to the ambiguity of the yaw angle, see discussion in Section 3.4, the resulting trajectory has in one case been rotated slightly to fit the true trajectory better

and hence also the estimate of the AoA. For the simulation results where this has been done, it is clearly stated.

The radio environment is configured in the same way for all simulations as

$$\begin{aligned} a^1 &= 1.5, \quad \theta^1 = \pi/3, \\ a^2 &= 0.9, \quad \theta^2 = 2\pi/3, \\ a^3 &= 2, \quad \theta^3 = -2\pi/3, \end{aligned} \tag{6.25}$$

and the argument of the complex amplitude is chosen from $\mathcal{U}(-\pi, \pi)$. The SNR of the radio signal is as before set to 20 dB.

Static radio channel

The calculation of the Cramér-Rao bound in the previous section showed that one impinging ray does not contain enough information to significantly improve the pose estimation and this case is therefore not simulated. The first test of the filter is a static channel with two and then three impinging rays. For the case with two rays, 1 and 2 from (6.25) are used and the filter is set to 600 particles. For three rays, the number of particles is increased to 2000 since the number of states has grown. The radio related states of the particles were initialized as in Table 6.2. The result from the simulation with two and three impinging rays is shown in Figure 6.16 and 6.17 respectively.

State	Distribution	Unit
a^1	$\mathcal{N}(1, 0.5)$	-
a^2	$\mathcal{N}(1, 0.5)$	-
a^3	$\mathcal{N}(1, 0.5)$	-
θ^1	$[\theta^1]^\star + \mathcal{U}(-20, 20)$	deg
θ^2	$[\theta^2]^\star + \mathcal{U}(-20, 20)$	deg
θ^3	$[\theta^3]^\star + \mathcal{U}(-20, 20)$	deg
ϕ^1	$\mathcal{U}(-\pi, \pi)$	rad
ϕ^2	$\mathcal{U}(-\pi, \pi)$	rad
ϕ^3	$\mathcal{U}(-\pi, \pi)$	rad

Table 6.2 The initial distributions of the states where * indicates the true AoA and $\mathcal{U}(a, b)$ is a uniform distribution between a and b. When initializing the filter, an initial estimate of the AoA is assumed to be obtained by the iterative ℓ_1 regularization algorithm presented in Section 4.1.

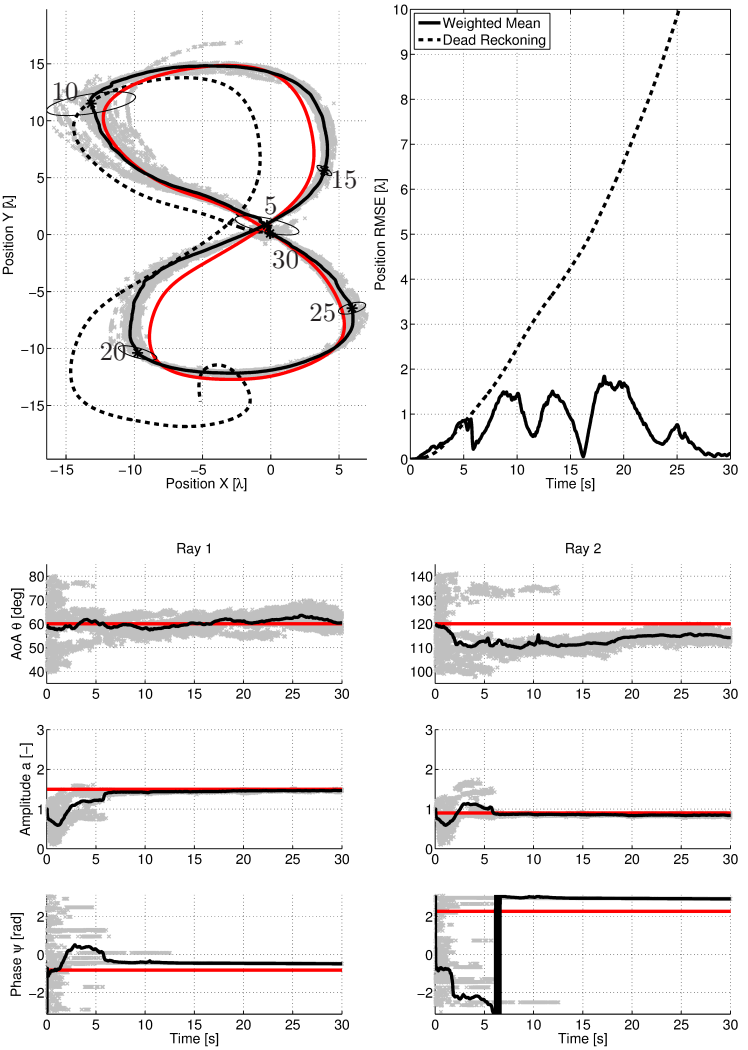

Figure 6.16 The upper left panel shows the weighted average (-), dead reckoned (- -), the ground true (-) and the 20 best particles (x) for each time instance of the trajectory. The numbers indicate the time at the given points together with the covariance ellipse. The upper right panel shows the RMSE of the position of the weighted average (-) and the dead reckoning (- -) as a function of time. The lower panel shows the estimate of AoA, amplitude and phase for each ray with the same color coding as before. Note that until the first turn, several hypotheses exist. After the turn, the filter settles on one solution. The RMSE at the end point of the dead reckoning is 16 λ compared to 0.1 λ for the sensor fusion approach.

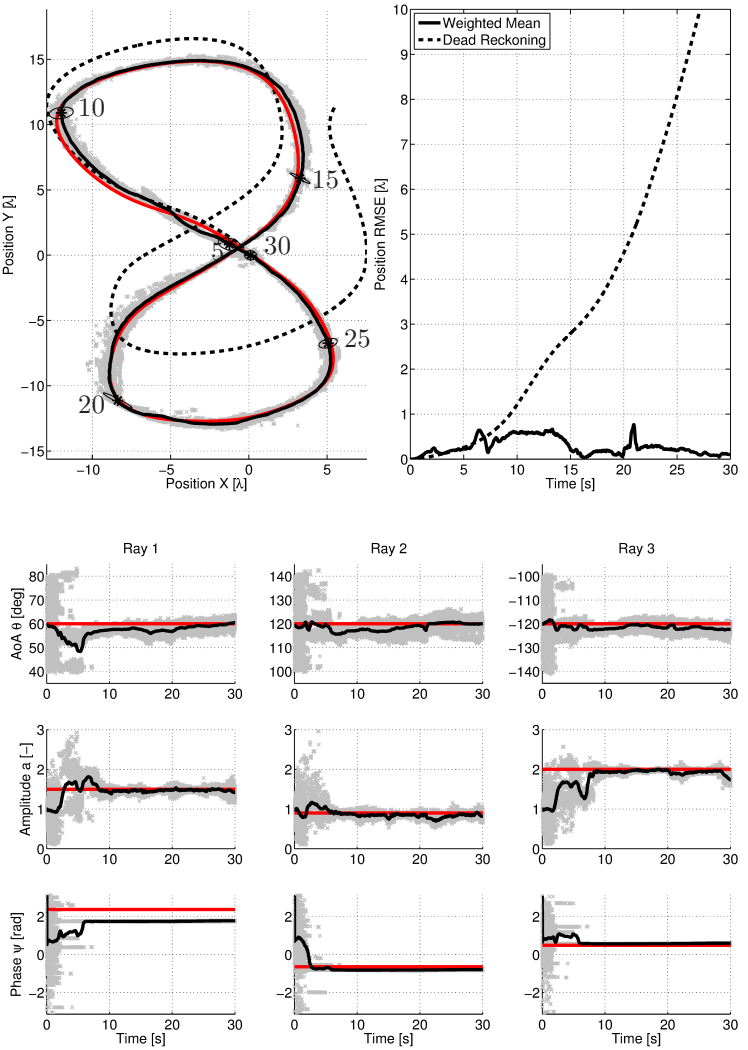

Figure 6.17 Same as for Figure 6.16 but with three impinging rays. The filter tracks the position very well and settles on the true AoA and amplitude for the three rays. However, the phase is not estimated correctly. The RMSE at the end point of the dead reckoning is 13 λ compared to 0.1 λ for the sensor fusion approach.

The position estimate errors for the case with two rays are below 2 λ throughout the whole movement in this simulation. Also, after the first turn, the filter has enough information to remove some hypotheses and settle on one value for the AoA. This result is consistent with the previous result. The AoA and amplitude states converge to the true values while the phase has some offset but it does not affect the position estimates. With three rays, the estimates converge to the true states in a similar way and the RMSE for position estimate errors are lower compared to two impinging rays. Both cases shows great improvement in position RMSE by using the radio information compared to the dead reckoning approach. The simulation results look very promising.

Dynamic radio channel

To test the dynamics of the estimates, some amplitude variations are simulated on the different rays for two and three rays respectively, see figures 6.18 and 6.19.

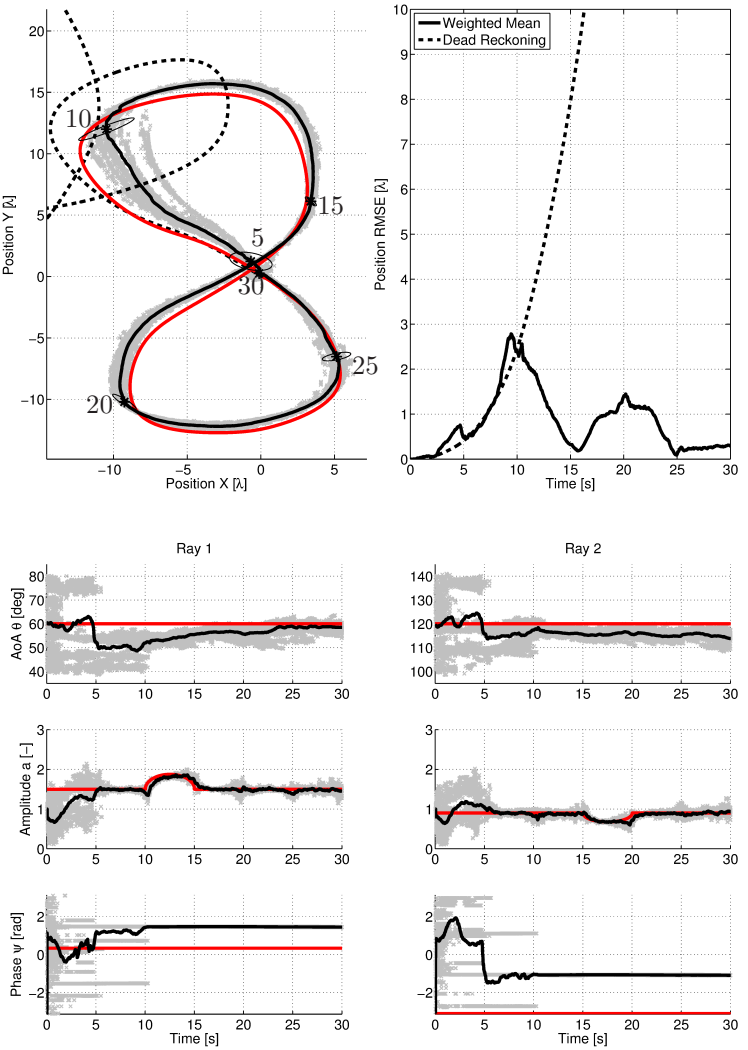

Figure 6.18 Same as in Figure 6.16 but with amplitude variations at 10 and 15 seconds. Note that the filter is able to track these variations without affecting the position estimates. The RMSE at the end point of the dead reckoning is 48 λ compared to 0.3 λ for the sensor fusion approach.

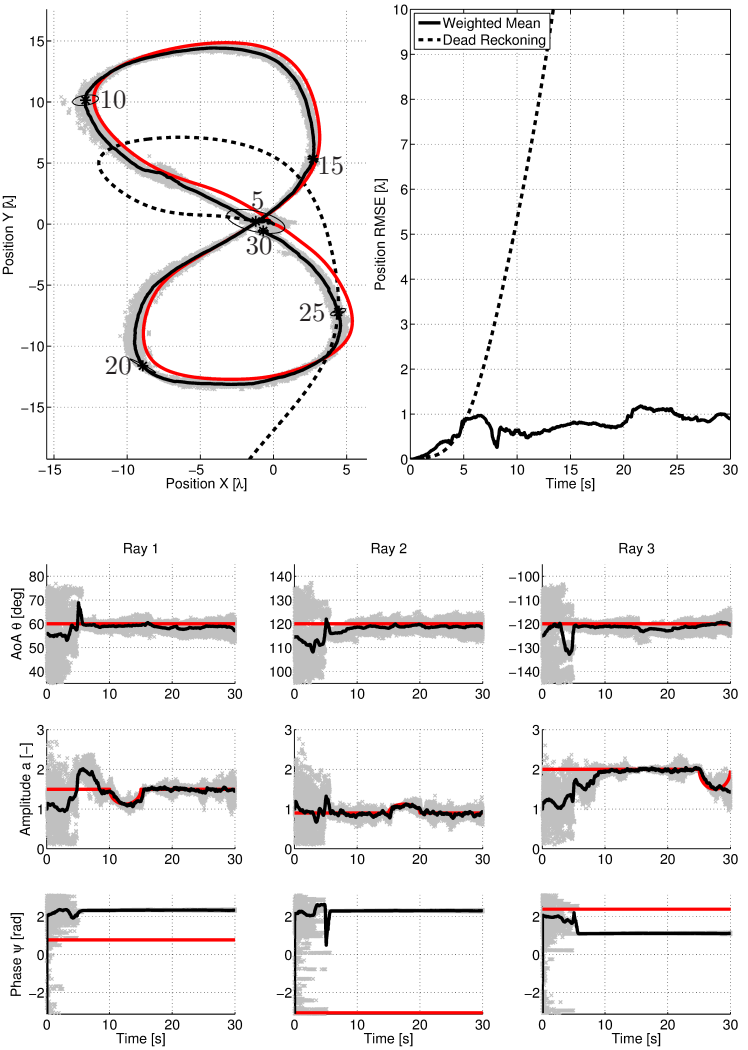

Figure 6.19 Same as in Figure 6.17 but with three rays and amplitude variations at 10, 15, and 25 seconds respectively. The result has been rotated 5 degrees. The filter manages to track the position well during amplitude variations. The RMSE at the end point of the dead reckoning is 65 λ compared to 0.9 λ for the sensor fusion approach.

For the case of two impinging rays in Figure 6.18, the filter tracks the amplitude disturbances at 10 and 15 seconds while maintaining a good estimate of the position. After the second disturbance, the position RMSE has increased to approximately 1.5 λ. The performance is similar to the case with three impinging rays in Figure 6.19. The filter tracks the amplitude disturbances at 10, 15, and 25 seconds well even if the filter does not settle at the true value after the last disturbance. The peak position RMSE is around one λ for this realization.

Frequency error estimation

To test the filter for its ability to estimate position when there is phase noise present from the receiver, a frequency error as

$$\delta_f(t) = \begin{cases} 0.1, & t \leq 15 \\ 0.1 + 0.01t, & 15 < t \leq 30 \end{cases} \quad [\text{Hz}] \tag{6.26}$$

is added to the radio signal. The only case considered here is with three impinging rays, configured as before. In Figure 6.20, the simulations show what happens if the frequency error is not estimated. The position estimate is clearly off from the ground true trajectory after ten seconds. Also, the filter tries to compensate the phase drift by adjusting the estimated AoA heavily, starting at around 15 seconds. In Figure 6.21, the estimation is enabled and the stationary frequency error is estimated as soon as the movement starts and it is also tracked during the ramp. Hence, the filter is able to track frequency errors which is necessary in order to improve pose estimation.

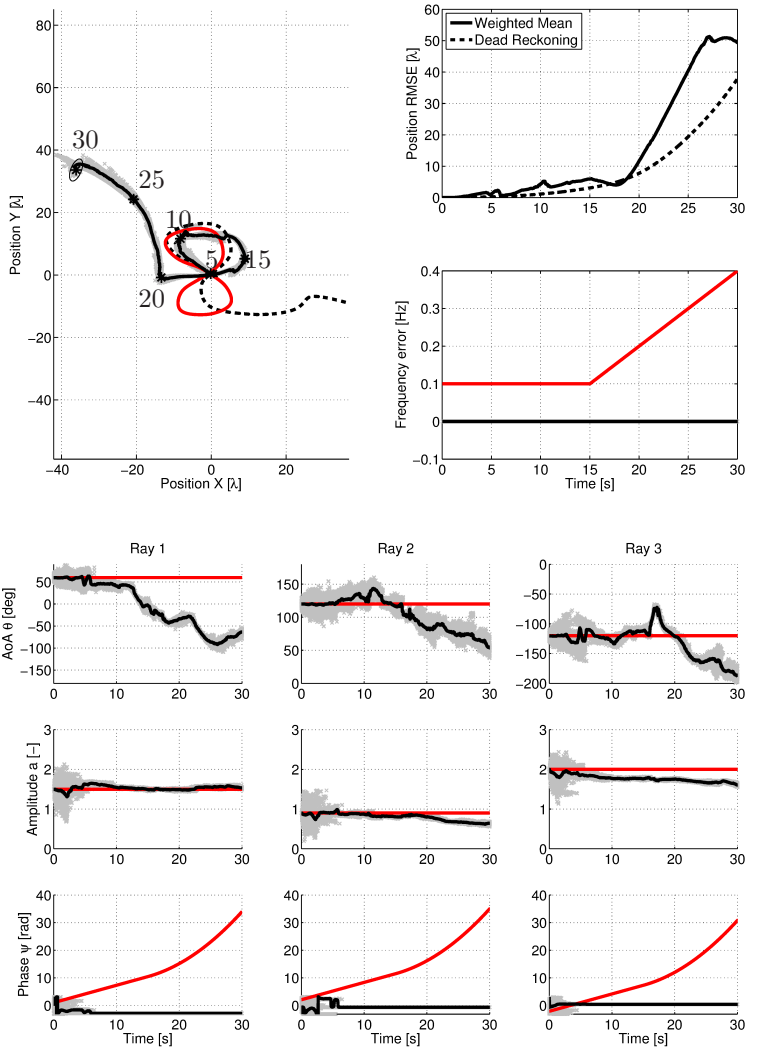

Figure 6.20 Same as in Figure 6.17 but with a frequency error added according to (6.26) but not estimated. The frequency error is shown in the second panel to the right. Note that the RMSE for the estimated position is higher than dead reckoning for the whole movement and the large changes in estimated AoA start at around 15 seconds.

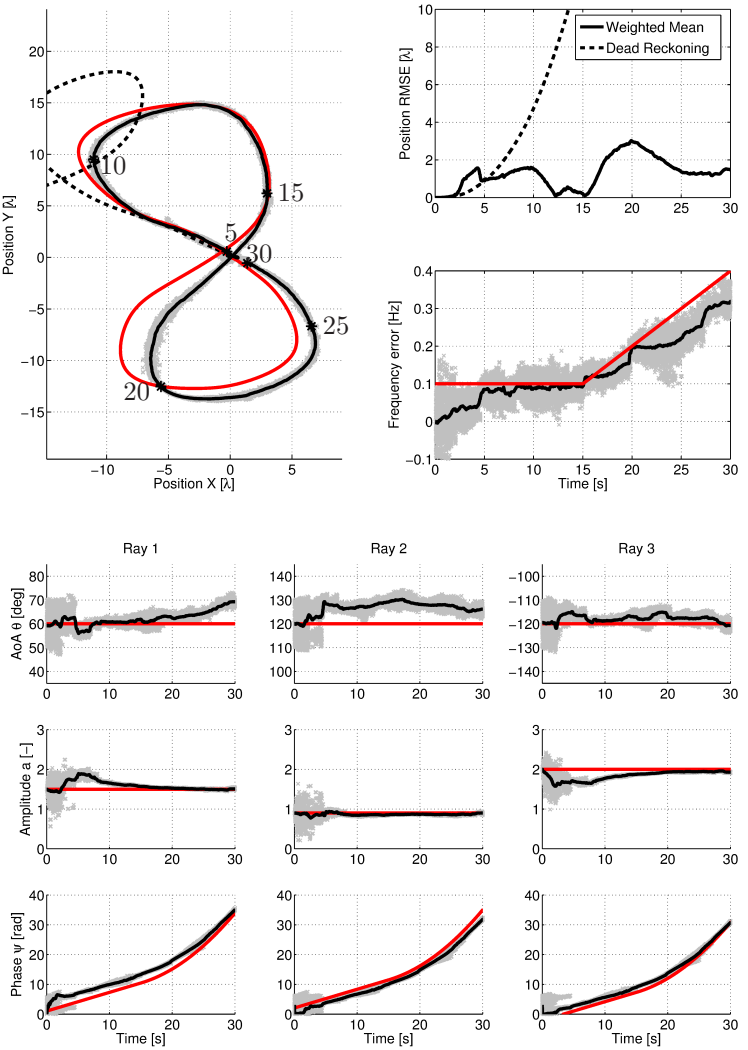

Figure 6.21 Same as in Figure 6.17 but with a frequency error added according to (6.26) and also estimated. The frequency error is shown in the second panel to the right. The filter is able to estimate both the stationary frequency error and the ramp. The accuracy of the estimated position is comparable to the scenario without frequency error. The RMSE at the end point of the dead reckoning is 78 λ compared to 1.5 λ for the sensor fusion approach..

Number of particles needed

The number of particles needed to estimate the state vector depends on the size of the state vector but also on the distributions of the states. To evaluate the number of particles needed for good convergence of the filter, the same trajectory as before is used with three impinging rays. To speed up the simulations, the same filter implementation as before is converted to C code using the Coder toolbox in Matlab. The initialization is as in Table 6.2, and six cases with 250, 500, 1000, 2000, 4000, and 8000 particles respectively are considered. For each case, 50 Monte Carlo runs are simulated. The position RMSE for all realizations is calculated and the result is presented in Figure 6.22.

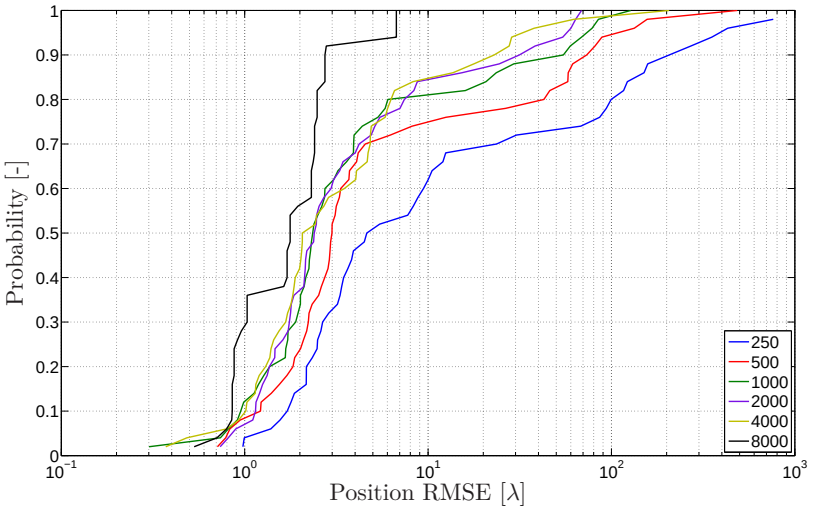

Figure 6.22 The likelihood of position RMSE for different numbers of particles is shown as a cumulative distribution function.

The result shows that at the 50% level there is very little difference between the cases with 1000, 2000, and 4000 particles and even for the rare cases with high RMSE, the difference is small. The case with 8000 particles is as expected the best one but also the most time consuming. The simulation time is presented in Table 6.3. Note that the simulation times are measured in Matlab without any particular crafting of the operations to minimize simulation time.

The movement corresponds to 30 seconds with a sample rate of 50 Hz so with the current implementation, 500 particles can be simulated in real-time. The case with 8000 particles is approximately 130 times slower than real-time but on a dedicated hardware platform, a real-time implementation would still

# Particles N	Simulation Time [s]	Simulation Time per Particle [ms]
250	14	56
500	34	68
1000	91	91
2000	301	151
4000	1090	273
8000	3980	498

Table 6.3 Average simulation time for 1500 samples for different number of particles and average simulation time per particle. The simulation time needed for each particle increases as $\approx N^{1.6}$.

be possible. The computation time as a function of the number of particles N increases as $\approx N^{1.6}$. The reason for the increase of simulation time per particle is not known. One possible explanation is that the resampling step is dominant in the algorithm but further investigation has to be made to find the cause.

Summary

The implemented filter has in simulation proven to be capable of solving the estimation problem under both static and dynamic scenarios. The filter was tested with both amplitude variations and frequency error and the results are impressive. The improvement in estimated position compared to dead reckoning is large. Also, the static case was proven to converge in Monte Carlo simulation giving a proof of repeatability of the results. The argument of the complex amplitude is, despite the Cramér-Rao analysis, challenging to estimate. The argument is not correctly estimated for all rays in any of the simulation results. However, since the estimated position corresponds well with the true one, the argument is apparently not critical to the estimation of the position.

7

Experiments

7.1 Hardware

Inertial measurement unit

The IMU used in this thesis is delivered by Phidgets [Phidgets, 2013] at a price of $150 and measures 30 × 35 mm, see Figure 7.1. This IMU contains one accelerometer, one gyroscope, and one magnetometer along each unit axis to give it a total of nine degrees of freedom. The performance of the device is comparable to what is available in cellular phones today. The magnetometers have not been used in this thesis. The software for communication with the device is implemented in LabView^{TM}.

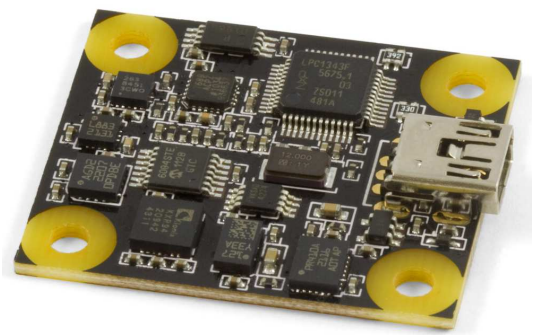

Figure 7.1 IMU 1044 from Phidgets used in this thesis. The device measures 30 × 35 mm.

Characterization and calibration The Allan deviation technique described in Section 3.1 is used for characterization of the noise sources in the IMU. The IMU is placed on a table and data is gathered for 30 minutes at a data rate of 250 Hz. The results of the accelerometers and of the gyroscopes are presented in figures 7.2 and 7.3 respectively.

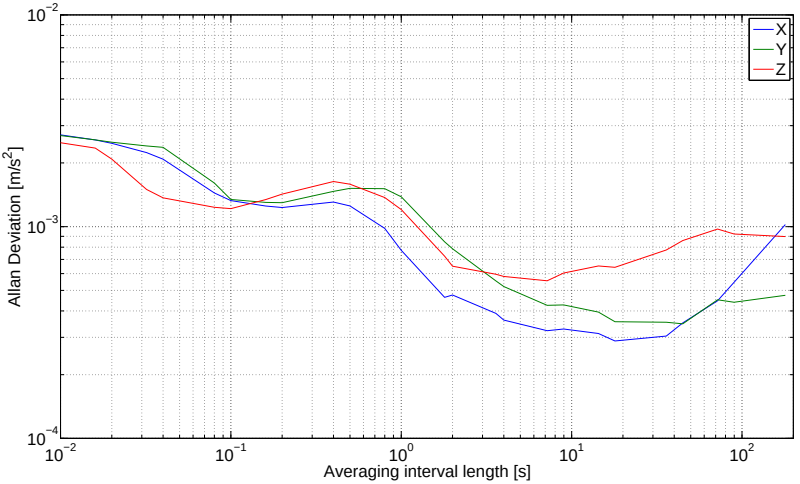

Figure 7.2 Allan deviation for the three accelerometers. There is strong indication of correlated noise at 0.5 seconds. The origin of this noise is unknown.

	Bias Instability [m/s/h]	Velocity Random Walk [m/s/$\sqrt{\text{h}}$]
X Axis	1.0 (at 18 s)	0.046
Y Axis	1.3 (at 45 s)	0.083
Z Axis	2.0 (at 7 s)	0.072

Table 7.1 Accelerometer noise parameters estimated from measurements in Figure 7.2.

The accelerometers exhibit heavy influence of correlated noise at averaging lengths of 0.5 seconds. The source of this correlated noise is unknown. The gyroscope shows better performance with less correlated noise. The IMU is among the inexpensive ones and this is reflected in the performance of the unit.

Before the IMU is used for measurements, its accelerometers are calibrated with respect to alignment, constant bias and orthogonality. The calibration scheme used here is presented in [Skog and Händel, 2006]. The reason for not calibrating the gyroscopes is that it is hard to rotate the device with a known angular speed.

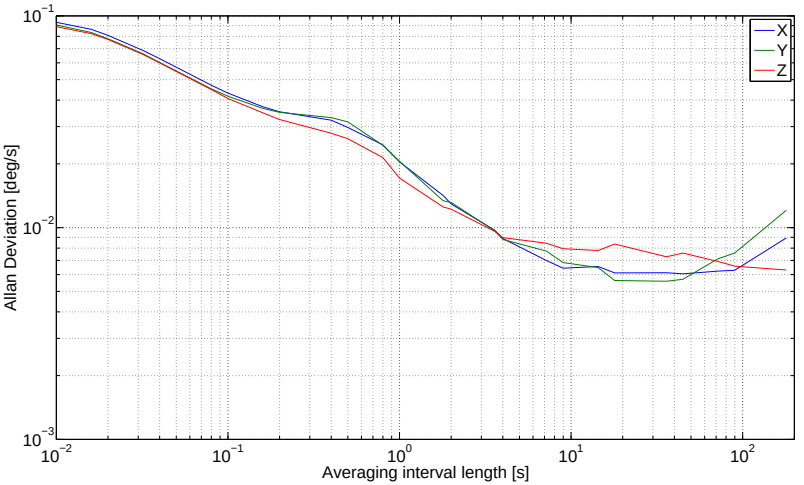

Figure 7.3 Allan deviation for the three gyroscopes. The performance resembles the ideal response in Figure 3.2.

	Bias Instability [°/h]	Angle Random Walk [°/$\sqrt{\text{h}}$]
X Axis	22 (at 45 s)	1.2
Y Axis	20 (at 35 s)	1.2
Z Axis	23 (at 180 s)	1.0

Table 7.2 Gyroscope noise parameters estimated from measurements in Figure 7.3.

Radio equipment

To be able to control the radio environment for the experiments, a complete transmitter-receiver chain has been configured. To do this a Channel Sounder known as RUSK [MEDAV, 2013] is used, see Figure 7.5. The equipment consists of one transmitter and one receiver and has the capability of measuring the radio channel impulse response from one transmitter to many receivers for radio channel characterization and analysis. Since the radio channel is reciprocal, *i.e.*, the transfer function from the transmitter to the receiver is equal to the channel going in the other direction, it does not matter which one of the receiver and the transmitter that is moving. Hence, the description of the channel sounder from here on is written as if it were to have one receiver and many transmitters where the transmitters act as controlled scattering

objects generating one ray each. By switching transmission frequency and transmitter antenna at high speed, the individual channel impulse responses at different frequencies are obtained. One benefit with this configuration is the possibility to evaluate the radio channel individual impulse responses from each transmitter to the receiver. The transmitter and receiver are synchronized to minimize uncontrolled frequency error in the experiments. A schematic of the equipment configuration is presented in Figure 7.4.

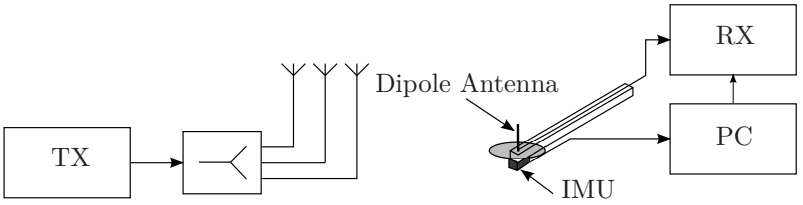

Figure 7.4 Block diagram of the equipment used for experiments. The RUSK TX is connected to a high speed multiplexer feeding the three patch antennas. The IMU and a dipole antenna with a ground plane are fixed to a wooden stick and the measurement signals are fed to a PC and the receiver respectively. Note that RUSK has several receivers and one transmitter but due to the reciprocal property of the channel, it can be considered to have several transmitters and one receiver. When the experiment starts, the PC triggers the receiver to initiate data recording.

The transmitter antennas are patch antennas, suitable for the frequency band of 2.4 GHz. The receiver antenna is a dipole antenna for the same frequency band with a ground plane to eliminate unwanted reflections.

7.2 Data gathering

The IMU data recording is synchronized with the recording of the radio signal. The sensors are recorded at 250 Hz but later down sampled to 50 Hz by averaging over five samples, see discussion in Section 5.2. The IMU is mounted together with the dipole antenna on a wooden stick, see Figure 7.6, making it easy to move them by hand without interfering with the receiver. The experiments are carried out outdoors on a rooftop with clear line of sight between the transmitter antennas and the receiver on the stick. A total number of 129 frequency points between 2.40 GHz and 2.48 GHz are recorded but only the one on 2.40 GHz is used for the evaluation in this work. The wavelength λ is 12.5 cm for this choice of frequency. The noise level in the measurement scenario is approximately 35 dB.

The three transmitter antennas are placed as shown in Figure 7.8 with a table holding the stick to give stationary measurements during a short

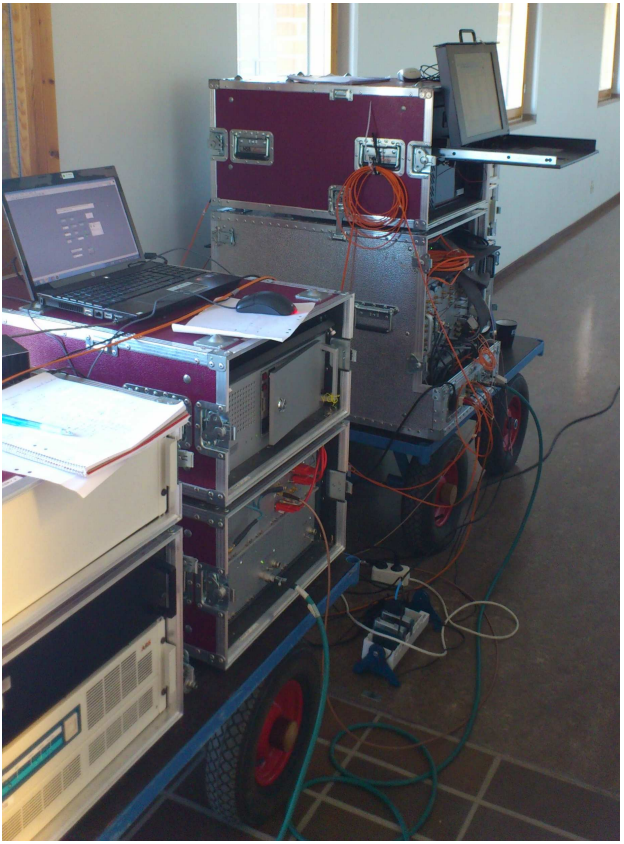

Figure 7.5 The Channel Sounder RUSK with transmitter unit closest to the viewer and receiver unit behind it.

startup sequence. A photo of the test area is shown in Figure 7.7 where the transmitter antennas are marked. Also, the start and stop position is carefully tracked but the interim trajectory is however not tracked. No exact ground truth is therefore available. The AoAs to the transmitters are measured using a laser distance measure. The AoA denoted as ”known” might be a few degrees off compared to the true values.

Figure 7.6 IMU and dipole antenna with ground plane mounted on the wooden stick.

Figure 7.7 The test area with the table holding the IMU and receiver antenna closest to the viewer. The three transmitter antennas acting as scattering objects are marked in red.

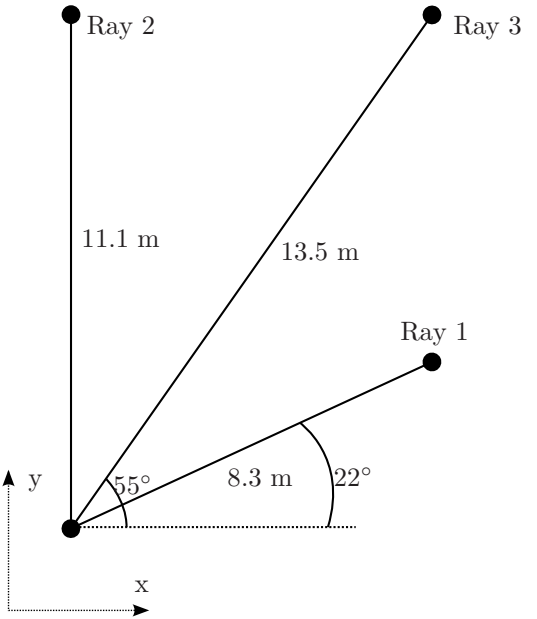

Figure 7.8 Layout of the test area with the three transmitters and the IMU/RX unit in the lower left corner.

7.3 Experiment results

The same implementation of the marginalized particle filter as used in Section 6.5 is reused here. The state initialization is according to Table 7.3. The results from two different experiments are presented in figures 7.9 and 7.10 respectively. Since the true trajectory is not known, the distance to the origin is used instead of RMSE for evaluation. Both movements start and stop at the same location. Since the transmitter and the receiver are synchronized, the frequency error becomes negligible. Thus, the white noise on the state modeling frequency error is set to track slow changes.

State	Distribution	Unit
a^1	$\mathcal{N}(1, 0.1)$	-
a^2	$\mathcal{N}(1, 0.1)$	-
a^3	$\mathcal{N}(1, 0.1)$	-
θ^1	$[\theta^1]^\star + \mathcal{U}(-10, 10)$	deg
θ^2	$[\theta^2]^\star + \mathcal{U}(-10, 10)$	deg
θ^3	$[\theta^3]^\star + \mathcal{U}(-10, 10)$	deg
ϕ^1	$\mathcal{U}(-\pi, \pi)$	rad
ϕ^2	$\mathcal{U}(-\pi, \pi)$	rad
ϕ^3	$\mathcal{U}(-\pi, \pi)$	rad

Table 7.3 The initial distributions of the states where * indicates the true AoA and $\mathcal{U}(a, b)$ is a uniform distribution between a and b. When initializing the filter, an initial estimate of the AoA is assumed to be obtained by the iterative ℓ_1 regularization algorithm presented in Section 4.1.

In the first experiment in Figure 7.9, the stick is kept on the table while moving it. This is to reduce the influence of elevation in the measurements. The pose estimation result is very promising, the filter tracks the movement and settles to zero velocity after the movement has stopped at 16 seconds. Also, the AoA is tracked well with some offset to the true values. The error at the end position is around 5 λ or 62 cm with the current wavelength. The same value with dead reckoning is 134 λ or 16.8 m.

In the second experiment in Figure 7.10, the stick is handheld in the air without support from the table. As before, the result is very promising since the filter tracks the movement and settles to zero velocity after the movement has stopped. Also, the AoA is tracked well with some drift of θ^1 at the end. The error at the end position is around 2 λ or 25 cm with the current wavelength. The distance to the origin at the end point of dead reckoning is 70 λ or 8.8 m.

Finally, the repeatability of the model is tested with 200 Monte Carlo runs. The root mean distance to the origin is calculated and presented as a cumulative distribution in Figure 7.11. The filter and the configuration of it shows a high level of convergence, 80% of the runs have a root mean squared distance of less than 10 λ. Note that the true value of the distance during the movement is not known.

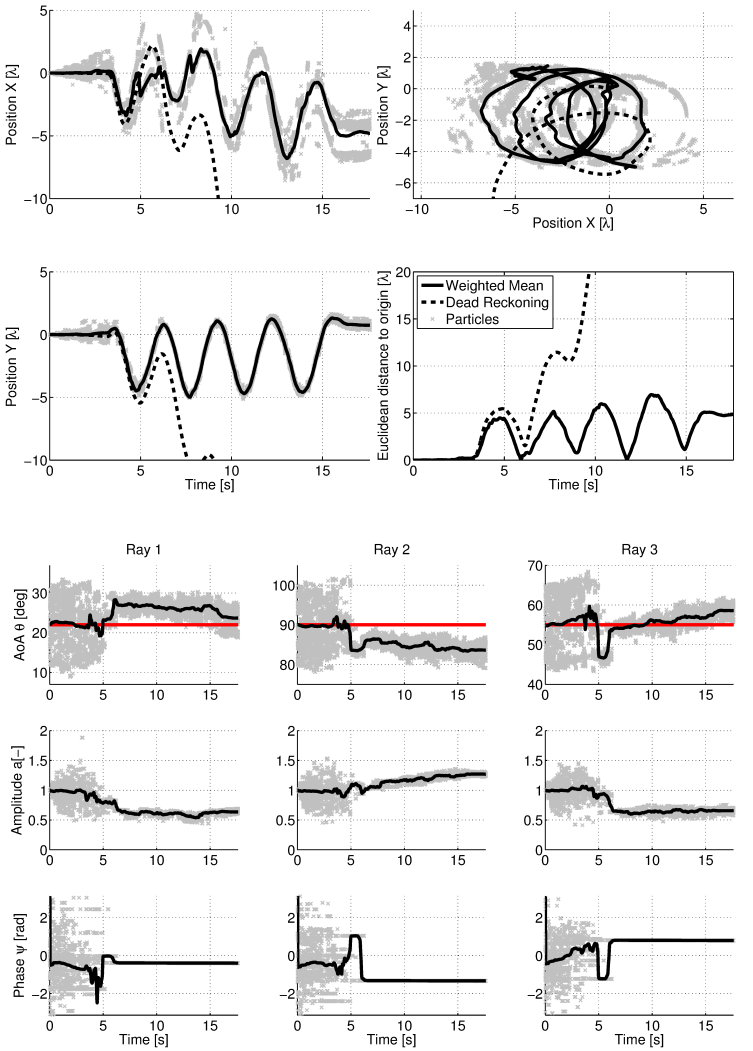

Figure 7.9 The upper left panels show the weighted average (-), dead reckoned (- -), and the 20 best particles (x) for each time instance of the trajectory for position X and Y respectively. The upper right panel shows a 2D plot for the position. The second upper panel to the right shows euclidean distance to origin for the weighted mean and the dead reckoning. The lower panel shows the estimate of AoA, amplitude and phase for each ray with the same color coding as before. Note the multiple hypotheses for position in X. The dead reckoning supplies reliable estimates until approximately 6 seconds.

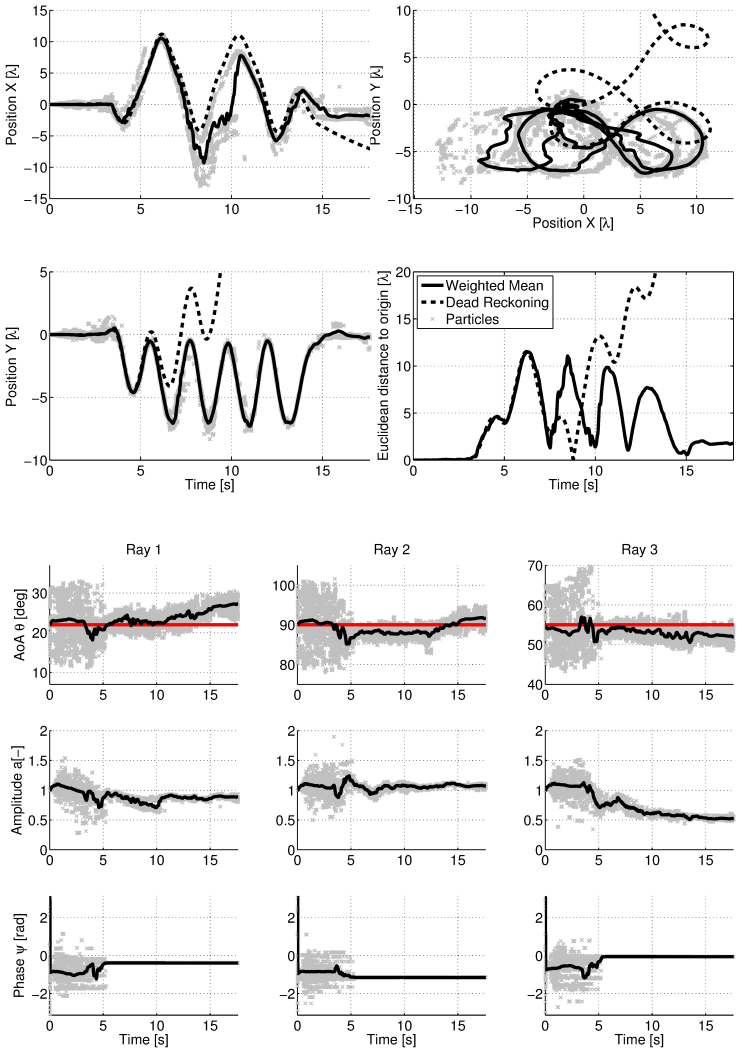

Figure 7.10 Same as Figure 7.9 but for another dataset. The results are comparable in performance. Even here there are multiple hypotheses for the position in X but as soon as more data it gathered, they can be discarded. Note that the dead reckoning in X is very good until 15 seconds while in Y it fails after 7 seconds.

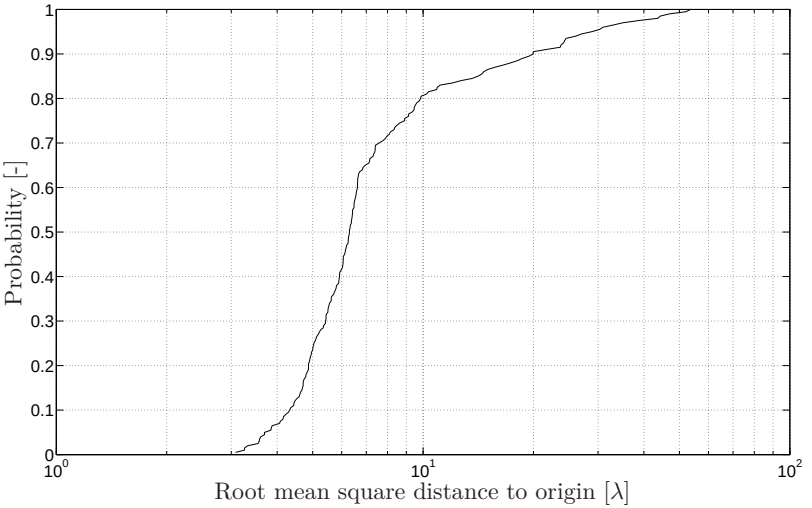

Figure 7.11 The likelihood of root mean square distance to origin for the same dataset used in Figure 7.9 is evaluated for 200 Monte Carlo runs. Approximately 80% of the runs have a root mean square distance of less than 10 λ and the number of particles is 2000. Note that the true value of the distance during the movement is not known.

7.4 Discussion

Even though the measurement scenario is carefully arranged with respect to antenna placement and measurement of start and stop position, there are error sources that are hard to eliminate. The derivation of the measurement equation (2.41) in Section 2.2 assumes that the receiver and transmitters are in the same plane. If not, the elevation angle will influence the argument of the received signal. Since it is hard to keep the free hand movement in a plane, this effect will be present and altering the phase of the received signal.

Another source of error is the amplitude of the received radio signal. It is modeled as a random walk process in the state space model, see Section 2.2. In Figure 7.12 the amplitude a of a dataset where the receiver is kept stationary is presented together with a probability plot for the individual rays. The distributions are close to being Gaussian distributions. However, when the receiver is moving the result is changed, see Figure 7.13. Especially for ray 1, the amplitude is no longer a constant with added white Gaussian noise. The reason for this behavior is unknown but one possible explanation is that the multipath propagation is more severe than expected. The noise distribution of the amplitude α can be considered to be Gaussian if the line of sight component of the multipath channel is dominant compared to the scattered

paths. However, if the power from the scattered paths is comparable to the power from the direct path, the noise distribution is better modeled as Rician [Molisch, 2005]. The reason for the rich scattering environment might be a strong ground reflection or interference with the person holding the stick. Still, the pose estimation result of the filter is very good even with these disturbances.

Even though the experimental situation has been chosen to be application friendly, compared to what could be expected in worst-case situations, the belief is that the experiments can be taken as proof-of-concept for the suggested method. The limits of performance and full potential of the method is however an area for future research.

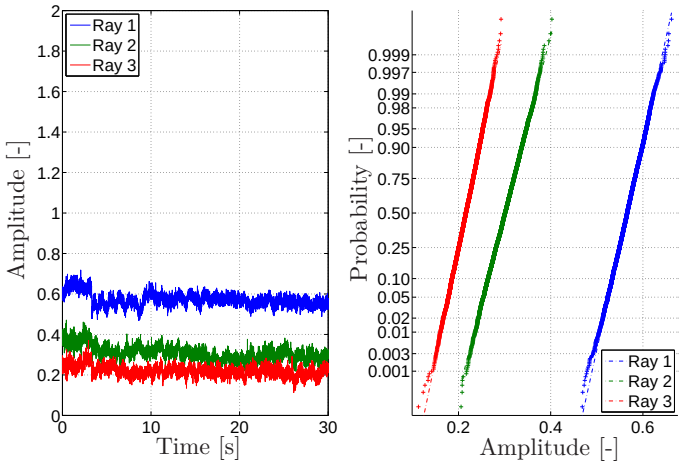

Figure 7.12 The left panel shows amplitude for the three rays in the received signal for a 30 second measurement. The level is almost constant throughout the measurement. To the right, the cumulative distribution of the same data is shown. The slopes of the three datasets are similar, indicating that the amplitude is constant with added white Gaussian noise.

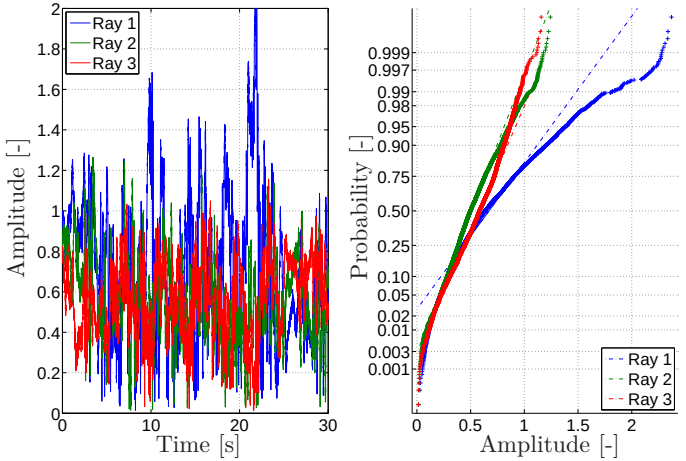

Figure 7.13 The left panel shows amplitude for the three rays in the received signal for a 30 second measurement. The variations during the measurement are large. To the right, the cumulative distribution of the same data is shown. Note the increase in variance compared to the stationary case in Figure 7.12. Ray 1 experiences a different noise distribution compared to the other rays. This could be due to more severe multipath propagation than expected.

8

Conclusions

8.1 Summary

In this thesis, the problem of estimating pose and radio channels jointly has been addressed. To connect the kinematics of a moving antenna with the radio channel response, a state space model was derived, based on a ray-trace based radio channel model. One advantage of the scheme is that signals present in the cellular systems today can potentially be used to improve pose estimation. For recursive estimation of the joint estimation problem, the marginalized particle filter was chosen as sensor fusion algorithm and a batch AoA estimation algorithm for initialization of the filter.

Some fundamental conclusions about estimating AoA and phase/frequency errors in the receiver were drawn along with a study of two batch AoA estimation approaches. Furthermore, the Cramér-Rao analysis showed that with three impinging rays and a movement that excites the system in more than one direction is enough to limit the asymptotic growth rate of the variance of the position. Also, in this case, the variance growth was limited for all other states in the model of the joint pose and radio channel estimation problem. This result is important since it shows that the radio signals contain enough information to limit the variance growth rate present in dead reckoning. The exact asymptotic growth rate of the method in this situation is an open research question.

Finally, simulations of the model showed promising performance, capable of estimating both amplitude and phase/frequency errors while moving the receiver in the channel. The number of particles in the filter needed for estimating three impinging rays was also investigated showing that a real-time implementation of the problem is within reach. To test the model with real data, an outdoor scenario with three transmitters acting as scattering objects was configured. Two different patterns, stretching approximately 2 meters each were tested with great performance in sense of pose estimation. The results showed a potential breakthrough in pose estimation performance using an inexpensive IMU without need for additional infrastructure.

8.2 Future work

This thesis opens up for several interesting future research topics and areas.

Real-time implementation

A real-time implementation of the algorithms is a natural step to take from this thesis. Depending on the computational requirements of the algorithms, the implementation can be realized in either software or in a dedicated field-programmable gate array (FPGA) hardware platform. The later will, among others, include a choice of how to restructure the filter in order to take as much advantage as possible of the parallel structure in the FPGA. For information on FPGA implementations of particle filters, see [Bolic, 2004].

3D movement

The calculations in this thesis assume that the device is moving in 2D. For the kinematic model, three states were used for position in order to be able to extend the measurement equation including a height dependence. Before that can be done, an additional state for each ray modeling the AoA in altitude needs to be added. This state will be part of the nonlinear state vector so the computational burden of the particle filter will be increased.

Using information from wideband channel measurements

One limitation made early in the thesis was to ignore the extra information that wideband radio channels will supply. Each frequency slot creates a virtual map such as in figures 2.3 to 2.5. Since the location of the receiver is equal in all maps as well as the AoA, it is only states for the complex amplitude for each ray in each map that has to be added to the state vector.

Indoor scenarios

The experiments presented in this thesis have been performed outdoors due to the simpler radio channels with fewer scattering objects. Some work has been made on estimating radio channels for an indoor environment using the same equipment but without the tight integration between pose and radio channel. More of that work can be found in [Yaqoob et al., 2013]. However, the particle filter became too computer intensive when supplying all of the measurements from the indoor session due to the increased state vector. With a dedicated hardware platform, the algorithm is believed to be fast enough to be able to use the extra information the wideband scenario yields. The long term goal for this path would be to build an algorithm capable of estimating the position in all areas where no other positioning technique exists.

Understanding the limitations due to phase/frequency errors

Tracking of the frequency error in the real experiments could be tested by adding an error signal to the measurements in order to evaluate the performance of the algorithm. This would reflect a more realistic scenario where phase noise in the receiver is present.

Improved radio channel models

The radio channel model used here assumes that all units such as transmitters, scattering objects, and receiver are static or moving so slow that Doppler shifts not originating from RX movement can be neglected. Also, the antennas used are assumed to have an isotropic antenna pattern. This is not a realistic model looking at the antennas used in modern cellular phones. An interesting work would be to investigate how the antenna pattern affects the channel impulse response and also if the non-uniform antenna pattern can be used as information for the orientation of the device.

Combining particle filters and expectation maximization algorithm

The SAGE algorithm mentioned in Chapter 2 is an implementation of the popular Expectation-Maximization (EM) algorithm, see [Dempster et al., 1977]. Recent work has proven that the particle filter and the EM algorithm can be merged where the EM is used to estimate constant states with high efficiency [Schön et al., 2011]. If the radio channels are given a constraint of how fast they are changing, the algorithm could potentially be used here.

Further evaluation of the batch AoA algorithms

The reweighted iterative ℓ_1 algorithm was chosen to be used as an initial estimator of the AoA and the number of rays to track. The evaluation of the two algorithms in Section 6.2 is done using perfect position estimates. An interesting extension of the evaluation is to let the estimated position be calculated using dead reckoning and to evaluate the algorithms on robustness with respect to position errors.

Bibliography

Achtelik, M., S. Weiss, and R. Siegwart (2011). "Onboard IMU and monocular vision based control for MAVs in unknown in- and outdoor environments". In: *Robotics and Automation (ICRA), 2011 IEEE International Conference on*, pp. 3056–3063.

Andoh, H., M. Sawahashi, and F. Adachi (1998). "Channel estimation filter using time-multiplexed pilot channel for coherent RAKE combining in DS-CDMA mobile radio". *IEICE Transactions on Communications* **81**:7, pp. 1517–1526.

Arildsen, T. and J. Blauendahl (2010). *Advanced Channel Estimation and Multiuser Detection in GSM: SAGE-Based Iterative Single-Antenna Interference Cancellation*. Lambert Academic Publishing.

Bahai, A. R., B. R. Saltzberg, and M. Ergen (2004). *Multi-carrier digital communications: theory and applications of OFDM*. Springer Verlag.

Bailey, T. and H. Durrant-Whyte (2006a). "Simultaneous localization and mapping (SLAM): Part I". *Robotics Automation Magazine, IEEE* **13**:2, pp. 99–110.

— (2006b). "Simultaneous localization and mapping (SLAM): Part II". *Robotics & Automation Magazine, IEEE* **13**:3, pp. 108–117.

Bolic, M. (2004). *Architectures for efficient implementation of particle filters*. PhD thesis.

Boss, D. and K.-D. Kammeyer (1997). "Blind GSM channel estimation". In: vol. 2, pp. 1044–1048.

Boyd, S. and L. Vandenberghe (2004). *Convex optimization*. Cambridge university press.

Broumandan, A., T. Lin, A. Moghaddam, D. Lu, J. Nielsen, and G. Lachapelle (2007). "Direction of arrival estimation of GNSS signals based on synthetic antenna array". In: *Proceedings of the 20th International Technical Meeting of the Satellite Division of the Institute of Navigation (ION GNSS'07)*.

Broumandan, A., J. Nielsen, and G. Lachapelle (2010). "Signal detection performance in rayleigh fading environments with a moving antenna". *Signal Processing, IET* **4**:2, pp. 117–129.

Candes, E. J., M. B. Wakin, and S. P. Boyd (2008). "Enhancing sparsity by reweighted ℓ_1 minimization". *Journal of Fourier Analysis and Applications* **14**:5, pp. 877–905.

Capon, J. (1969). "High-resolution frequency-wavenumber spectrum analysis". *Proceedings of the IEEE* **57**:8, pp. 1408–1418.

Coleri, S., M. Ergen, A. Puri, and A. Bahai (2002). "Channel estimation techniques based on pilot arrangement in OFDM systems". *IEEE Trans. Broadcasting* **48**, pp. 223–229.

Coutsias, E. A. and L. Romero (2004). "The quaternions with an application to rigid body dynamics".

CVX (2013). URL: `http://cvxr.com`.

Dahlman, E., S. Parkvall, J. Sköld, and P. Beming (2010). *3G Evolution: HSPA and LTE for Mobile Broadband*. Elsevier Science.

Davison, A. J. (2003). "Real-time simultaneous localisation and mapping with a single camera". In: *Computer Vision, 2003. Proceedings. Ninth IEEE International Conference on*. IEEE, pp. 1403–1410.

Dempster, A. P., N. M. Laird, and D. B. Rubin (1977). "Maximum likelihood from incomplete data via the em algorithm". *Journal of the Royal Statistical Society. Series B (Methodological)*, pp. 1–38.

Doucet, A., N. de Freitas, K. Murphy, and S. Russell (2000). "Rao-blackwellised particle filtering for dynamic Bayesian networks". In: *Proceedings of the Sixteenth conference on Uncertainty in artificial intelligence*. UAI'00. Morgan Kaufmann Publishers Inc., Stanford, California, USA, pp. 176–183.

Edfors, O., M. Sandell, J.-J. van de Beek, S. Wilson, and P. Borjesson (1998). "OFDM channel estimation by singular value decomposition". *Communications, IEEE Transactions on* **46**:7, pp. 931–939.

Fessler, J. A. and A. O. Hero (1994). "Space-alternating generalized expectation-maximization algorithm". *Signal Processing, IEEE Transactions on* **42**:10, pp. 2664–2677.

Godha, S., G. Lachapelle, and E. Cannon (2006). "Integrated GPS/INS system for pedestrian navigation in a signal degraded environment". In: *ION GNSS*. Vol. 2006.

Gordon, N., D. Salmond, and A. F. M. Smith (1993). "Novel approach to nonlinear/non-Gaussian Bayesian state estimation". *Radar and Signal Processing, IEE Proceedings F* **140**:2, pp. 107–113.

Gu, H. (1996). "Ambiguity function and Cramér-Rao bound in the multisignal case". *Radar, Sonar and Navigation, IEE Proceedings* - **143**:4, pp. 227–231.

Gu, Y., A. Lo, and I. Niemegeers (2009). "A survey of indoor positioning systems for wireless personal networks". *Communications Surveys Tutorials, IEEE* **11**:1, pp. 13–32.

Gustafsson, F. (2010). *Statistical Sensor Fusion*. Studentlitteratur.

Han, X. (2004). "Channel estimation techniques for WCDMA communication systems".

IEEE Std 952-1997 (1998). *IEEE standard specification format guide and test procedure for single-axis interferometric fiber optic gyros*.

Kalman, R. (1960). "A new approach to linear filtering and prediction problems". *Trans. ASME–J. Basic Engineering* **82**:Series D, pp. 35–45.

Karlsson, R., T. Schön, and F. Gustafsson (2005). "Complexity analysis of the marginalized particle filter". *Signal Processing, IEEE Transactions on* **53**:11, pp. 4408–4411.

Kay, S. M. (1993). *Fundamentals of statistical signal processing: Estimation theory*. Prentice Hall.

Khayrallah, A., R. Ramesh, G. Bottomley, and D. Koilpillai (1997). "Improved channel estimation with side information". In: *Vehicular Technology Conference, 1997, IEEE 47th*. Vol. 2, 1049–1053 vol.2.

Krim, H. and M. Viberg (1996). "Two decades of array signal processing research: the parametric approach". *Signal Processing Magazine, IEEE* **13**:4, pp. 67–94.

Kuipers, J. B. (1999). *Quaternions and rotation sequences: a primer with applications to orbits, aerospace, and virtual reality*. Princeton university press.

Liang, Y., H. Luo, X. Zhao, H. Zhang, and C. Yan (2006). "Nonlinear channel estimation based on particle filtering for MIMO-OFDM systems". In: *Communications, Circuits and Systems Proceedings, 2006 International Conference on*. Vol. 1. IEEE, pp. 347–351.

Maybeck, P. S. (1982). *Stochastic models, estimation, and control*. Academic press.

MEDAV (2013). URL: `http://www.channelsounder.de`.

Molisch, A. F. (2005). *Wireless Communications*. Wiley.

Ohlsson, H., L. Ljung, and S. Boyd (2010). "Segmentation of arx-models using sum-of-norms regularization". *Automatica* **46**:6, pp. 1107–1111.

Pedersen, T. (2009). *Contributions in Radio Channel Sounding, Modeling, and Estimation*. PhD thesis. The Faculty of Engineering, Science, Navigation, and Communications, Aalborg Univerity, Denmark.

Pei, L., R. Chen, J. Liu, H. Kuusniemi, T. Tenhunen, and Y. Chen (2010). "Using inquiry-based Bluetooth RSSI probability distributions for indoor positioning". *Journal of Global Positioning Systems* **9**:2, pp. 122–130.

Phidgets (2013). URL: `http://www.phidgets.com`.

Proakis, J. G. and M. Salehi (2002). *Communication systems engineering, 2nd ed.* Prentice-Hall, Inc.

Richardson, A. (2011). *WCDMA Design Handbook*. Cambridge University Press, New York, NY, USA.

Rong Li, X and V. P. Jilkov (2003). "Survey of maneuvering target tracking. Part I. dynamic models". *Aerospace and Electronic Systems, IEEE Transactions on* **39**:4, pp. 1333–1364.

Sabatini, A. M. (2006). "Quaternion-based extended Kalman filter for determining orientation by inertial and magnetic sensing". *Biomedical Engineering, IEEE Transactions on* **53**:7, pp. 1346–1356.

Sabatini, A. M., C. Martelloni, S. Scapellato, and F. Cavallo (2005). "Assessment of walking features from foot inertial sensing". *Biomedical Engineering, IEEE Transactions on* **52**:3, pp. 486–494.

Schmeink, K., R. Block, C. Knievel, and P. A. Hoeher (2010). "Joint channel and parameter estimation for combined communication and navigation using particle swarm optimization". In: *Positioning Navigation and Communication (WPNC), 2010 7th Workshop on*, pp. 4–9.

Schmidt, R. (1986). "Multiple emitter location and signal parameter estimation". *Antennas and Propagation, IEEE Transactions on* **34**:3, pp. 276–280.

Schön, T., F. Gustafsson, and P.-J. Nordlund (2005). "Marginalized particle filters for mixed linear/nonlinear state-space models". *Signal Processing, IEEE Transactions on* **53**:7, pp. 2279–2289.

Schön, T., A. Wills, and B. Ninness (2011). "System identification of nonlinear state-space models". *Automatica* **47**:1, pp. 39–49.

Skog, I. and P. Händel (2006). "Calibration of a MEMS inertial measurement unit". In: *XVII IMEKO World Congress*.

Skog, I., J.-O. Nilsson, and P Händel (2010). "Evaluation of zero-velocity detectors for foot-mounted inertial navigation systems". In: *Indoor Positioning and Indoor Navigation (IPIN), 2010 International Conference on*. IEEE, pp. 1–6.

Staszewski, R., C. Fernando, and P. Balsara (2005). "Event-driven simulation and modeling of phase noise of an RF oscillator". *Circuits and Systems I: Regular Papers, IEEE Transactions on* **52**:4, pp. 723–733.

Stoica, P. and P. Babu (2012). "SPICE and LIKES: two hyperparameter-free methods for sparse-parameter estimation". *Signal Processing* **92**:7, pp. 1580 –1590.

Sukkarieh, S., E. M. Nebot, and H. F. Durrant-Whyte (1999). "A high integrity IMU/GPS navigation loop for autonomous land vehicle applications". *Robotics and Automation, IEEE Transactions on* **15**:3, pp. 572–578.

Taylor, J. (1979). "The Cramér-Rao estimation error lower bound computation for deterministic nonlinear systems". *Automatic Control, IEEE Transactions on* **24**:2, pp. 343–344.

Titterton, D. and J. Weston (2004). "Strapdown inertial navigation technology. 2:nd edition". *The Institution of Electronical Engineers, Reston USA*.

Woodman, O. (2010). *Pedestrian Localisation for Indoor Environments*. PhD thesis. University of Cambridge, Computer Laboratory.

Woodman, O. and R. Harle (2008). "Pedestrian localisation for indoor environments". In: *Proceedings of the 10th international conference on Ubiquitous computing*. UbiComp '08. ACM, Seoul, Korea, pp. 114–123.

Yaqoob, M. A., A. Mannesson, F. Tufvesson, and B. Bernhardsson (2013). "Direction of arrival estimation with arbitrary virtual antenna arrays using low cost inertial measurement unit". *Accepted for publication in Proceedings of IEEE International Conference on Communications 2013*.

Zhang, P., J. Gu, E. Milios, and P. Huynh (2005). "Navigation with IMU/GPS/digital compass with unscented kalman filter". In: *Mechatronics and Automation, 2005 IEEE International Conference*. Vol. 3, 1497–1502 Vol. 3.